Characterization of an Erbium Atomic Beam

master thesis in physics

by

Johannes Schindler

submitted to the Faculty of Mathematics, Computer Science
and Physics of the University of Innsbruck

in partial fulfillment of the requirements
for the degree of Master of Science

Supervisors:
Ass.Prof. Dr. Francesca Ferlaino
Univ.Prof. Dr. Rudolf Grimm

Innsbruck, July 2011

Zum Besten aller Wesen.

Abstract

In this thesis we study and characterize an erbium atomic beam emerging from a high-temperature oven system. This is the first step towards the production of a quantum-degenerate gas of Er. Er is a rare-earth element and its quantum mechanical interaction properties are yet rather unexplored. Its exceptionally large magnetic moment of $7\,\mu_{\mathrm{B}}$ makes Er especially interesting, since it allows studies on the physics of dipolar quantum gases. In addition, Er shows an unusual electronic configuration and a complex energy level scheme, promising rich scattering properties and offering many possibilities for laser cooling.

Since Er has a high melting point temperature of more than $1500\,^{\circ}\mathrm{C}$, the oven system for the production of a thermal atomic beam requires specific engineering. This includes thermal shielding, heated apertures, special crucible materials as well as reliable control- and security systems. We characterize the atomic beam emerging from the oven by absorption spectroscopy and fluorescence imaging on the strong 401 nm transition. Based on our measurements, we optimize the collimation setup and we find the ideal operation temperature to be $T \simeq 1250\,^{\circ}\mathrm{C}$ with a corresponding atomic flux of $3 \times 10^{10}\,\mathrm{s}^{-1}$ injected into the Zeeman slower.

Zusammenfassung

Im Rahmen dieser Arbeit untersuchen wir einen Erbium-Atomstrahl, welchen wir mittels eines Hochtemperaturofens erzeugen. Dies ist der erste Schritt zur Erzeugung eines Quantengases von Erbium Atomen. Erbium gehört zur Gruppe der seltenen Erden, seine quantenmechanischen Wechselwirkungseigenschaften sind noch weitgehend unerforscht. Erbium ist besonders interessant, da durch sein aussergewöhlich großes magnetisches Moment von $7\,\mu_\mathrm{B}$ zahlreiche Experimente zur Physik dipolarer Quantengase ermöglicht werden. Ebenso sind aufgrund der komplexen elektronischen Struktur dieses Elements mannigfaltige Streueigenschaften zu erwarten und zudem zahlreiche Möglichkeiten zur Laserkühlung gegeben.

Der hohe Schmelzpunkt von Erbium von über $1500\,^\circ\mathrm{C}$ stellt besondere Anforderungen an das Ofendesign. Unter anderem verwenden wir eine thermische Abschirmung, beheizte Blenden, spezielles Material für den Tiegel sowie eigene Kontroll- und Sicherheitssysteme. Durch Absorptionsspektroskopie und Fluoreszenzmessungen mit dem starken atomaren Übergang bei $401\,\mathrm{nm}$ charakterisieren wir den erzeugten Atomstrahl. Basierend auf unseren Messungen optimieren wir die Ofenblenden und bestimmen die ideale Betriebstemperatur zu $T \simeq 1250\,^\circ\mathrm{C}$, bei welcher der Atomfluß in den Zeeman Slower $3 \cdot 10^{10}\,\mathrm{s}^{-1}$ beträgt.

Contents

Contents **v**

Introduction **1**

1 Thermal atomic beams **4**
1.1 Effusive oven 4
1.2 Atomic beam 6
1.3 Determination of the atomic flux 8
1.4 Spectrum 9

2 Erbium **12**
2.1 General properties 12
2.2 Electronic properties 14
2.3 Isotopes 16
2.4 Laser cooling of erbium atoms 18
2.5 Magnetic properties 20
2.6 Scattering properties 21

3 Experimental setup **23**
3.1 Vacuum chamber 23
3.2 Cooling and trapping lights 26

4 Erbium oven **29**
4.1 Oven system 29
4.2 Control system 31
4.3 Atomic beam shutter 33

5 Characterization of the atomic beam **37**
5.1 Measurement setup 37
5.2 Collimation setup 1 40
5.3 Collimation setup 2 51
5.4 Flux 57

Conclusion and Outlook **62**

A Magnetic moments of the lanthanides **65**

B Erbium oven control **67**

C Atomic beam shutter control **69**
C.1 Control box 69
C.2 Source code 70

D Calibrations **78**
D.1 Laser frequency 78
D.2 CCD camera 80

Bibliography **81**

List of Symbols and Abbreviations **88**

Introduction

By cooling atoms to ultralow temperatures, we gain extraordinary high control over their external as well as their internal degrees of freedom. Therefore, ultracold atoms empower us to study and to understand phenomena belonging to very different branches of research, such as quantum chemistry, condensed matter and few-body physics, high-temperature superconductivity, and quantum simulations [1–5].

The field of ultracold quantum gases has been subject to vast developments in the past two decades. The first Bose-Einstein condensation, a phase transition that leads to the macroscopic occupation of the system's ground state at ultralow but finite temperatures, was attained in 1995 [6–8]. Subsequently, also fermions, representing the basic building blocks of matter were cooled to quantum degeneracy [9–11]. The ability to modify the two-body interaction by magnetic or optical Feshbach resonances [12] increased dramatically the level of control on the systems. This opened the way of studying tunable quantum gases in the weak and in the strong interacting regime and of creating more complex structures such as weakly bound dimer states [13–16]. All of this pioneering works were performed on elements from the alkali series and rely on the isotropic and short-ranged contact interaction. Alkali atoms provide comparatively simple systems with just one valence electron in the electronic s-shell and convenient optical transitions for laser cooling experiments. At ultralow temperatures, the interaction between those atoms can simply be described by a single scattering parameter known as the s-wave scattering length a.

In further advance, the laser cooling and trapping techniques were extended to more complex atomic species, which provide additional challenges and prospects [17–19]. In particular, atoms or molecules that interact via the dipole-dipole interaction (DDI) lead to totally new phenomena. In contrast to the contact interaction, the DDI has anisotropic and long-range nature. This gives rise to new quantum phases and offers geometry dependent tunability [20, 21]. Two candidate systems exhibit strong DDI: polar molecules and magnetic atoms. Polar molecules carry a large electric dipole moment but require a complex production sequence since direct laser cooling can hardly be applied [22, 23]. Magnetic

atoms exhibit smaller magnetic dipole moments but offer more robust systems. Chromium has been so far the only strongly magnetic species to be Bose condensed[1] [24]. In this system, the dipolar character manifests itself in spectacular effects such as the d-wave collapse of the trapped gas [25], the geometry dependent stability of the system [26] and suppression of collisional relaxation in an optical lattice [27]. Nowadays, exotic atoms with high magnetic moments, as found in the lanthanide series are subject of increased interest in our community and represent the cutting-edge research on the DDI [28–30].

Erbium is one of those elements with highly magnetic atoms. It is a rather unexplored species, which shows a very rich energy structure and many favorable properties like a large number of isotopes, a high mass, a high magnetic moment and a variety of narrow as well as broad laser cooling transitions. In addition, erbium's unusual electronic configuration leads to complex scattering properties [31–34].

The primary goal of our experiment is to Bose condense Er atoms and to investigate their scattering properties. Besides studies of ultracold dipolar Bose or Fermi gases, also the formation of Feshbach molecules with even higher magnetic moments or few body physics with DDI are of interest. Our vision is to admix Li atoms to Er, leading to a crystal like system with extreme mass imbalance to observe novel effects on the field of Efimov physics or of the BEC-BCS crossover.

At the moment, our experiment is in the construction phase. We set up the complete vacuum apparatus and the main laser setup for cooling and trapping. During my master thesis time, I contributed to the mounting of the vacuum apparatus, the installation of the cooling water system and the construction of various coils to generate magnetic fields including the winding of the Zeeman slower coils. Furthermore, I had the possibility to gain some experience with a dye laser that we plan to use for the narrow line magneto-optical trap. Besides the above mentioned tasks, the main focus of my work is the setting up and characterization the Er oven system. I installed and programmed a control- and safety system for the oven as well as an atomic beam shutter control system. Once the Er oven was operating, I characterized the atomic beam by means of laser spectroscopy and optimized the beam collimation setup based on these measurements.

This thesis is structured as follows. Chapter 1 gives an overview on the fundamental theoretical concept to understand the atomic beam behavior. In Chap. 2 we review the main properties of Er atoms with emphasis on its laser cooling transitions and trapping potential. Chapter 3 gives an overview on our complete experimental setup including the vacuum chamber and the laser setup. The detailed setup and working principle of the Er oven is explained in Chap. 4.

[1] Recently, also Dysprosium atoms have been Bose condensed in the group of B. Lev at University of Illinois at Urbana-Champaign (private communication 07.2011).

Finally, in Chap. 5 we present the results of the laser spectroscopy measurements that characterize the Er atomic beam and that we used to adapt the Er oven design to our requirements.

Chapter 1

Thermal atomic beams

The starting point of our experiment is a thermal beam of Er atoms produced from an effusive high-temperature oven. The atomic beam is then decelerated via the Zeeman slower technique and later trapped in a magneto-optical trap. In this Chapter, we introduce the working principles of an effusive oven and the methods to characterize the atomic beam emerging from the oven.

1.1 Effusive oven

There exist many different kinds of sources for the production of a thermal atomic beam, depending on its demands and source material [35]. For source materials with high melting points, coated heated-filaments or laser deposition generate free atoms, but provide only limited atomic flux. Wicking recirculation sources offer higher flux and are a clever way to conserve source material in applications with needs for long source life, such as in atomic clocks. For our purpose, we use an effusive heated oven combined with a bright wall collimator that we discuss in Sec. 1.2. It provides a robust system with a high, well controllable atomic flux. The oven itself consists of a tube with an aperture. It is heated by surrounding heating wires and is water cooled for thermal shielding. The technical details are given in Chap. 4, in the following we describe the theoretical working principle on a simplified system.

We consider an ideal atomic gas in thermal equilibrium at temperature T stored in a box. It is described by the ideal gas law

$$p = k_\mathrm{B}\, n\, T\,, \tag{1.1}$$

where p is the pressure, k_B the Boltzmann constant and n the atomic density. If the box is surrounded by vacuum and has a circular aperture with diameter b_1, the atoms escape from it because of the pressure gradient between the box and the vacuum. Here, it is important to distinguish different regimes of the

oven operation. Depending on p, the atoms suffer collisions with each other. The mean distance atoms travel between two successive collisions, the so called mean free path λ_{mf}, is given by

$$\lambda_{\mathrm{mf}} = \frac{1}{\sqrt{2}\,\pi\, d_0^2\, n}\,, \tag{1.2}$$

where d_0 is the atomic diameter [36]. If λ_{mf} is smaller than the size of the aperture, the atoms encounter many collisions while emerging from the box. This leads to a hydrodynamic flow, a collective transport process, and is described by fluid dynamics. In contrast, for

$$\lambda_{\mathrm{mf}} \gtrsim b_1 \tag{1.3}$$

atom-atom collisions are rare and atom-wall collisions dominate. This is the effusive- or molecular flow regime, in which our effusive oven works. The expansion is an individual transport process where mechanisms as so called diffusive reflection can occur: an atom hits a wall, sticks to it and is re-emitted in an angle that is independent of its incident angle. By this, in contrast to hydrodynamic flow, an atom that hits the inner face of the aperture can return to the box. Furthermore, in the effusive regime, the emergence of atoms from the box does not change the spatial- nor the velocity distribution of the atoms inside the box.

In the effusive regime, we can calculate the flux emerging from the box as follows. The velocity $v = |\vec{v}|$ of the atoms inside the box is described by the well known 3D Maxwell-Boltzmann velocity distribution

$$P_v(T) = C\,\left(\frac{m}{k_{\mathrm{B}}\,T}\right)^{\frac{3}{2}}\, v^2\, \exp\!\left(\frac{-\,m\,v^2}{2\,k_{\mathrm{B}}\,T}\right)\,, \tag{1.4}$$

with C a normalisation constant and m the mass of an atom. The most probable velocity is $v_{\mathrm{mp}} = \sqrt{2\,k_{\mathrm{B}}\,T\,/\,m}$ and the mean velocity is $\bar{v} = 2\,v_{\mathrm{mp}}\,/\,\sqrt{\pi}$.

Figure 1.1 illustrates the atomic volume $V = \bar{v}\,\mathrm{d}t \cdot A\,\cos\alpha$ leaving the box in the time interval $\mathrm{d}t$ [37]. Here, α is the angle of emergence and $A = b_1^2\,\pi\,/\,4$ is the area of the aperture. Only a part $\mathrm{d}\omega\,/\,(4\,\pi)$ of the atoms travels on a solid angle $\mathrm{d}\omega$. The number of atoms $\mathrm{d}N$ per unit time $\mathrm{d}t$ leaving the box into $\mathrm{d}\omega$ is given by the unit flux $\mathrm{d}\Theta$ and reads as

$$\mathrm{d}N = \mathrm{d}\Theta\,\mathrm{d}t = \frac{\mathrm{d}\omega}{4\,\pi}\,n\,\bar{v}\,\cos\alpha\,A\,\mathrm{d}t\,, \tag{1.5}$$

where n is the atomic density. Integrating Eq. (1.5) over the solid angles $\mathrm{d}\omega = 2\,\pi\,\sin\alpha\,\mathrm{d}\alpha$ with α from 0 to $\pi/2$ gives the total flux coming out of the box

$$\Theta = \frac{1}{4}\,n\,\bar{v}\,A\,. \tag{1.6}$$

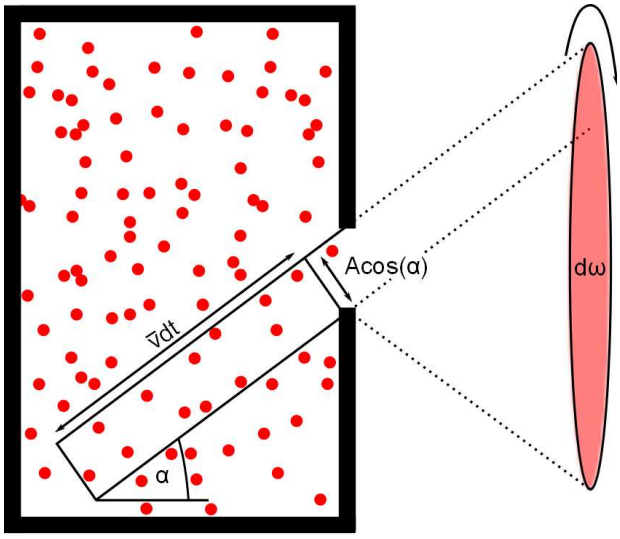

Figure 1.1: In the time interval dt, an atomic volume of $V = \bar{v}\,\mathrm{d}t \cdot A\,\cos\alpha$ leaves the box at an angle of emergence α. A is the area of the aperture, $\bar{v}$ is the mean velocity of the atoms. Integration in spherical coordinates over φ from 0 to $2\,\pi$ and over ϑ from 0 to α gives the volume emerging into the solid angle dω.

1.2 Atomic beam

The angular distribution of the atoms leaving the box from the aperture is proportional to $\cos\alpha$, as given in Eq. (1.5). Only atoms travelling at small angles are useful for the experiment, since they can travel through the apparatus without hitting it. A large fraction of atoms is unused and it is needed to block it to avoid or reduce source material deposition in the apparatus. The atomic beam can be narrowed by collimating it by a second aperture, aperture 2, in front of the first aperture, aperture 1. This is a so called dark wall collimator that provides simple geometric shading by cutting off the unused part of the source beam. This technique is not suitable for our experiment, since Er deposited at the apertures can overgrow and close the aperture. Therefore, we use heated apertures that re-emit the blocked atoms. This is a type of a so called bright wall collimator that conserves the source material and extends the source life time [35]. In terms of simplicity, in the following we neglect that the apertures are heated. Provided that the mean free path of the atoms is larger than the typical geometry of the oven, this is a valid approximation.

Figure 1.2 shows the oven with and additional aperture 2 with diameter b_2 at a distance a from aperture 1. Only atoms inside the dotted lines contribute to the atomic beam leaving the oven. The beam emerges into a solid angle around the z-axis of

$$\omega = 2\,\pi\,(1 - \cos\alpha)\,, \quad \text{where} \quad \alpha = \tan^{-1} f \quad \text{and} \quad f = \left(\frac{b_1/2 + b_2/2}{a}\right)\,, \tag{1.7}$$

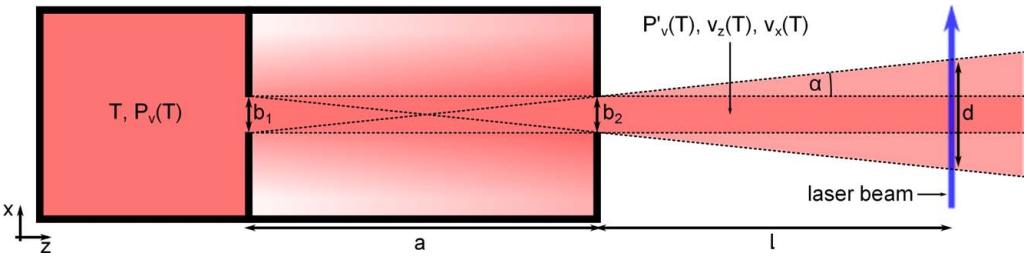

Figure 1.2: Scheme of an effusive oven with aperture 1 of diameter b_1 and aperture 2 at a distance a with diameter b_2. Inside the box, the atoms have temperature T and velocity distribution $P_v(T)$. Only atoms inside the dotted lines contribute to the atomic beam. The beam emerges into a solid angle $\omega = 2\,\pi\,(1 - \cos\alpha)$ and has diameter d at a distance l from aperture 2. The atoms in the beam have velocity distribution $P'_v(T)$ and longitudinal and transversal velocity components $v_z(T)$ and $v_x(T, f)$. A laser beam crosses the atomic beam transversal at distance l from aperture 2.

where f is the collimation ratio. At a distance l from the aperture 2, the beam has a diameter d of

$$d = 2\left((a + l)\,f - \frac{b_1}{2}\right) . \tag{1.8}$$

The flux Θ' through the aperture is obtained by integrating Eq. (1.5) over $\mathrm{d}\omega = 2\,\pi\,\sin\alpha\,\mathrm{d}\alpha$ from $\alpha = 0$ to $\alpha = \tan^{-1} f$:

$$\Theta' = \frac{1}{4}\,n\,\bar{v}\,A\,\frac{f^2}{1 + f^2} . \tag{1.9}$$

A different type of bright wall collimator uses a long channel instead of a circular hole for aperture 1. In the effusive regime, wrongly directed atoms hit the tube wall and by diffusive reflection they can return to the source or contribute to the directed beam. This changes the angular distribution of the atoms from Eq. (1.5) considerably. The flux of atoms travelling along the tube is undiminished, whereas the total atomic flux Θ_{tube} is reduced to

$$\Theta_{\mathrm{tube}} = \frac{1}{\kappa}\,\Theta . \tag{1.10}$$

The factor $1/\kappa$ depends on the geometry of the channel and for a long circular cylindrical tube it is given by $1/\kappa = (8\,b_1)\,/\,(3\,a_1)$, where b_1 is the diameter and a_1 the length of the tube [37]. However, as the longitudinal flux is not altered by such a collimator, Eq. (1.9) also holds in this case, given that f is small and $\lambda_{\mathrm{mf}} \gtrsim a_1$.

In an atomic beam the velocity distribution of the atoms is no longer described by Eq. (1.4) as in the box. Since, as shown in Eq. (1.5) and Fig. 1.1, the probability of an atom to emerge from the box is proportional to its velocity, the velocity distribution changes to

$$P'_v(T) = C'\left(\frac{m}{k_{\mathrm{B}}\,T}\right)^2 v^3\,\exp\!\left(\frac{-\,m\,v^2}{2\,k_{\mathrm{B}}\,T}\right) , \tag{1.11}$$

with normalisation constant C' and $P'_v(T) \propto v^3$. Thus, the most probable velocity changes to $v'_{\mathrm{mp}} = \sqrt{3\,k_B\,T\,/\,m}$ and the mean velocity is $\bar{v}' = v'_{\mathrm{mp}}\,\sqrt{3\,\pi\,/\,8}$ [37].

We can distinguish two components of the velocity distribution: a longitudinal distribution with velocities $v_z(T)$ and a transversal distribution with velocities $v_x(T, f)$. The longitudinal distribution is determined by the temperature T of the source, whereas the transversal distribution has to fulfil the boundary condition of the apertures and is determined by the collimation ratio f from Eq. (1.7). The individual velocities must obey

$$v_x \leq f\,v_z \qquad [38]. \tag{1.12}$$

1.3 Determination of the atomic flux

We can control the flux by the source temperature. The source should emit as many atoms as necessary for the experiment but as few atoms as possible to extend the source life-time. To monitor the flux, we measure it by laser spectroscopy.

In a simple model we consider the atoms as pure two level systems (2-LS) with ground state $|g\rangle$ and excited state $|e\rangle$. The energy difference of the two states is $\Delta E_{\mathrm{eg}} = h\,\nu_0$ with the transition frequency ν_0. If an atom absorbs a photon from a resonant laser beam with frequency ν_0, the atom is excited from $|g\rangle$ to $|e\rangle$. After the lifetime τ of $|e\rangle$, the atom decays back to $|g\rangle$ by spontaneous emission of a photon with energy $h\,\nu_0$ and can be re-excited. The photon is emitted in random directions and can be observed as fluorescence light [39]. Therefore, the intensity of the transmitted light is reduced by the amount of absorbed light and is proportional to the atomic density.

As shown in Fig. 1.2, we cross the atomic beam transversely with a resonant laser beam at the distance l from aperture 2. For laser beam intensities below the saturation intensity I_{sat} of the transition, the Beer-Lambert law describes the transmission of light with incident intensity I_0 through the atomic beam [40]:

$$I = I_0\,\exp(-D)\ . \tag{1.13}$$

D is related to the optical density (OD) of the atomic beam by $D = \ln(10)\,OD \approx 2.3\,OD$. For the laser beam interacting with the atomic beam from x_1 to x_2, D is defined as

$$D = \int_{x_1}^{x_2} n(x)\,\sigma_0\,\mathrm{d}x \approx n\,\sigma_0\,j\,, \tag{1.14}$$

where σ_0 is the cross-section for the absorption of a resonant photon by an atom [38]. For small angles α from the beam axis, the density can be estimated as constant over the light-atom interaction length $j = x_2 - x_1$. In general, j is not equal to the atomic beam diameter d, since atoms that are not in center have velocity components in the direction of the laser beam. Hence, their resonance

frequencies are Doppler shifted and these atoms do not interact with the light. In a 2-LS, the absorption cross-section is given by

$$\sigma_0 = \frac{3\,\lambda^2}{2\,\pi} \tag{1.15}$$

for resonant light with wavelength $\lambda = c\,/\,\nu_0$ [41]. Combining Eq. (1.13 - 1.15) yields to the atomic density:

$$n = -\frac{2\,\pi}{3\,\lambda^2}\,\frac{1}{j}\,\ln\left(\frac{I}{I_0}\right)\,. \tag{1.16}$$

In this way, by measuring I_0, I and j, we can calculate the total flux Θ_{tot} out of an source with aperture diameter b_1 and temperature T by inserting Eq. (1.16) into Eq. (1.6):

$$\Theta_{\text{tot}} = -\frac{\pi^{\frac{3}{2}}}{24}\,\frac{b_1^2}{\lambda^2\,j}\,\ln\left(\frac{I}{I_0}\right)\,\sqrt{\frac{2\,k_{\text{B}}\,T}{m}}\,. \tag{1.17}$$

Respectively, by Eq. (1.9), we can calculate the flux injected into a certain angle around the beam axis.

1.4 Spectrum

To characterize the atomic beam in further detail, we scan the frequency ν of the longitudinally crossed laser light over the atomic resonance at ν_0. The transmitted light intensity I as a function of ν represents the absorption spectrum. We find an absorption peak around ν_0 and its exact position, width and shape reflect the physics of the atomic beam. The natural line shape and -width of the unperturbed atoms get altered and broadened by their thermal motion, atom-atom collisions or interaction with light. By understanding the underlying broadening mechanisms, we can conclude from the absorption spectrum on the collimation, temperature or flow regime of the source and the atomic beam.

Natural linewidth

The natural linewidth $\Delta\nu_{\text{nat}}$ is the fundamental limit of the linewidth. Due to the finite lifetime τ of the exited state, the Heisenberg energy uncertainty relation $\Delta E\,\tau = h$ limits the width to

$$\Delta\nu_{\text{nat}} = \frac{\Delta E}{h} = \frac{1}{2\,\pi\tau}\,. \tag{1.18}$$

The natural line shape can be derived from a classical model of a damped harmonic oscillator for the excited electron [38]. In this model, the atomic potential is approximated as a harmonic potential and radiative energy loss results in damping. This leads to

$$I_{\text{nat}}(\nu) = I_0\,\frac{(\Gamma/4\pi)^2}{(\nu-\nu_0)^2 + (\Gamma/4\pi)^2}\,, \tag{1.19}$$

which is a Lorentzian function with peak intensity I_0 and full width half maximum (FWHM) $\Delta\nu_{\mathrm{nat}} = \Gamma/2\pi$. $\Gamma = 1/\tau$ corresponds to the spontaneous decay rate of the excited state.

Doppler broadening

Moving atoms see the frequency of a laser beam Doppler shifted. Accordingly, the resonant condition for an atom moving at a non-relativistic velocity v is

$$\nu = \nu_0 + \frac{\vec{k}\,\vec{v}}{2\,\pi} = \nu_0 \left(1 + \frac{v_k}{c}\right) , \tag{1.20}$$

where $\vec{k}$ is the wave vector of the light wave, $v_k = \vec{v}\,\vec{e}_k$ is the velocity component in its direction and c is the speed of light. Since in a thermal gas the atoms have distributed velocities, this shift leads in first order to a broadening of the spectral line. For the interaction with the light, only v_k needs to be considered, thus a 1D Maxwell-Boltzmann distribution with normalization constant C'' describes the velocity distribution of free atoms:

$$P_{v_k}(T) = C'' \sqrt{\frac{m}{k_B\,T}}\, \exp\!\left(\frac{-\,m\,v^2}{2\,k_B\,T}\right) . \tag{1.21}$$

Substituting $v = c\,(\nu/\nu_0 - 1)$ gives the probability distribution $P_\nu(T)$ that is proportional to the line shape

$$I_{\mathrm{D}}(\nu, T) = I_0(T)\, \exp\!\left(\frac{-\,c^2\,m\,(\nu - \nu_0)^2}{2\,k_{\mathrm{B}}\,T\,\nu_0^2}\right) , \tag{1.22}$$

which is a Gaussian function with peak intensity $I_0(T)$. It has a Doppler width $\Delta\nu_{\mathrm{D}} = (\nu_0/c)\,\sqrt{2\,k_{\mathrm{B}}\,T\,/\,m} = \nu_0\,v_{\mathrm{mp}}\,/\,c$ and a FWHM of $\Delta\nu_{\mathrm{D}}^{\mathrm{FWHM}} = 2\,\sqrt{\ln 2}\,\Delta\nu_{\mathrm{D}}$.

In an atomic beam the velocity distribution is not a pure Maxwell-Boltzmann distribution, but is additionally proportional to v. Therefore, according to Eq. (1.11), v'_{mp} has to be used and thus $\Delta\nu'_{\mathrm{D}} = \nu_0\,v'_{\mathrm{mp}}\,/\,c$. However, the main difference to the free gas is that the distribution has two components with velocities v_x and v_z. Thus, the Doppler width also has two components and according to Eq. (1.12):

$$\Delta\nu_{\mathrm{D},x} = \Delta\nu_{\mathrm{D},z}\,f = \frac{\nu_0}{c}\,v'_{\mathrm{mp}}\,f\,. \tag{1.23}$$

This means that the Doppler broadening of a spectral line is reduced by collimating the atomic beam. Thus, the resolution can be increased and, more important for us, conclusions on the collimation can be drawn.

Other broadening mechanisms

Saturation- or power broadening occurs when the intensity of the laser beam exceeds or is comparable to the saturation intensity I_{sat} of the transition. Then,

the optical pumping rate is larger than the relaxation rate and the line is broadened [38]. The resulting line has a Lorentzian shape with FWHM

$$\Delta\nu_{\mathrm{S}} = \Delta\nu_{\mathrm{nat}}\sqrt{1 + I/I_{\mathrm{sat}}}\,. \tag{1.24}$$

For $I \ll I_{\mathrm{sat}}$ it is thus negligible.

Collisional- or pressure broadening results from the deformation of the electronic wave function during an atom-atom collision. Thus, the transition frequency is shifted and the line is broadened [38]. The resulting line has a Lorentzian shape with FWHM

$$\Delta\nu_{\mathrm{col}} = n\,\sigma_{\mathrm{at}}\,v_{\mathrm{mp}} \;\propto\; n\,\sqrt{T}\,. \tag{1.25}$$

Since the collision cross-section σ_{at} for Er is not known yet, we cannot make predictions on the strength of this mechanism besides that for a constant density n, the linewidth scales with $\sqrt{T}$. In general, due to the limited collisions in the effusive regime, this effect should be negligible.

If several different mechanisms contribute to the broadening of a line, the resulting total line shape is represented by the convolution of the individual line shapes. For instance, a line broadened due to Doppler broadening as well as due to saturation broadening has a line shape described by a Voigt profile:

$$V(\nu;\Delta\nu_{\mathrm{G}},\Delta\nu_{\mathrm{L}}) = \int_{-\infty}^{+\infty} G(\nu';\Delta\nu_{\mathrm{G}})\,L(\nu-\nu';\Delta\nu_{\mathrm{L}})\,\mathrm{d}\nu'\,. \tag{1.26}$$

$G(\nu;\Delta\nu_{\mathrm{G}})$ represents the Gaussian contribution with width $\Delta\nu_{\mathrm{G}} = \Delta\nu_{\mathrm{D}}^{FWHM}$, $L(\nu;\Delta\nu_{\mathrm{L}})$ represents the Lorentzian contribution with width $\Delta\nu_{\mathrm{L}} = \Delta\nu_{\mathrm{nat}} + \Delta\nu_{\mathrm{S}}$. In this case, the resulting total linewidth $\Delta\nu_{\mathrm{V}}$ is estimated as

$$\Delta\nu_{\mathrm{V}} \approx 0.5346\,\Delta\nu_{\mathrm{L}} + \sqrt{0.2166\,\Delta\nu_{\mathrm{L}}^2 + \Delta\nu_{\mathrm{G}}^2} \quad [42]. \tag{1.27}$$

If we do not consider the spectrum of a free gas, but the transversal spectrum of an atomic beam, according to Eq. (1.23), we have to employ the reduced Doppler width $\Delta\nu_{\mathrm{D},x}^{FWHM}$ in Eq. (1.26) and Eq. (1.27).

Chapter 2

Erbium

Erbium is a very interesting and rather unexplored element for ultracold gas experiments. It is a soft, silver-colored metal with an atomic number of 68. It belongs to the rare earth elements and is part of the lanthanide series. There is an increasing interest in elements from this series, since they can exhibit high magnetic moments and have exotic electronic configurations, which opens up many possibilities for laser cooling applications. In this Chapter, we present relevant properties of erbium atoms, including the electronic, the magnetic and the scattering properties. We also discuss the optical transitions that we want to use for laser cooling and trapping Er atoms.

2.1 General properties

Erbium was discovered in 1843 in a quarry near the village of Ytterby in Sweden, as other rare earth elements such as Ho, Tm and Yb. Today, Er is almost exclusively mined in China. It finds many commercial applications in laser technology. For instance, it is used as doping element for fiber lasers. Here, trivalent Er ions are pumped with 980 nm or 1480 nm light and emit light at wavelengths around 1550 nm [43,44]. In optical communication, this is used for fiber amplifiers, which allow fast and relatively cheap signal amplification at low noise [45–47]. Also the Er:YAG solid state laser finds common use in medical photo-ablation treatments due to the strong absorption of its 2940 nm infrared light in water [48, 49].

Erbium is a soft, silver-colored rare earth metal. Macroscopically it has a fibroid structure, microscopically it forms a hexagonal close packed crystal [50]. Similar to Cr [51], Er has a comparatively high melting point temperature of $T_{\mathrm{melt}} = 1529\,^{\circ}\mathrm{C}$ [52]. Figure 2.1 shows its vapor pressure as a function of the temperature. For comparison, we also plot the vapor pressure of other rare earth elements such as Tm, Yb and Sa, of the magnetic Cr atoms and of the alkali metal Li, which we will in future experiments admix to the Er machine. The

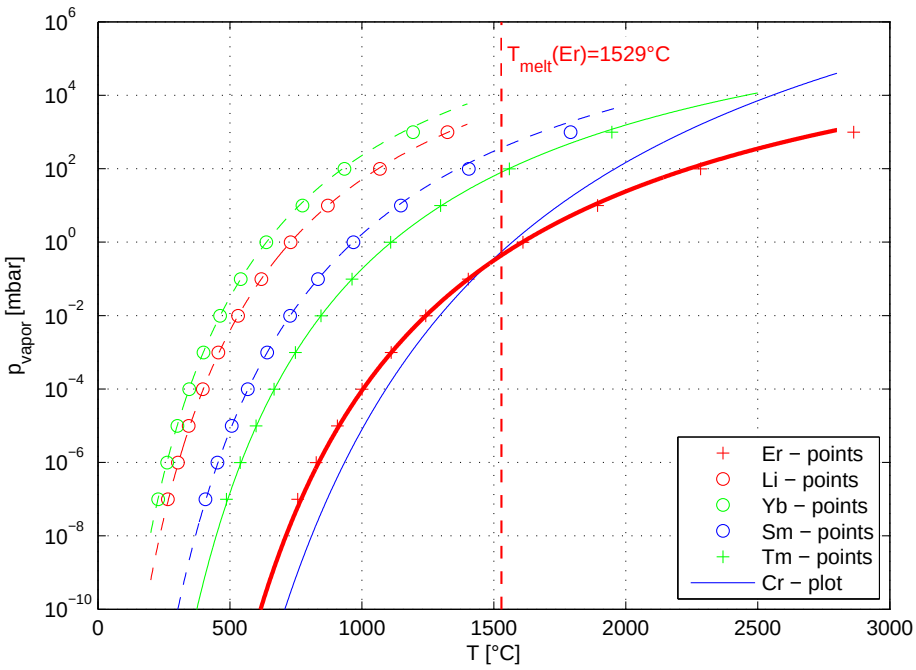

Figure 2.1: Vapor pressure as a function of the temperature for Er, Li, Yb, Sm, Tm and Cr. Erbium requires high temperatures for vapor pressures suitable for the production of a thermal atomic beam. The solid and dashed lines are fits to the data [53] using Eq. 2.1. The vertical dotted line shows the melting point temperature T_{melt} of Er.

data points are extracted from [53] and fitted to an Antoine equation [54], which approximates the relation between vapor pressure and temperature:

$$P_{\mathrm{vapor}}(T) = \exp\left(a - \frac{b}{c+T}\right), \tag{2.1}$$

with the fit parameters a, b and c. Erbium and Cr show the lowest vapor pressures for a given temperature. Although Er, Tm and Yb are neighboring elements, the melting point of Yb is much smaller than that of Er and Tm[1]. It is likely that this is due to the different crystal structure, which is hexagonal for Er and Tm, but cubic for Yb [50, 55]. For Er, the required high temperatures for sufficiently high vapor pressures make the production of an oven technologically challenging. As we will discuss in Sec. 5.4, we estimate that temperatures of 1200 °C lead to a reasonable Er atom flux for Zeeman slower (ZS) and magneto-optical trap (MOT) applications.

Erbium has the advantage of showing good getter properties. As reported in Ref. [56], Er films have exceptionally high adsorption activity especially for hydrogen, which commonly limits the achievable pressure in a vacuum chamber.

[1] $T_{\mathrm{melt}}(\mathrm{Yb}) = 824\,°\mathrm{C}$, $T_{\mathrm{melt}}(\mathrm{Tm}) = 1545\,°\mathrm{C}$, [53].

When the Er oven is turned on, a part of the atoms coats the inner walls of the vacuum chamber. Remnant atoms hitting the wall stick to it, and the pressure drops. This eases the production of ultra high vacuum (UHV) conditions in the vacuum chamber. It is the same principle as that of a Ti-sublimation pump, but since the surface area of Er films is much larger than that of Ti films, the effect should be even stronger with Er.

Erbium is very appealing for quantum gas experiments. First, it has a comparatively high magnetic moment of $7\,\mu_\mathrm{B}$ [2]. Nowadays, highly magnetic atoms are attracting great attention in our community because of the many possibilities to study dipolar effects [20]. Second, Er has a rich energy structure, which results from its unusual electronic configuration, where an incomplete f-shell with two electron vacancy is submerged by a full s-shell. This offers many possibilities for various laser cooling schemes and leads to novel collisional behavior. In addition, the numerous Zeeman levels open opportunities for quantum computing, as recently proposed in [57]. Third, six stable isotopes provide flexibility for the experiment and allow investigation of bosonic as well as fermionic systems.

The group of Jabez J. McClelland at the National Institute of Standards and Technology (NIST) has been the first to demonstrate laser cooling of a magnetic rare earth species. They produced a blue MOT with 10^5 atoms at temperatures below $25\,\mu$K [33, 58], as well as a narrow-line MOT with temperatures below $2\,\mu$K [34].

2.2 Electronic properties

The electronic ground state of Er is in a [Xe]$4f^{12}6s^2$ configuration. The [Xe] means that, as in the noble gas Xe, all shells energetically up to the $5p$ shell are fully occupied. From the 14 valence electrons, two of them fill the $6s$ shell and the remaining 12 are arranged in the $4f$ shell, leaving it with a two electron vacancy. Therefore the incomplete $4f$ shell is subjacent to the complete $6s$ shell, what is called submerged shell structure. This results in very rich scattering properties [31, 32] and a complex energy level scheme [29, 59], as shown in Fig. 2.2.

Since the bosonic isotopes have nuclear spin quantum number $I = 0$, the relevant quantum number is the total angular momentum quantum number J. Er has 110 states with J values ranging from 2 to 12. In Fig. 2.2 even parity[3] states are indicated with red horizontal lines, odd parity states with black horizontal lines. The arrows mark transitions from the even parity ground state at $J = 6$ to odd excited states at $J = 7$. This is because in an electric dipole transition,

[2] The Bohr magneton is defined as $\mu_\mathrm{B} = \frac{e\hbar}{2m_\mathrm{e}}$ with e the elementary charge, $\hbar$ the reduced Planck constant and m_e the electron rest mass.

[3] Parity is a symmetry property of the electronic wave function. The parity operator $\hat{P}$ inverts the wave function through the origin. If $\hat{P}\Psi(\vec{r}) = \Psi(-\vec{r}) = \Psi(\vec{r})$ the wave function has even parity, if $\hat{P}\Psi(\vec{r}) = \Psi(-\vec{r}) = -\Psi(\vec{r})$ it has odd parity [60].

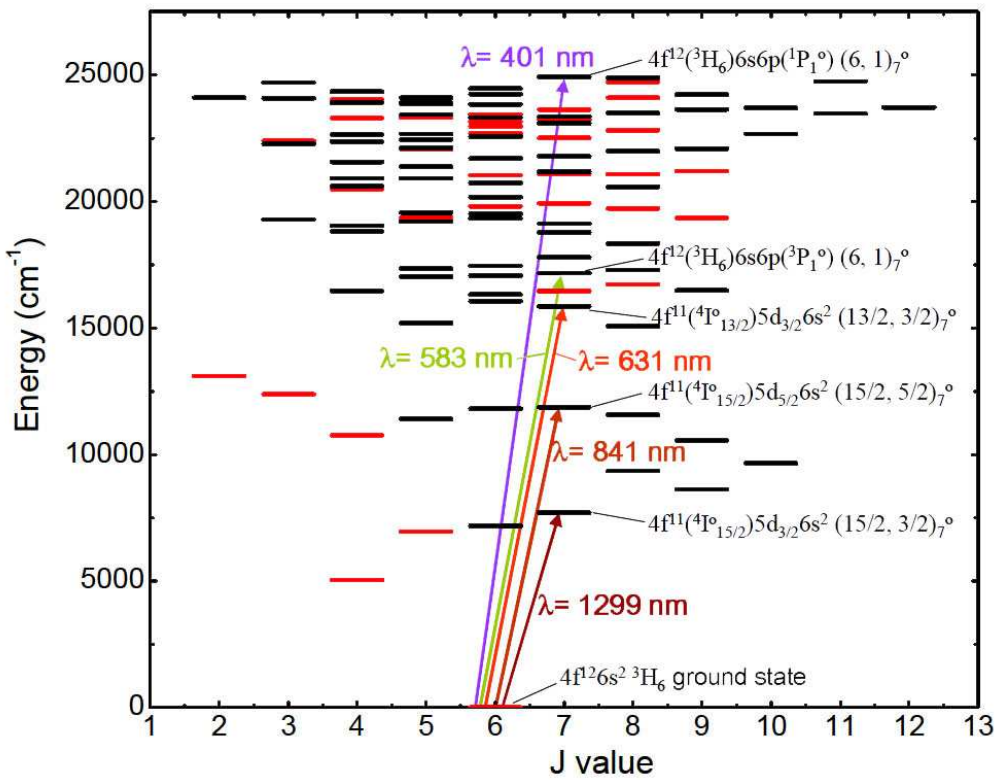

Figure 2.2: The energy level scheme of Er. Even parity states are indicated with red horizontal lines, odd parity states with black horizontal lines. The arrows show electric dipole transitions investigated in [29], for our experiment the transitions at 401 nm and at 583 nm are of special interest. Plot and data from [29] and [59].

which is the most dominant type of transition, the total angular moment J has to change by ± 1 and the parity of the state must change [61].

The different energy levels arise from the occupation of different shells and from the coupling scheme of the electrons. The well known Russell-Saunders or spin-orbit (LS-) coupling is common for light elements, where the Coulomb interaction is dominant over the spin-orbit interaction. In this scheme, all individual electronic orbital angular momenta $\vec{l}$ and spins $\vec{s}$ of each electron add separately to a total orbital angular moment $\vec{L}$ and a total spin $\vec{S}$, which finally couple to a total angular moment $\vec{J} = \vec{L} + \vec{S}$ [39]. The resulting state is denoted by the term symbol ${}^{(2s+1)}L_J$. Accordingly with the usual spectroscopic notation [61], the L-states are labeled with letters as follows: .

L value	0	1	2	3	4	5	6	...
symbol	S	P	D	F	G	H	I	...

In the case of heavy elements, the spin-orbit interaction is comparable or stronger than the Coulomb interaction. The resulting coupling scheme is known

as jj-coupling. A special case of this is the J_1J_2-coupling, which is relevant for many excited states of the lanthanides [62]. In this scheme, the $4f$ electrons and the outer, remaining electrons couple independently in a LS-coupling scheme to states with total angular momentum $\vec{J_1}$ and $\vec{J_2}$. They add to a overall total angular momentum $\vec{J} = \vec{J_1} + \vec{J_2}$ and the resulting state is denoted as $(J_1, J_2)J$ term.

In the ground state of Er, the $4f^{12}6s^2$ electrons are coupled in a LS-coupling scheme to a $^3\mathrm{H}_6$ term with a total orbital momentum quantum number $L = 5$. This is exceptionally high, compared to the ground states of the alkali atoms, which all have $L = 0$. The excited states usually experience a higher spin-orbit interaction and follow the J_1J_2-coupling scheme. For instance, the excited state associated with the strong laser cooling transition at 401 nm is labeled as $[\mathrm{Xe}]4f^{12}(^3\mathrm{H}_6)6s6p(^1\mathrm{P}_1^0)\,(6,1)_7^0$, see Fig. 2.2. Here, one of the ground state $6s$ electrons is excited to the $6p$ shell. The 12 $4f$ electrons couple in a LS-scheme to a $^3\mathrm{H}_6$ term, the $6s$ and the $6p$ electron couple in a LS-scheme to a $^1\mathrm{P}_1^0$ term. These two states couple to a $(J_1, J_2)_J^0 = (6,1)_7^0$ term, where $J = 7$ and '0' indicates the odd parity.

2.3 Isotopes

Erbium possesses six stable bosonic and fermionic isotopes with relatively high masses m from 162 amu to 170 amu. Tab. 2.1 shows the natural abundance and nuclear spin quantum number I of the stable Er isotopes.

element	mass m [amu]	abundance [%]	nuclear spin I	statistic
erbium	162	0.1	0	boson
	164	1.6	0	boson
	166	33.5	0	boson
	167	22.9	7/2	fermion
	168	27.0	0	boson
	170	14.9	0	boson

Table 2.1: Natural abundance and nuclear spin of the stable erbium isotopes. Data from [63].

In the electronic ground state, Er has a total angular momentum quantum number $J = 6$. No bosonic isotope shows hyperfine structure, being $I = 0$. The ground state of the fermionic ^{167}Er with $I = \frac{7}{2}$ splits up into eight hyperfine states from $F = \frac{19}{2}$ to $F = \frac{5}{2}$. Compared to other fermionic alkali systems that were brought to quantum degeneracy as ^{40}K [9] or ^{6}Li [64], ^{167}Er shows an exceptionally high abundance of 22.9 %. The richness in isotope number gives us more flexibility in terms of scattering properties. This can be very facilitative, as in the case of Sr. Here, the least abundant of the four isotopes, ^{84}Sr, has been the

first to be Bose condensed thanks to its favorable scattering properties[4] [17, 18]. Later on, it even was used to cool the fermionic ^{87}Sr by interisotope collisions to quantum degeneracy [65].

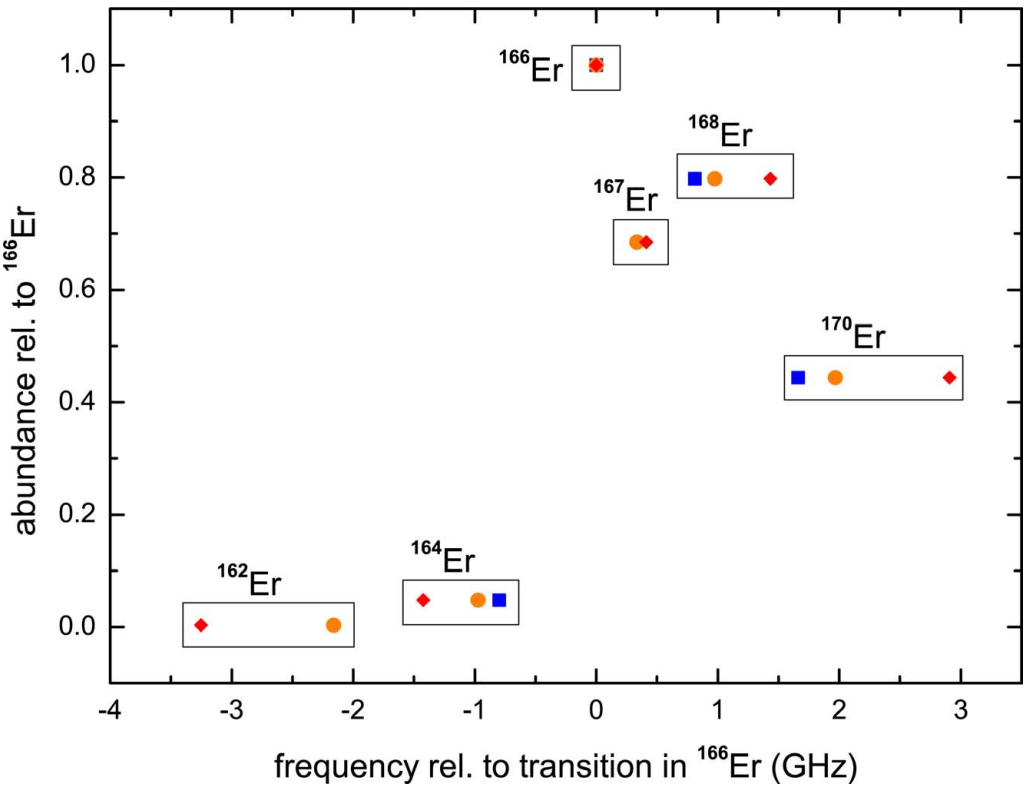

Figure 2.3: Natural abundance versus isotope shift for the 401 nm, the 583 nm and the 841 nm transition. ^{166}Er is taken as a reference. Data from [32, 66, 67], no values known for ^{162}Er and ^{167}Er at the 401 nm transition.

The laser cooling transition frequencies depend on the particular isotope. The different number of neutrons leads to different atom core masses and charge distributions and in that way the transition frequencies are shifted, what is called isotope shift [60]. Figure 2.3 shows the isotope shift of all stable isotopes for three transitions [32, 66, 67]. Taking ^{166}Er as a reference, the isotope shift is always less than 2.2 GHz for the 401 nm and the 583 nm transition. This is convenient since we can reach all isotopes at each transition within the same mode of the laser system.

[4] The scattering properties determine the thermalization of the atoms and thus are the key parameter for evaporative cooling.

2.4 Laser cooling of erbium atoms

The group of Jabez J. McClelland has identified five different transitions that could be used for laser cooling experiments, as illustrated in Fig. 2.2. Tab. 2.2 shows the accordant laser cooling parameters such as the natural linewidth $\Delta\nu$, the saturation intensity I_{sat}, the Doppler temperature T_{Doppler} and the recoil temperature T_{recoil} given in Ref. [29] with corrections from Ref. [68, 69].

parameter	transition				
	400.91 nm	582.84 nm	631.04 nm	841.22 nm	1299.21 nm
Γ (1/s)	2.2×10^8	1.2×10^6	1.8×10^5	5.0×10^4	13
τ	4.5 ns	0.857 μs	5.6 μs	20 μs	75 ms
$\Delta\nu$	35.6 MHz	0.19 MHz	28 kHz	8.0 kHz	2.1 Hz
I_{sat}	72.2 mW/cm²	0.13 mW/cm²	15 μW/cm²	1.8 μW/cm²	0.13 nW/cm²
T_{Doppler}	854 μK	4.8 μK	680 nK	190 nK	51 pK
v_{Doppler}	0.210 m/s	15 mm/s	5.8 mm/s	3.1 mm/s	50 μm/s
T_{recoil}	357 nK	170 nK	140 nK	81 nK	34 nK
v_{recoil}	6.0 mm/s	4.1 mm/s	3.8 mm/s	2.8 mm/s	1.8 mm/s

Table 2.2: The laser-cooling parameters for several transitions in Er [29, 68, 69]: spontaneous decay rate Γ, lifetime τ, linewidth $\Delta\nu$, saturation intensity I_{sat}, Doppler temperature T_{Doppler}, Doppler velocity v_{Doppler}, recoil temperature T_{recoil} and recoil velocity v_{recoil}.

The 401 nm transition has a broad natural linewidth $\Delta\nu = 36$ MHz, resulting in a strong scattering force

$$F_{\text{scat}} = \hbar\, k\, \frac{\Gamma}{2}\, \frac{I \,/\, I_{\text{sat}}}{1 + I \,/\, I_{\text{sat}} + 4\,\delta^2 \,/\, \Gamma^2}\,, \tag{2.2}$$

where $\Gamma = 2\,\pi\,\Delta\nu$ the spontaneous decay rate, $I_{\text{sat}} = \pi\, h\, c\, \Gamma \,/\, (3\,\lambda^2)$ the saturation intensity, I the intensity, $\hbar\, k$ the photon momentum and δ the detuning from the transition [60]. Therefore, we use this transition for the ZS to slow the thermal atomic beam, for transversal cooling (TC) to focus the atomic beam and for the imaging. This transition can also be used for a MOT [33], but for our MOT we want to take advantage of the narrow linewidth $\Delta\nu = 0.19$ MHz of the 583 nm transition, which has a lower Doppler temperature[5] T_{Doppler} of 4.8 μK. Due to the high mass m of Er, the recoil temperature[6] T_{recoil} of 170 nK is also very low. The ZS is designed to slow the atoms to 5 m/s, which is on the order of the capture velocity of the MOT. Therefore, it will be feasible and benefical to use the 583 nm transition to capture and further cool the slowed atoms in the MOT.

[5] The Doppler temperature $T_{\text{Doppler}} = \frac{\hbar\,\Gamma}{2\,k_{\text{B}}}$ is the fundamental temperature limit for the Doppler cooling mechanism [60].

[6] The recoil temperature $T_{\text{recoil}} = \frac{\hbar^2\,k^2}{m}$ is the fundamental temperature limit for sub-Doppler cooling mechanisms [60].

In usual alkali gas experiments, the cooling transition needs to be optically closed. Otherwise atoms leaking to metastable states get lost from the cooling cycle. As demonstrated in Ref. [33], this requirement is much less restrictive for Er atoms. Considering the energy level diagram in Fig. 2.2 and the electric dipole selection rules[7], it is clear that the 401 nm cooling transition is optically open. In particular, excited atoms can decay[8] to any energetically lower lying metastable state of opposite parity and $J = 6, 7$ or 8. In Ref. [33] the branching ratio for this transition is determined to 8×10^{-6}, so in every 1.3×10^5 transitions to the ground state, the excited state once decays to a metastable state. Depending on the number of required cooling cycles, this can limit the atomic population. However, atoms in such metastable states can be trapped by the quadrupole magnetic field of the MOT because of their high magnetic moment μ, as reported first in Ref. [33] and later in Ref. [70]. Thus, non-resonant metastable atoms cascade back to the ground state, from where they can be recaptured by the MOT beams. So in the 401 nm transition, despite the numerous loss channels, the atoms can be recycled due to the high magnetic moment that confines the atoms to the vicinity of the MOT beams.

We find the 583 nm transition particularly suitable for MOT operation. Here, excited atoms can decay to two metastable states, but since the energy change such transitions is very small, the transition rate is also small according to the Fermi golden rule, leading to a branching ratio of 2×10^{-8}.

Erbium is very favorable for the use of polarization gradient cooling, since the magnetic moments of many excited states are very similar to the one of its ground state. The Landé g-factors[9] of ground and excited state differ only by 0.004 for the 401 nm transition and by 0.03 for the 583 nm transition[10] [59]. Sub-Doppler cooling mechanisms rely on Zeeman shifts of the ground state sublevels, whereas Doppler cooling relies on Zeeman shifts of the ground state versus the excited state. Therefore, there is a critical magnetic field value above which the Doppler cooling dominates, as explained in [71,72]. Clearly, for smaller differences of the g-factors of ground and excited state, this critical magnetic field value is higher and the sub-Doppler cooling is less sensitive to magnetic fields. Therefore, especially the 401 nm transition is very suitable for polarization gradient cooling, as demonstrated in Ref. [58] and also in similar work on Dy [28].

[7] In emission, J can change to $J' = J \pm 1$ (stimulated emission) and also to $J' = J$ (except for $J = 0$) (spontaneous emission). The parity symmetry has to change in both cases [61].

[8] In a first order approximation, we only consider decay via the electric dipole radiation and neglect the weaker decay via electric quadrupole or via magnetic dipole transitions, which would involve odd parity states with J values from 5 to 9.

[9] The magnetic moment μ is proportional to the Landé g-factor of the state, see Eq. (2.3).

[10] $g[4f^{12}6s^2\,{}^3\mathrm{H}_6] = 1{,}16381$, $g[4f^{12}({}^3\mathrm{H}_6)6s6p({}^1\mathrm{P}_1^0)\,(6,1)_7^0] = 1{,}160$, $g[4f^{12}({}^3\mathrm{H}_6)6s6p({}^3\mathrm{P}_1^0)\,(6,1)_7^0] = 1{,}195$

2.5 Magnetic properties

Compared with the maximum magnetic moment $\mu = 1\,\mu_\mathrm{B}$ of alkali atoms, most of the lanthanide elements have high magnetic moments. Tab. 2.3 shows the electronic configuration and the ground state magnetic moment μ of all lanthanide atoms [59]. There is a direct relation between the vacancy of the $4f$-shell and the magnetic moment [73]. As we explain in more detail in App. A, the Hund's rules [60] determine the ground state quantum numbers, which determine the Landé g-factor of the state. Since

$$\mu = g\, M_J\, \mu_\mathrm{B}, \tag{2.3}$$

with g the Landé g-factor, and M_J the magnetic quantum number of the total angular momentum, the magnetic moment is related to the occupation of the $4f$-shell. Erbium has $\mu = 7\,\mu_\mathrm{B}$, resulting from its $4f^{12}6s^2$ electronic ground state occupation: According to Hund's rules this configuration leads to a $^3\mathrm{H}_6$ ground state term with $M_J = 6$. This gives a Landé g-factor of 1.16 and results in a magnetic moment of $6.98\,\mu_\mathrm{B}$.

element	**La**	**Ce**	**Pr**	**Nd**	**Pm**
e.c. ([Xe]-)	$5d^1 6s^2$	$4f^1 5d^1 6s^2$	$4f^3 6s^2$	$4f^4 6s^2$	$4f^5 6s^2$
μ [μ_B]	1	4	3	2	1

Sm	**Eu**	**Gd**	**Tb**	**Dy**
$4f^6 6s^2$	$4f^7 6s^2$	$4f^7 5d^1 6s^2$	$4f^9 6s^2$	$4f^{10} 6s^2$
0	7	5	10	10

Ho	**Er**	**Tm**	**Yb**
$4f^{11} 6s^2$	$4f^{12} 6s^2$	$4f^{13} 6s^2$	$4f^{14} 6s^2$
9	7	4	0

Table 2.3: The ground state electronic configuration ('e.c.') and ground state magnetic moment μ (rounded, in units of μ_B) of all lanthanides listed by rising atom number. All lanthanides have a complete Xe configuration, $\mu\,/\,\mu_\mathrm{B} = g\, M_J$, values from [59].

The quantum behavior of Er gas is expected to be strongly affected by its magnetic properties. The interaction energy of two magnetic dipoles aligned by a polarizing magnetic field is

$$U_\mathrm{dd} = \frac{C_\mathrm{dd}}{4\,\pi} \frac{1 - 3\,\cos^2(\theta)}{|\vec{r}|^3}, \tag{2.4}$$

where $C_\mathrm{dd} = \mu_0\, \mu^2$ is the coupling constant, $\vec{r}$ the relative coordinate of the two dipoles and θ is the angle between $\vec{r}$ and the dipole axis [20]. This means that for Er with $\mu = 7\,\mu_\mathrm{B}$ the dipole-dipole interaction (DDI) is 49 times stronger than

for alkali atoms with $\mu = 1\,\mu_\mathrm{B}$ since $C_\mathrm{dd} \propto \mu^2$. Furthermore, the DDI is long-range and anisotropic since $U_\mathrm{dd} \propto |\vec{r}|^{-3} \cos^2(\theta)$. This has many consequences and is expected to give rise to novel collisional behavior. In the case of identical fermions ultracold collisions are blocked by the Pauli exclusion principle due to the symmetry of s-wave scattering. The anisotropy of the DDI could enable such collisions by introducing higher partial waves [21]. In the case of bosons, the long-range character of the DDI might fundamentally change the universal scaling law of Efimov physics [74].

The dipolar-length $a_\mathrm{dd} = (m\,\mu_0\,\mu^2)\,/\,(4\,\pi\,\hbar)$, where μ_0 is the magnetic constant, is a measure for the absolute strength of the DDI [20]. Thus, the high mass m of Er further enhances its dipolar character. Additionally, the high μ and m should result in the observation of many Feshbach resonances already at low magnetic fields. Controlling the scattering length via Feshbach resonances is an important tool to reach quantum degeneracy and to produce tunable quantum gases [12].

2.6 Scattering properties

Important quantities as the background scattering length a, which determines the interaction at low temperatures are so far unknown. Its determination is the first goal of our experiment.

The use of evaporative cooling [75] is an important step for the achievement of quantum degeneracy. It is mostly performed in magnetic traps, but for non-S-state atoms collisional relaxation of the magnetic moments leads to rapid loss of atoms in a magnetic trap [76, 77]. Erbium is in an electronic H-state, but has a submerged shell structure, where the spherical symmetric $6s$-shell could suppress the interaction anisotropy of the H-state and effectively make it a S-state. This competition between open and closed shells can also be seen in the development of the investigation of the spin relaxation rates of Er in magnetic traps. In 2004 Hancox et al. studied collisions of He with Er in a He buffer gas cooled magnetic trap at temperatures below 1 K [31]. They successfully trapped Er and measured a suppression of the collisional transfer of angular momentum. Therefore, they concluded that in Er-He collisions the interaction anisotropy of the Er atoms is shielded by the two unpaired electrons. This gave hope that this would also hold for Er-Er collisions. However in 2010, Connolly et al. measured large spin relaxation rates of Er in a magnetic trap at temperatures of 500 mK [32]. The rates are significantly higher than those of highly magnetic S-state atoms and in striking contrast to the previous work. Although there are currently no theoretical predictions for Er-Er collisions, they explain the rapid loss by an additional spin relaxation mechanism despite spin exchange, dipolar relaxation or second-order spin-orbit coupling, which is induced by the electronic interaction

anisotropy. This means that magnetic trapping of Er will be highly inefficient. Therefore, in our experiment, we will use an optical dipole trap (ODT) to perform evaporative cooling of Er.

Chapter 3

Experimental setup

For the production of an Er BEC and further experiments on ultracold Er and Er-Li mixtures, we set up a vacuum apparatus and several laser systems. In the vacuum chamber, a thermal beam of Er atoms is produced in an oven and subsequently the atoms are slowed, trapped and further cooled by magnetic fields and laser light. In this Chapter, we give an overview of the experimental setup and the cooling strategy to produce a BEC of Er atoms.

3.1 Vacuum chamber

Figure 3.1 shows a drawing of the complete vacuum chamber, which is composed of five main sections: (a) Er oven chamber, (b) Li oven chamber, (c) Zeeman slower (ZS), (d) magneto-optical trap (MOT) chamber and (e) pumping chamber.

The Er oven chamber consists of a commercial oven system, which produces an Er atomic beam by the effusion of solid Er at temperatures up to 1350 °C. A detailed discussion of the Er oven is found in Chap. 4. In brief, the oven system consists of a crucible surrounded by a water cooled thermal shield. The crucible is divided in two parts: the effusion cell, where solid Er is placed and the hot lip, which contains two heated apertures. The emerging atomic beam has a most probable velocity of about 415 m/s at a temperature of 1350 °C. The oven system is followed by an octagon, which gives optical access at five CF40 viewports. Here, as indicated with the blue arrows, we can apply transversal cooling (TC) [78] using the strong 401 nm transition. By cooling the atoms transversely with red detuned light in a 2D optical molasses, their transversal velocity components are reduced and thus the atomic beam is further collimated. Via the moveable bellow on top, it is possible to place an Al mirror at the beam axis under an angle of 45 ° in respect to the beam axis. In this way, we can check the atomic beam path towards the MOT chamber and the injection of the ZS light. On the

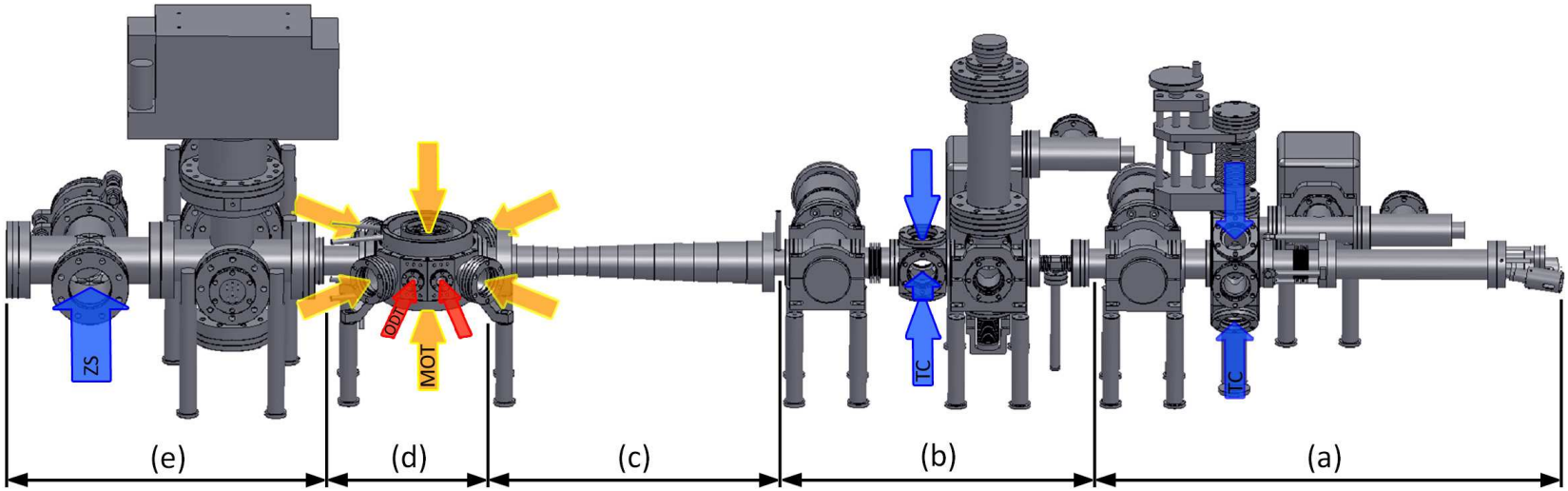

Figure 3.1: Drawing of the complete vacuum chamber, which consists of: (a) Er oven chamber, (b) Li oven chamber, (c) ZS, (d) MOT chamber and (e) pumping chamber. Red arrows indicate the 1064 nm light, which we use for the ODT, yellow arrows show the 583 nm MOT beams, blue arrows mark the 401 nm light for the ZS and TC.

backside of the octagon we connect an ion pump[1], an ionization gauge[2] and an all metal angle valve, which is used to attach a turbomolecular pump system[3] for pre-pumping. The Er oven chamber is separated by an all metal transition valve from the rest of the chamber to allow refilling of the oven without loosing the vacuum conditions in the whole chamber.

In the adjacent Li oven chamber, we can admix Li atoms to the atomic beam. The Li oven[4] is situated below the beam axis and emits Li atoms in vertical direction. In a tube along the beam axis, which is divided alongside in three parts, Er and Li are combined to a joint atomic beam. In 2/3 of the tube's cross section, the Er atomic beam travels from the Er oven towards the ZS and MOT. Li atoms can enter the remaining 1/3 of the tube from below and are collimated to a longitudinal beam by microtubes inserted along the beam axis [79]. At the end of the tube, Er and Li atoms emerge towards the ZS and merge into a two species atomic beam. In the prime setup, where we focus on Er itself, this Li oven section is replaced by an ordinary tube. After the Li oven section, a four-way cross connects another pump section with an ion pump[1], an ionisation gauge[2] and an angle valve. On top, a Ti-sublimation pump[5] gives further pumping capacity on demand. From below, the atomic beam shutter can mechanically block the atomic beam via a tiltable bellow and a servo motor. Past this, another cube with four viewports allows further transversal cooling to collimate the beam. A bellow, which we use for the alignment of the complete chamber, connects the second valve, which is integrated for the same reason as the prior one.

The ZS is a spin-flip type σ^- slower with an independent magnetic offset field. For the ZS we use the 401 nm light, red detuned by about $16\,\Delta\nu \mathrel{\widehat{=}} 580\,\mathrm{MHz}$. The ZS is water cooled and contains a differential pumping tube. This 8 mm in diameter and 30 cm long tube maintains a pressure gradient of 10^3 between the oven chambers, where pressures of 10^{-9} mbar are sufficient, and the experimental chamber, where pressures of about 10^{-12} mbar are needed. After the ZS, the slowed Er atomic beam is expected to have a longitudinal velocity of $5\,\mathrm{m/s}$.

The slowed atoms are captured in the MOT chamber. We use the narrow 583 nm transition for MOT operation. The MOT consists of a six beam optical molasses and a quadrupole magnetic field. Depending on the available laser power and on the desired MOT size, the beams each have a diameter of up to 30 mm and the coils generate a magnetic field gradient of about $10\,\mathrm{G/cm}$. The Feshbach- and the curvature coils give an homogeneous offset magnetic field for the use of Feshbach resonances [12] and add curved magnetic fields for compensation

[1] Varian *Star cell 20 l*
[2] Varian *UHV-24*
[3] Pfeiffer *HiCube classic*
[4] The Li oven has the same design as the one already used in the FeLiKx experiment in Innsbruck [79].
[5] Varian *TSP filament-type*

or magnetic trapping. A pair of compensation coils, which compensates the magnetic field of the ZS is mounted on the front and back of the MOT chamber. All coils are water cooled. To compensate for residual magnetic fields of any direction, we install a compensation cage around the MOT chamber, which is not shown Fig. 3.1. To cool the atoms towards quantum degeneracy, we load the atoms from the MOT into a crossed optical dipole trap (ODT) at 1064 nm. For this, another four, smaller, CF16 viewports give optical access for two beams, which are sketched as red arrows.

To provide and measure pressures as low as 10^{-12} mbar, the pumping chamber is equipped with an ion pump[6], a Ti-sublimation pump[5] and an ionisation gauge[2]. For pre-pumping and the baking of the experimental chamber, a turbomolecular pump[3] can be attached by an angle valve. Since not all atoms from the atomic beam are captured by the MOT, but a large part will hit the end of the chamber, it is not possible to inject the 401 nm light for the ZS directly from the backside, because a coated window looses transmittance rapidly. A coated mirror suffers only small loss of reflectivity, as we measured in a test setup with the movable mirror from the Er oven section. The reflectivity of the Al mirror coated with Er was only 3 % lower than that of the uncoated mirror. Therefore, in the four way cross, we inject the ZS light towards the atomic beam with a 45 ° Al mirror from the side.

3.2 Cooling and trapping lights

A single-mode single-frequency (smsf) frequency doubled diode laser[7] provides light at 401 nm. It has an output power of 120 mW, which we use for ZS, TC and imaging. The linewidth of the laser diode of about 100 kHz is well below the natural linewidth of the 401 nm transition in Er. To prevent long-term frequency drifts we lock the laser to the atomic transition by a phase modulation transfer locking scheme. Figure 3.2 shows the optical setup of the locking scheme.

To lock the laser to the atomic transition frequency, we generate free Er atoms that can get resonant with the laser light. Since Er has a very high melting point temperature, it is inapplicable to use a vapor cell, as it is done for all alkali atoms [80]. Therefore, we use a hollow cathode lamp (HCL), which is a glass tube with Er coated cathodes and is filled with Ar buffer gas at a pressure of 4 mbar. By applying high voltage[8] to the electrodes, we produce an Ar plasma. The Ar ions are accelerated towards the cathode, hit it and sputter off Er atoms. This generates free, neutral Er atoms that we can use to lock the laser. To obtain an error signal for the lock, we use modulation transfer spectroscopy [81, 82], a

[6] Varian *Star cell 75 l*
[7] Toptica *DL-SHG pro*
[8] Typical values are a voltage of 125 V at a current of 7 mA.

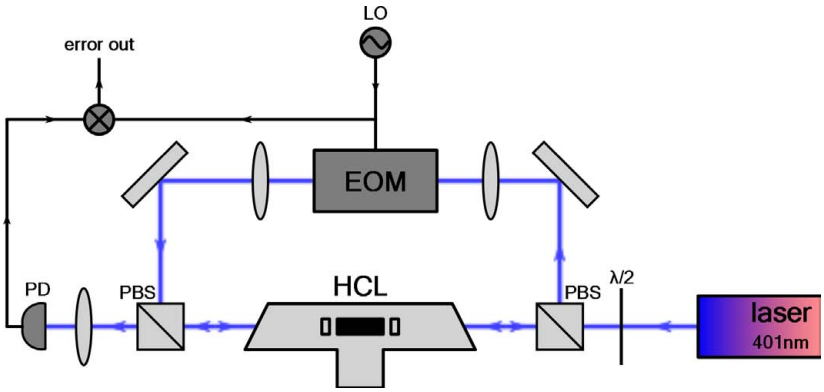

Figure 3.2: Scheme of the optical setup for the modulation transfer lock. In a hollow cathode lamb (HCL), free Er atoms interact can get resonant with the lower beam branch, the probe beam . The upper beam branch, the pump beam, is modulated with an electro optic modulator (EOM) before it enters the HCL. The probe beam signal is detected with a photodiode (PD). By mixing it with the local oscillator (LO) signal used for the EOM we gain an error signal for locking the laser to a certain Er transition.

pump-probe technique, which gives a Doppler-free spectrum. For this, the light from the laser is split with a polarizing beam splitter (PBS) into a probe and a pump beam. The pump beam is phase modulated with an electro optic modulator (EOM), which is driven with a local oscillator (LO) at a frequency of about 14.7 MHz. With another PBS we overlay counter propagating pump- and probe beam in the HCL. If the light is resonant with the Er atoms, the phase modulation of the pump beam is transferred to an amplitude modulation of the probe beam by nonlinear effects in the atoms. We detect the probe beam with a photodiode (PD) and mix it with the LO signal to allow phase sensitive detection. The generated signal has a flat baseline and a zero-crossing exactly at the transition frequency and thus can be fed directly to the laser system as an error signal for stable long-term locking. A typical signal of this modulation transfer spectroscopy is shown in Fig. 3.3. Here, four of erbium's five stable bosonic isotopes are clearly visible at the major zero-crossings of the signal, separated by the isotope shift. The residual zero-crossings, mainly in-between ^{166}Er and ^{168}Er, arise from the fermionic ^{168}Er, which is split into several hyperfine states. We can lock the laser to a certain isotope by the steep signal slope at the corresponding zero-crossing.

The MOT light at 583 nm is generated by a dye laser[9], which we pump with a 10 W smsf solid state laser[10]. The current master work of Alexander Rietzler is the development of a locking scheme for the dye laser. It needs to have smsf operation at an output power of 700 mW and a stability and linewidth of 100 kHz[11].

[9] Radiant Dyes *cw-ring-laser*
[10] Coherent *Verdi V10*
[11] This is required, since the natural linewidth of the 583 nm transition in Er is 170 kHz.

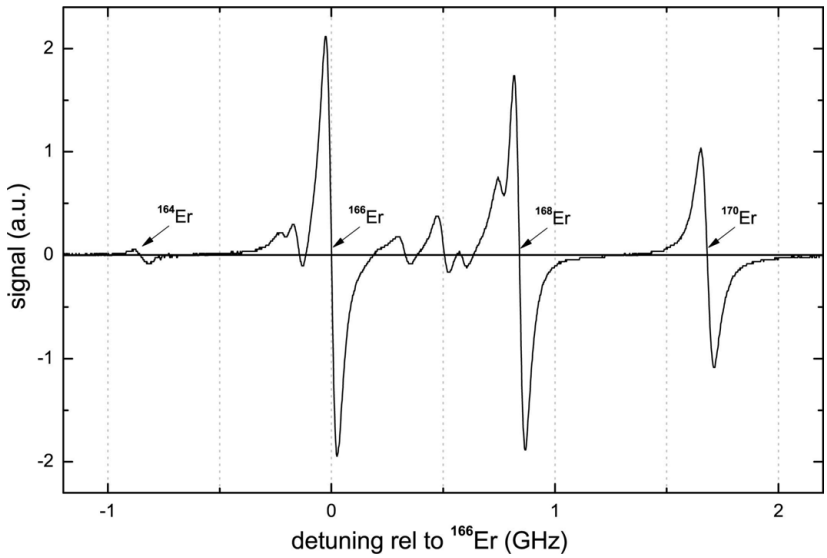

Figure 3.3: A typical signal of the modulation transfer spectroscopy on the HCL. Four of erbium's five bosonic isotopes are clearly visible at the major zero-crossings of the signal, separated by the isotope shift. The residual zero-crossings, mainly in-between ^{166}Er and ^{168}Er, arise from the fermionic ^{168}Er, which is split into several hyperfine states. Due to the signal's steep slope at the transitions and its flat baseline, it provides an excellent error signal for the locking of the laser system.

For this, he will stabilize and lock the laser with an external cavity. The light for the ODT at 1064 nm is produced by a smsf solid state laser[12]. Since a ODT operates far off detuned and the laser offers a good intensity stability, no special frequency- or intensity stabilization is needed.

[12]InnoLight *MEPHISTO MOPA 18 W*

Chapter 4

Erbium oven

We produce a thermal Er atomic beam from a commercial oven operating at about 1200 °C. The oven consists of an effusion cell, where few gram of solid Er are sublimated, and two separately heated apertures, which collimate the atomic beam. For thermal shielding, the high-temperature oven is water cooled. In this Chapter, we first describe the setup, the working principle and the home built control- and safety system. Later, we discuss the atomic beam shutter, which we use to block the atomic beam prior the ZS.

4.1 Oven system

The complete oven system is manufactured by CreaTec Fischer & Co. GmbH[1]. The oven has a special design to fulfill the requirement of high-temperature operation, as needed for Er, which has a melting point temperature of 1529 °C [52]. The central part is the effusion cell (EC), where solid Er is heated. The adjacent hot lip (HL) consists of two apertures that collimate and direct the atomic beam emerging from the EC towards the ZS tube. For heat shielding, the whole crucible is surrounded by a water cooled cylinder. Figure 4.1 shows a technical drawing of the detailed setup.

The tantalum (Ta) crucible consists of the EC part, where we can insert 10 cm^3 of solid material, and the HL part, where a spacer fixes the first and second aperture. The apertures both have 5 mm inner diameter and are separated by 50 mm. The EC and the HL part are heated separately with Ta wires, fixed by a pyrolytic boron nitride spacer that provides mechanical stability and electrical insulation even at high temperatures. This whole section is surrounded by a water cooled cylinder and integrated in a steel tube with a CF40 flange connection to the main chamber. A bellow allows to adjust the orientation of the oven. The power supply for the heating wires and the temperature sensors are feed through

[1] Model: Dual Filament Effusion Cell *DFC-40-10-290-WK*.

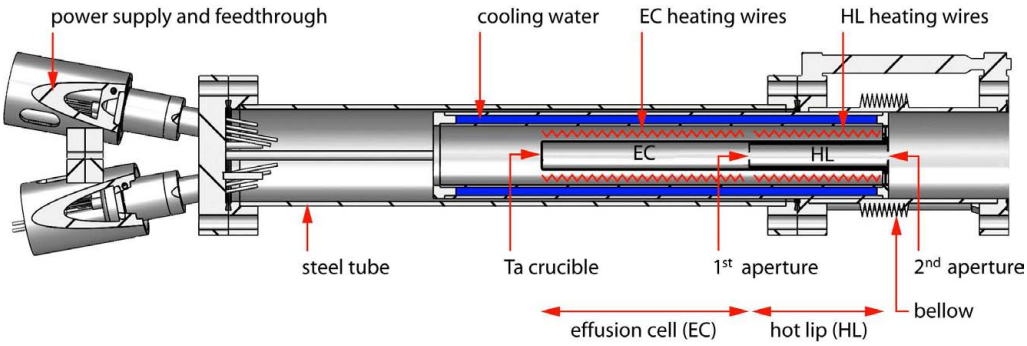

Figure 4.1: Schematic, sliced view of the Er oven. It consists of a crucible with EC and HL, two separate heating wires, a water cooling system and a tiltable housing with connections for power supply and temperature sensors.

at the back end of the oven by ceramic spacers.

The heating wires heat the EC and the HL radiatively. The specified temperature range is $100 - 1400\,^{\circ}\mathrm{C}$, the PID controller provides a stability of better than $0.1\,^{\circ}\mathrm{C}$. Temperature ramps should not exceed $30\,^{\circ}\mathrm{C}/\mathrm{min}$, to allow thermalization with Er and reduce the stress on the crucible. The maximum EC and HL heating wire currents and the corresponding heating powers are 3.5 A and 6.1 A as well as 84 W and 220 W respectively [83]. Typical operation temperatures for the EC range between $1000\,^{\circ}\mathrm{C}$ and $1350\,^{\circ}\mathrm{C}$, depending on the required flux. This temperature is still well below the melting point of Er of $1529\,^{\circ}\mathrm{C}$ because liquid material can break the crucible when cooling down the oven. Since we can heat EC and HL separately, we typically use the HL at $100\,^{\circ}\mathrm{C}$ higher temperatures than the EC to prevent material condensation at the apertures. This is an essential feature, since in related experiments[2] with Cr, condensed Cr has been observed to grow over the aperture and to lead to a short circuit of the heating wires.

The thermocouple temperature sensors are attached outside of the crucible. This implies that the measured temperature can differ from the actual temperature of the Er inside the crucible by few percent and we thus can use it only as a guiding value. The water cooling system shields the vacuum chamber from the high temperatures. It requires a water flow of $2\,\mathrm{l}/\mathrm{min}$ at $5 - 10\,^{\circ}\mathrm{C}$ water temperature and maintains a temperature of less than $100\,^{\circ}\mathrm{C}$ all over the oven section vacuum chamber. The oven system has to be operated in vacuum, it is specified from a maximum pressure of 1×10^{-5} mbar down to the UHV regime. To provide this, we use a turbomolecular pump and an ion pump, as discussed in Sec. 3.1.

The high temperatures involved also require a careful material engineering. We chose Ta for all parts of the crucible and for the wires. Tantalum has the advantage to have a very high melting point of more than $3000\,^{\circ}\mathrm{C}$ and to not create

[2]Private communication: Tilman Pfau, Universität Stuttgart.

low-temperature-melting alloys with Er, as demonstrated by the Er experiment at the NIST. In contrast, Ta and Cr form a low-temperature-melting alloy, so in this case, ceramic or other materials have to be used for the crucible [51].

A valve separates the oven chamber from the UHV part, so that we can keep the vacuum in the MOT chamber while refilling the oven. For the first oven operation, we clean the parts in a supersonic bath of acetone first, then of isopropanol and work in a clean environment. We cut Er pieces from an Er block and fill the bare crucible with typically 6 g of Er before we reassemble the crucible and the oven system. The insertion or removal of the crucible into the oven system must be done carefully in order to guarantee collinear alignment, since the heating wires can easily be damaged. Also the power and temperature connection must be handled with special care, since the ceramic spacers of the feedthroughs can break.

4.2 Control system

To control the high-temperature oven system and to secure it against power break down and cooling water failure, we set up a control system as schematically illustrated in Fig. 4.2.

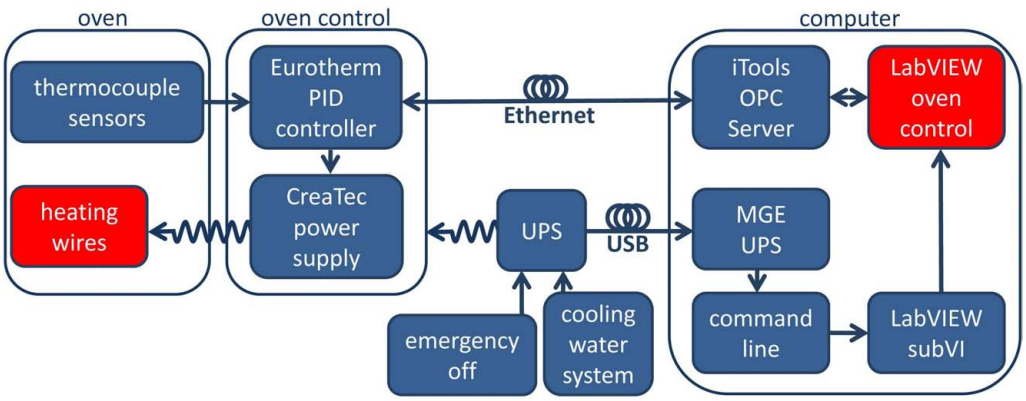

Figure 4.2: Structure of the Er oven control system. We control the oven from the computer via the oven control. We protect the oven control against power failure with an uninterrupted power supply (UPS), which we coordinate with the safety systems.

A CreaTec power supply unit with two power circuits supplies the heating wires of EC and HL. It is controlled by two Eurotherm precision proportional-integral-derivative (PID) controllers, which get feedback from the thermocouple sensors. The controllers can be monitored and set manually onboard, or by a computer connected via Ethernet. The iTools *OPC Server* program manages the PID controller variables, which we read and write in the LabVIEW oven

control program. In this way we monitor the actual temperature, the working setpoint temperature and the current output power and can set the temperature setpoints[3] and the temperature ramps.

Power failure can cause repeatedly, abrupt temperature ramps that damage the crucible. Therefore, we backup the power supply and the PID controller with an uninterrupted power supply (UPS), which is connected to the computer via an USB port. Here, the MGE UPS program manages the UPS variables, and executes the command line in case of variable changes. The command line itself starts a LabVIEW subVI executable that updates the UPS status in the LabVIEW oven control program. Therefore, in case of power failure, if the remaining supply time of the battery falls below a preset value, we cool down the EC and HL heating wires in a controlled way to the standby temperature, from which a sudden power-off does not harm the crucible.

The status of the cooling water system and the emergency off system are connected to the interlock of the UPS. In case of failure of the cooling water supply for the oven, as too low water backflow or leaks, this triggers an instant power off of the UPS and thus of the heating wires. This is crucial since without sufficient cooling water flow, the oven will overheat and vaporize the cooling water, which can damage the oven.

Hence, to operate the oven, the emergency-off system has to be inactive, the cooling water must run, the UPS and the power supply unit have to be switched on and the program iTools *OPC Server* must run. Then, the LabVIEW oven control program can be started to control the heating wires.

Figure 4.3 shows the user interface of the oven control program, App. B gives a detailed description of the program code. The user sets the EC and HL temperatures and the heating or cooling ramps in the commensurate displays of the two upper sub windows. Note that both values are protected against fault input. For operation at preset temperature setpoints, the 'ON' button changes between default temperature setpoints for working or standby operation. Further displays show the present temperatures, working setpoints, target setpoints, the thermocouple sensor status and the actual output power. The central part is a graph showing the actual and the working setpoint temperature in real time. In Fig. 4.3, the graph displays the initial heating up phase from 'OFF' to 'ON' mode. The straight lines mark the evolution of the working setpoints, which result of the target setpoints and the temperature ramps. The actual temperature values oscillate around the ideal values since the current limitation on the power supply is set to values that are optimized for the 'ON' mode. EC and HL temperature oscillate alternately; this shows that although the two PID controllers work independent of each other, the EC and HL system are coupled via radiation inside the oven. The 'enable values' button in the lower left of the screenshot allows to adjust

[3]The setpoint is the final obliged value, the working setpoint is the present obliged value.

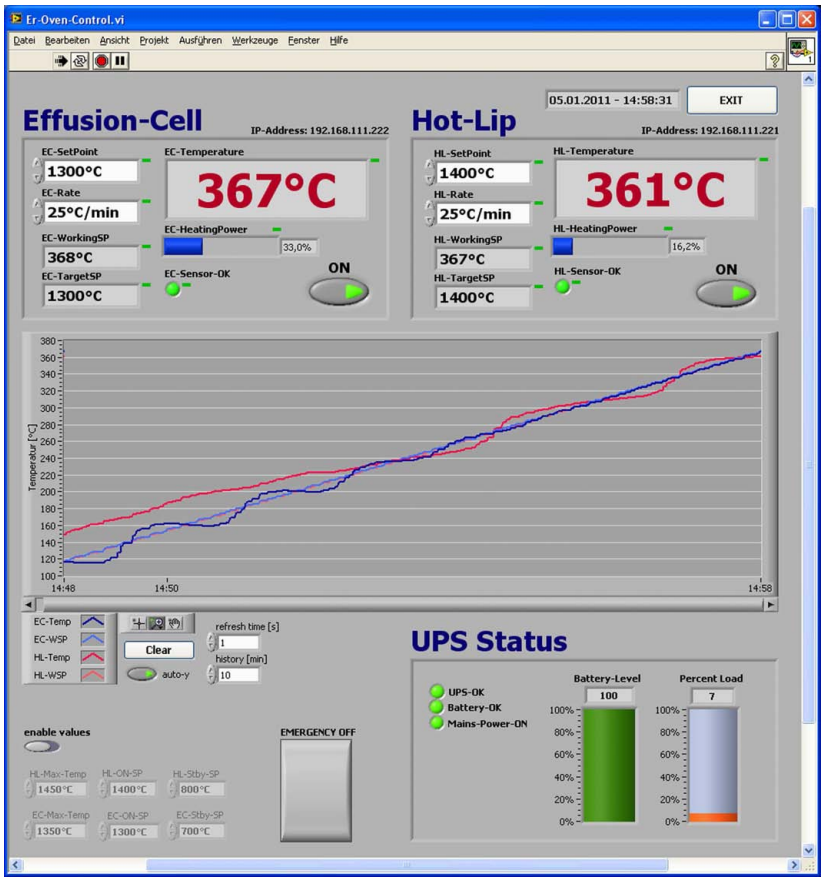

Figure 4.3: A screenshot of the oven control program user interface. We can set and monitor EC and HL temperatures on the computer. The program also reacts to the status the UPS.

the preset values for the temperature limits and the 'ON/STANDBY' temperatures. The 'EMERGENCY OFF' button at the lower middle of the interface sets the temperature setpoints and working setpoints to zero. This switches off the heating and the oven cools down as fast as possible. The subwindow 'UPS status' shows the status of the UPS variables. The program automatically reacts to changes of the backup time of the UPS.

4.3 Atomic beam shutter

For each experiment cycle, we will load the MOT with atoms coming from the Zeeman slowed beam. After the MOT phase, the atoms are lead into an ODT. At this point, the atomic beam should be blocked to leave the already optically trapped atoms unperturbed. Therefore, it is of prime importance to install an atomic beam shutter between Li oven and ZS section. The beam shutter is a mechanical shutter, which is driven by a servo motor. A control box connected

(a) (b) (c)

Figure 4.4: Technical drawings of the atomic beam shutter. (a) The shutter unit, in position (1): 'blocked beam' and in position (2): 'unblocked beam'. (b) The servo motor with mounting. (c) The complete assembly to the vacuum chamber, here the atomic beam enters from the front and is blocked.

with the experiment computer controls the shutter operation.

Figure 4.4 (a) shows the beam shutter for the 'blocked beam' and the 'unblocked beam' position. The disc has a diameter of 20 mm and since this is considerably larger in diameter than the 275 mm distant differential pumping tube of the ZS with 8 mm in diameter, this ensures adequate blocking of the atomic beam. A little bar connects the disc with the lower end of a bellow, which we attach to the vacuum chamber. Two ball bearings on the side arms, which we tighten with springs[4] allow tilting of the bellow. Figure 4.4 (b) shows the mounting of the servo motor. It is fixed to the posts of the chamber, and connected to the lower end of the bellow with a little bar. The servo motor has a metal gear to provide a long lifetime, and a torque of approximately 150 Ncm, which is sufficient to tilt the bellow. It is specified to rotate by 40 ° in 0.17 s at a supply voltage of 6 V, this sets the limit of the shutter speed. As common for servo motors, it is controlled with a pulse width modulated (PWM) signal. This signal has a period of 20 ms and an amplitude of 5 V. By modulating the width between 1 ms and 2 ms, we can set the position of the shutter. Figure 4.4 (c) illustrates the complete assembly of the shutter system. In this view, the atomic beam enters from the front and is blocked by the shutter.

The atomic beam shutter control box connects the servo motor with the digital output box of the experiment control. For this, we use a microcontroller[5] (μC), which coordinates manual or digital adjustments and control. In App. C.1 the circuit diagram and the operating guidelines for the electrical details and right

[4]Not shown in the drawing.
[5]Atmel *AVR ATmega128*

(a) front view **(b)** side view

Figure 4.5: The atomic beam shutter control box with all connections, status LEDs and most switches. Switches for the adjustment of the shutter position are inside the box.

usage are given. The source code for the μC, which we wrote in the programming language C, and comments on it in App. C.2 give insight into the firmware structure. Below, we describe the features of the control box according to Fig. 4.5 and give a brief overview of the firmware structure.

The control box is powered with 5 V to 8 V via a BNC connector. This directly supplies the servo motor, whereas we supply the electric circuit with a 5 V voltage regulation. This division avoids unintentional resets of the μC and protects the μC against too high voltage. In case of a low signal on the emergency off connector, the control box aborts operation and blocks the atomic beam. The experiment control sends a TTL signal to the control box. It has either a 'high' or a 'low' value and thus triggers the shutter position 'blocked beam' and 'unblocked beam'. To avoid groundloops, we do not connect the TTL signal directly to the μC, but via an opto-isolator[6], therefore it is inverted, the same holds for the emergency off signal. The switch 'pc/manual' changes from computer control to manual control, where the shutter position is set by the 'unshut/shut' switch. To calibrate the shutter position, we open the box, choose the manual mode and adjust the 'unshut' or 'shut' position by turning on the according potentiometer inside the control box. The connector 'con3' in Fig. 4.5 (b) offers to reprogram the μC via the programming adaptor without opening the box. Aside, the servo is attached. This connector[7] supplies the servo with power and sends the PWM control signal. The status LEDs display position and mode of the shutter and the shutter control. At initialisation, all LEDs shine for 1 s, blinking LEDs indicate an emergency blocking.

All these features result from the firmware of the μC. The basic working scheme relies on the following segments. A main while-loop uses interlaced if-loops to check the status of the control variables ordered by their importance:

[6]An integrated circuit (IC), providing galvanic separation by translating electrical information into optical information and backwards.

[7]For convenience, the connector is a case insensitive six pin connector, although only three pins for power, ground and signal are needed.

'emergency off', 'pc control', 'manual control', 'shutter positioning'. To control the servo, a timer interrupt runs every 10 ms[8]. If the value of the variable 'shutterpos', which determines the blocking of the atomic beam, changed within the last second, it sends the appropriate signal to the servo motor. Otherwise, it sends no signal and so leaves the motor at rest to avoid needless vibrations.

The interrupt, the PWM signal output and the analog to digital conversion[9] (ADC) are all features provided by the μC itself and are initialized together with the pin configuration in the beginning. In the end of the source code, we define the user defined functions for the positioning of the shutter via the potentiometers and the setting of the shutter position according to the manual- or the TTL signal input. The included header file defines constants, macros, variables and functions.

[8]This delay is negligible compared to the angular speed of the servo motor.

[9]The ADC converts the analog voltage values of the potentiometers, which we use for adjustment of the shutter position, to digital values, which the μC can process.

Chapter 5

Characterization of the atomic beam

We characterize the Er atomic beam using differential absorption spectroscopy. Already well below the melting point of Er, we observe a comparatively high atomic flux from the oven and an unexpected large spatial divergence of the atomic beam, indicating a large Doppler broadening. Based on our observations, we designed an optimized, new generation atomic beam collimation setup, which includes two apertures and a reducing-flux tube. In this Chapter, we describe the measurement setup and present our observations on beam divergence and atomic flux, performed on both the original and the optimized collimation setup, here referred to setup 1 and setup 2 respectively. A comparison of the performance of both setups is also given.

5.1 Measurement setup

To measure the atomic flux emerging from the Er oven and the divergence of the atomic beam, we perform spectroscopic measurements using the 401 nm transition. This is a comparatively strong transition with a linewidth of 36 MHz and a saturation intensity of $72\,\mathrm{mW/cm^2}$. It is well suitable for such a measurement since the resulting spectra provide strong signals. Figure 5.1 illustrates the optical setup. As discussed in Chap. 4, the Er oven system creates an atomic beam travelling longitudinally towards the MOT chamber, see Fig. 3.1. Our spectroscopic measurements are performed in the octagon chamber, which is located just before the Li oven section and the ZS tube. Here, five viewports guarantee good optical access. The 401 nm light enters the chamber and is intersected transversely with the atomic beam. If the light is resonant with the atomic transition, the atoms absorb the light, which then is spontaneously re-emitted.

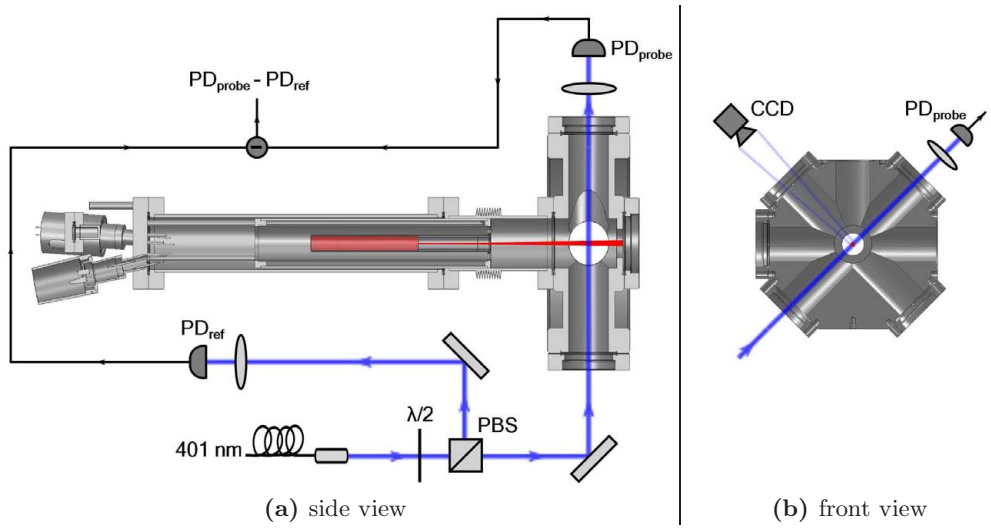

(a) side view **(b)** front view

Figure 5.1: The optical setup of the differential absorption spectroscopy and the imaging of the atomic beam fluorescence. (a) In the sliced side view of the oven chamber, a collimated atomic beam, drawn in red, leaves the Er oven. We split 401 nm light by a PBS into a reference beam, which falls directly on a PD and into a probe beam. The probe beam enters the octagon where it interacts with the atomic beam before it is detected by a PD. The difference of the two PD signals gives a signal free of global intensity fluctuations. (b) As shown in the front view, a CCD camera images the fluorescence perpendicular to laser and atomic beam, which travels into the plane of projection.

Absorption spectroscopy

We measure the absorption of light in a differential absorption spectroscopy setup as illustrated in Fig. 5.1(a). The absorption of light is detected by the photodiode PD_{probe}. By scanning the laser frequency, we record the absorption spectrum of the 401 nm transition for all stable isotopes. Since the atomic beam and the laser beam are perpendicular to each other, the spectral width provides information on the transversal velocity of the atoms and on the transversal Doppler broadening. To remove the background of the absorption signal, we use a differential setup. Here, a PBS splits the 401 nm light, transported with a fiber[1] from the laser-table to the experiment-table, into a probe beam and a reference beam. The intensity ratio of the two beams is adjustable by a half-wave plate. The reference beam power is measured directly by PD_{ref}. The probe beam passes through the chamber and interacts with the atoms before it is detected at PD_{probe}. Lenses[2] focus the laser beams onto the photodiodes. Within few percent, both beam paths have the same length of $\simeq$ 45 cm to equalize distortion effects that scale with

[1]In the setup characterized in Sec. 5.2 we use a polarization-maintaining singlemode Thorlabs *PM-S350-HP-custom* fiber of 10 m length. In the setup characterized in Sec. 5.3 we use a polarization-maintaining singlemode Schäfter + Kirchhoff *PMC-400Si-3.1-NA010-3-APC-800P* fiber followed by an additional PBS to clean the polarization further.

[2]With a focal lenght of 50 mm.

the length. The differential signal $\mathrm{PD_{probe}} - \mathrm{PD_{ref}}$ is free from global intensity changes, but is sensitive to intensity changes of the individual beams. To improve the signal further, we shield the chamber and the photodiodes from stray light and install an additional aperture in front of $\mathrm{PD_{probe}}$ to avoid back-reflections into the chamber.

The parameters and settings of the actual measurement are as follows. The laser beam power before the PBS is $60\,\mu$W, the radius of the laser beam is about 0.07 cm. Therefore, the intensity of the light is $I = 1\,\mathrm{mW/cm^2}$, which is well below the saturation intensity, $I \ll I_{\mathrm{sat}}$. To operate the laser on resonance, we lock the frequency externally via the HCL to the 401 nm transition of ^{166}Er, as discussed in Sec. 3.2. To scan the frequency, we use the scan mode of the laser system that simultaneously tilts the grating and changes the diode current of the seed diode laser. This results in a triangular frequency signal with more than 5 GHz peak-to-peak frequency amplitude and a period of 3 s at default settings. By this, the laser frequency can be scanned over the resonance without mode-hops in the doubling cavity. The differential PD signal is recorded with a digital storage oscilloscope. To achieve a good signal-to-noise ratio, all spectra are obtained by averaging the signal over more than 30 frequency scans. To calibrate the laser frequency in the scanning region, we measure the wavelength with a wavemeter[3] and combine this with the scan rate of the laser system. As discussed in more detail in App. D.1, this gives the frequency axis to the spectra recorded with the oscilloscope.

Fluorescence imaging

Additional to the absorption spectroscopy, we also image the fluorescence of atoms emitted in random directions with a CCD camera[4]. As shown in Fig. 5.1 (b), we mount the camera in front of an octagon chamber viewport, perpendicular to the laser beam. By this, we determine the laser-atom interaction length and estimate the cross section of the atomic beam. We place the camera about 20 cm from the chamber and we use a camera objective with large focal length, focused to the center of the chamber. A cover shields the camera from stray light. We calibrate the pixel size and the exposure time of the camera as described in detail in App. D.2. The exposure time needs to be short, not to saturate the CCD chip at high fluorescence light intensities and it needs to be long enough to detect low intensities. In setup 1, the optimal exposure time is 100 ms and the pixel size is $1\,\mathrm{px} \mathrel{\widehat{=}} 58.1\,\mu\mathrm{m}$. In setup 2, the optimal exposure time is 1 s and the pixel size is $1\,\mathrm{px} \mathrel{\widehat{=}} 42.8\,\mu\mathrm{m}$.

Figure 5.2 shows a typical CCD image of the fluorescence light of the atomic beam. In this view, the atomic beam is entering the image from the right side,

[3] HighFinesse *WS/7*
[4] MATRIX VISION *blue fox*

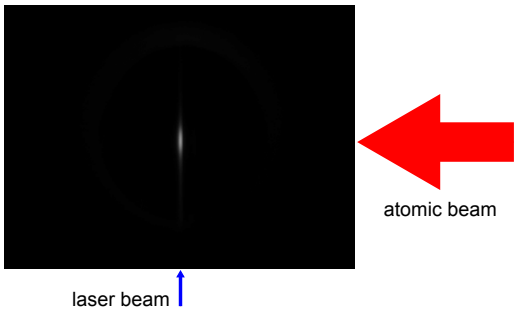

Figure 5.2: A typical CCD image of the fluorescence light of the atomic beam. In this view, the atomic beam is entering the image from the right side, the laser beam from the bottom, as indicated by the arrows (not in scale). Reflections of the light in the chamber are removed by a reference image. Only the parts of the atoms whose resonance frequencies are Doppler shifted by less than the natural linewidth of the transition are resonant and fluoresce. From such an image we derive the light-atom interaction length.

the laser beam from the bottom. Reflections of the light in the chamber are removed by a reference image. Only the parts of the atoms whose resonance frequencies are Doppler shifted by less than the natural linewidth of the transition are resonant and fluoresce. From such an image we derive the light-atom interaction length. In combination with the differential absorption measurement, we can deduce the flux of the atomic beam, as discussed in Sec. 1.3 and in Sec. 5.4.

5.2 Collimation setup 1

The collimation setup of the oven consists of a number of apertures placed right after the effusive oven. It determines the divergence of the atomic beam and its flux. The setup has to compromise between high flux and low atom loss. On the one hand, highly divergent atomic beams are useless in the experiments since only atoms in the central part of the beam can enter the ZS tube because of geometric limitation. On the other hand, strong collimation leads to an insufficient atomic flux.

In setup 1, we place two apertures in the oven section as schematically illustrated in Fig. 5.3. The first aperture, aperture 1, has an inner diameter $b_1 \simeq 5\,\mathrm{mm}$ and it is situated between the EC and the HL. At a distance $a \simeq 50\,\mathrm{mm}$ aperture 2, is installed with an inner diameter $b_2 \simeq 5\,\mathrm{mm}$. This second aperture has the main scope of collimating the atomic beam. At a distance of $l \simeq 83\,\mathrm{mm}$ from aperture 2, the probe laser beam transversely intersects the atomic beam. To characterize this setup before mounting the complete vacuum chamber, we assembled first the Er oven chamber, named section (a) in Fig. 3.1. Instead of the valve terminating the chamber, we placed a CF40 viewport.

As already pointed out in Chap. 1, the oven operates in the effusive regime. Using Eq. (1.1) and Eq. (1.2), we estimate the mean free path to be $\lambda_{\mathrm{mf}} \approx 4\,\mathrm{cm}$

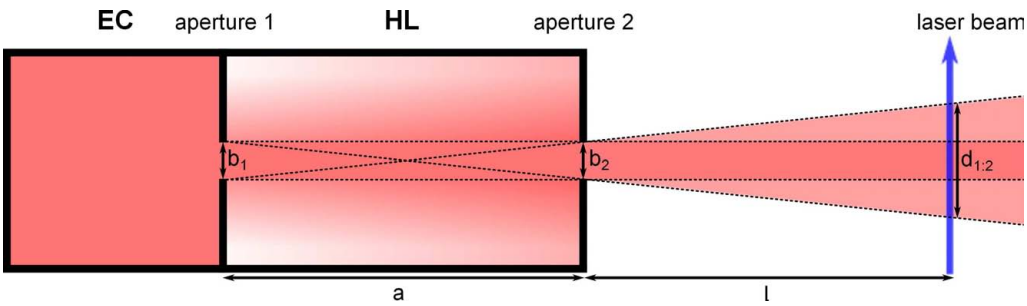

Figure 5.3: Scheme of collimation setup 1. Aperture 1, which separates EC and HL section and aperture 2, which collimates the atomic beam have both an inner diameter of $b_1 = b_2 \simeq 5\,\mathrm{mm}$ and are spaced by $a \simeq 50\,\mathrm{mm}$. At a distance of $l \simeq 83\,\mathrm{mm}$ from the aperture 2, the probe laser beam transversely intersects the atomic beam. The atomic beam diameter is expected to be $d_{1:2} = 22\,\mathrm{mm}$.

at a temperature of 1350 °C. Since the aperture dimensions are lower than λ_{mf} by an order of magnitude, we assume to be in the effusive regime.

Beam divergence

The atomic beam diameter at a certain distance from the EC is a measure of the beam divergence. By Eq. (1.8), for the geometry of setup 1 as illustrated in Fig. 5.3, we expect a diameter of $d_{1:2} = 22\,\mathrm{mm}$ at a distance of $a + l$ from the EC. We estimate the actual beam diameter d_{ex} by imaging the fluorescence of the atomic beam at the intersection with the laser beam. Since atoms with a radial velocity component $v_x \neq 0$ experience a Doppler shifted resonance frequency ν_0', we need to scan the laser frequency on a range exceeding the Doppler shift to image the complete atomic beam spectrum. Figure 5.4 shows such a measurement. Frames (a) to (i) represent negative fluorescence image sections, which are recorded in a time sequence. The atomic beam enters each frame from the right, the laser beam from the bottom, identical to Fig. 5.2. The laser frequency is scanned and increases from frame (a) to (i). Therefore, different sections of the atomic beam with different Doppler shifted resonance frequencies fluoresce on each frame, leading to an apparent motion of the fluorescence. The inhomogeneous shape of the fluorescence in frames (d) and (e) results from the fact that during the exposure time of 100 ms, the laser frequency is scanned by 200 MHz over the transversal atomic beam profile, leading to a distorted image. From frame (b) to (h) the fluorescence is visible in between the red dotted lines, spaced by 41 mm, which serve as a guide to the eye. However, the field of view of the CCD camera is of equal size and the edges of the total fluorescence region, are sharp and not smooth. Thus, it is likely that the actual atomic beam diameter is larger than the field of view. Therefore, we determine the lower bound of the atomic beam diameter to be $d_{\mathrm{ex}} \gtrsim 41\,\mathrm{mm}$.

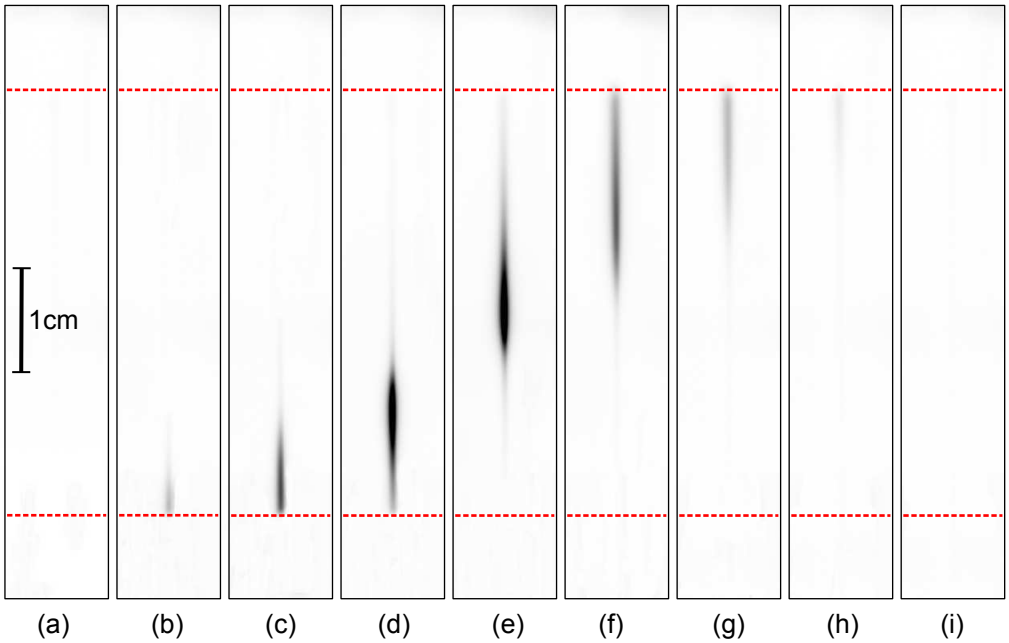

Figure 5.4: Fluorescence images, which are recorded in a time sequence. The atomic beam enters each frame from the right, the laser beam from the bottom. The laser frequency is scanned and thus is increased from frame (a) to (i). Therefore, different sections of the atomic beam with different Doppler shifted resonance frequencies fluoresce on each frame. The red dotted lines serve as a guide to the eye and signalise the region of fluorescence. A scale is given in frame (a) and to improve visibility we show the negative images.

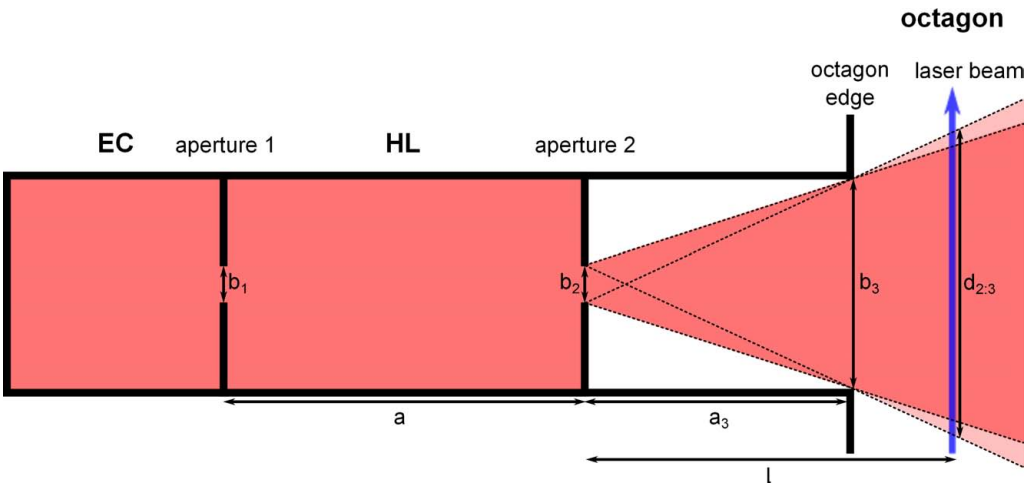

Figure 5.5: Scheme of the actual atomic beam in collimation setup 1. Atomic vapor fills both EC and HL part leading to an atomic beam that emerges from aperture 2 and is collimated at the inner edges of the octagon at a distance $a_3 \simeq 66\,\mathrm{mm}$ from aperture 2 with a diameter of $b_3 \simeq 38\,\mathrm{mm}$. For geometrical arguments, the resulting atomic beam is highly divergent and has a large diameter $d_{2:3} = 49\,\mathrm{mm}$.

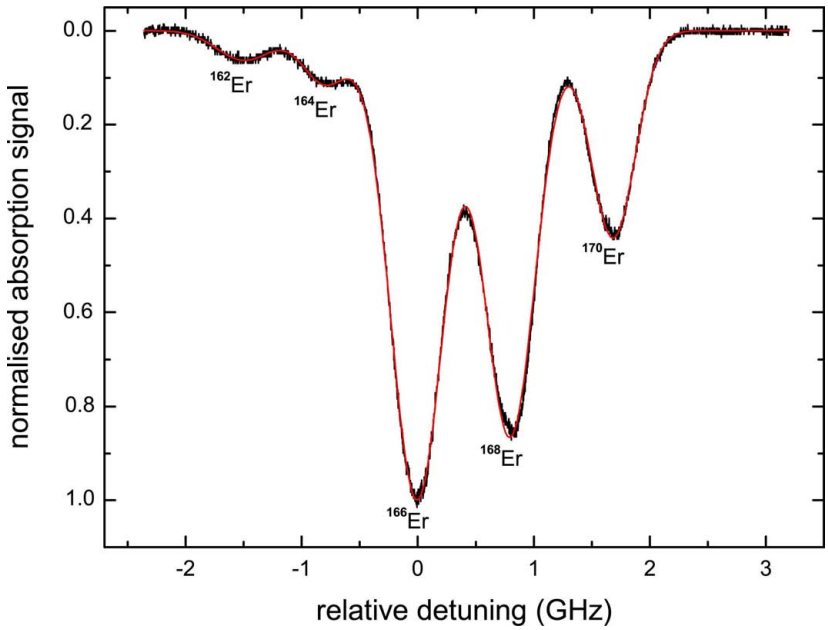

Figure 5.6: Transversal absorption spectrum at $T_{\mathrm{EC}} = 1350\,°\mathrm{C}$ and $T_{\mathrm{HL}} = 1450\,°\mathrm{C}$. The black line shows the differential signal, the red curve is a five peak Voigt function fit to the data. Five of the six stable Er isotopes are clearly resolved. The signal is normalized to the maximum absorption corresponding to a maximum optical density $OD_{\max} \simeq 0.21$.

This is a factor of 2 bigger than the value of $d_{1:2} = 22\,\mathrm{mm}$, which was expected for this collimation setup. A possible explanation for the large value of d_{ex} is to consider both the EC and the HL behaving as an effusive oven, as schematically illustrated in Fig. 5.5. As a consequence, the first aperture will not play any role in the collimation since similar to the EC, also the HL is filled with atomic vapor. This leads to an effectively shifted collimation setup: the atoms emerge from aperture 2 and are collimated at the proximate limiting structure, which is the octagon. The inner edges of the octagon chamber, which have a diameter of $b_3 \simeq 38\,\mathrm{mm}$ and a distance of $a_3 \simeq 66\,\mathrm{mm}$ from aperture 2, act as a third aperture. For such a collimation, we expect a beam diameter of $d_{2:3} = 49\,\mathrm{mm}$ what is in agreement with the lower bound of d_{ex}.

Spectrum

The large transversal divergence of the atomic beam is also confirmed by the absorption spectra. We measure the transversal absorption spectrum as described in Sec. 5.1. By this, we can directly measure the Doppler broadened width of the absorption signal and get information on the transversal velocities. Therefore, we can characterize the oven system also in dependence of its operation temperature.

Figure 5.6 shows the absorption spectrum recorded with the above described

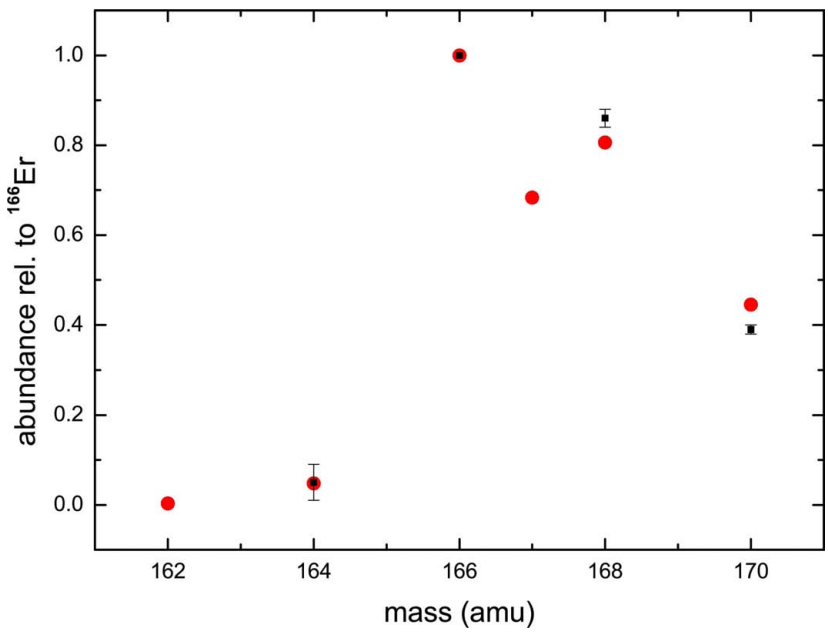

Figure 5.7: Abundance relative to ^{166}Er of the stable Er isotopes. The measured values, indicated as black squares, are in well agreement with the literature values [63], indicated as red circles. Since ^{162}Er has very low abundance, no reliable measurement result exists. ^{167}Er is split into eight hyperfine states and is not resolved in the measurement. The error bars are statistical over seven measurements.

setup 1. Since the EC and the HL part are operated at high temperatures of $T_{\mathrm{EC}} = 1350\,^{\circ}\mathrm{C}$ and $T_{\mathrm{HL}} = 1450\,^{\circ}\mathrm{C}$, the atomic beam has a high flux and absorbs 40 % of the incident light, leading to a distinct signal. All five stable bosonic isotopes of Er are clearly resolved. According to Eq. (1.26), we fit a Voigt function to the data from which we determine the peak positions and the width. The fitted Voigt function shows a vanishing small Lorentzian contribution, thus we can treat it as a pure Gaussian function.

Isotopic composition and isotope shift

The area of each individual absorption peak gives information on the isotope abundance. For an accurate determination, we average over seven different measurements at different operation temperatures. Comparing the measured values normalised to ^{166}Er with the natural abundance reported in literature [63], we find overall good agreement for ^{164}Er, ^{168}Er and ^{170}Er as shown in Fig. 5.7. Because of the low abundance of ^{162}Er of 0.1 %, we can not give a precise value. ^{167}Er is split into eight hyperfine states and is not resolved in the spectrum. The error bars account for the statistical error of the seven measurements.

The peak positions provide information on the isotope dependent frequency shift. Figure 5.8 compares the measured values to the literature values [32]. As

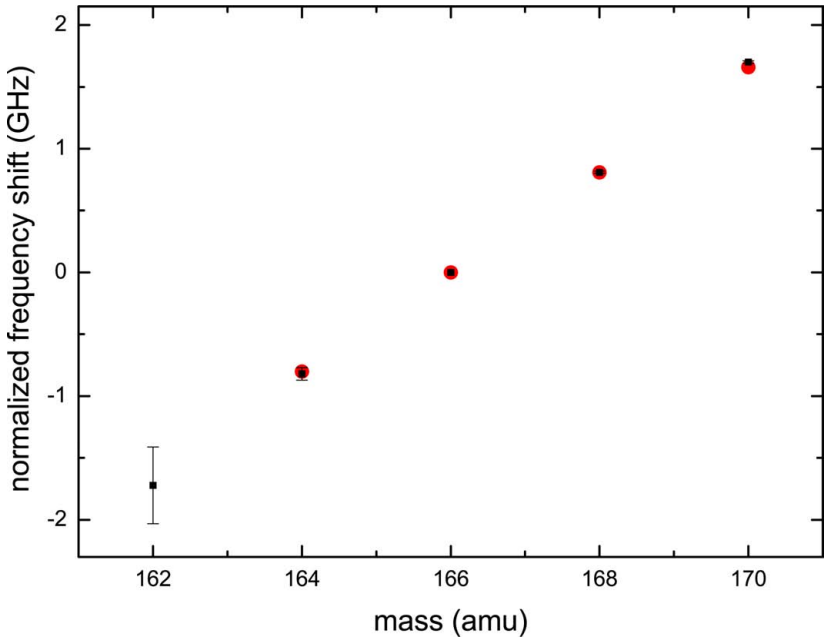

Figure 5.8: Frequency shift of the 401 nm transition relative to ^{166}Er for all stable bosonic isotopes of Er. The measured values, indicated as black squares, are in very good agreement with the literature values [32], indicated as red circles (no known value for ^{162}Er). The error bars are statistical over seven measurements.

before, the results are mean values of seven measurement sets, leading to a statistical error estimation. All values known from literature, also shown in Fig. 2.3, agree very well with our results. For ^{162}Er, to our knowledge no literature value exists, but our measured value fits to the slope of 400 MHz frequency change per atomic mass unit (amu) observed at the other bosonic isotopes.

Line shape and linewidth

In absence of any broadening mechanisms, the absorption spectrum has a Lorentzian line shape with a width given by the natural linewidth $\Delta\nu_{\mathrm{nat}}$, which is determined by the inverse lifetime of the excited state. For the 401 nm transition $\Delta\nu_{\mathrm{nat}}$ is 36 MHz. In our measurements, we always observe a linewidth bigger than the natural one, meaning that the spectrum is affected by some broadening mechanism. The shape of the absorption spectrum gives information on the underlying broadening mechanism. A Gaussian shape is most probably ascribed to Doppler broadening, while a Lorentz type shape can arise from saturation or collisional broadening. For mechanisms of equal strength, the profile is represented by a convolution of the contributing line shapes, namely a Voigt profile. In this first measurement set, we always observe a pure Gaussian profile and assume that Doppler broadening is the most dominant broadening mechanism. The error bars shown in all following graphs refer to the statistical error coming from the fit of

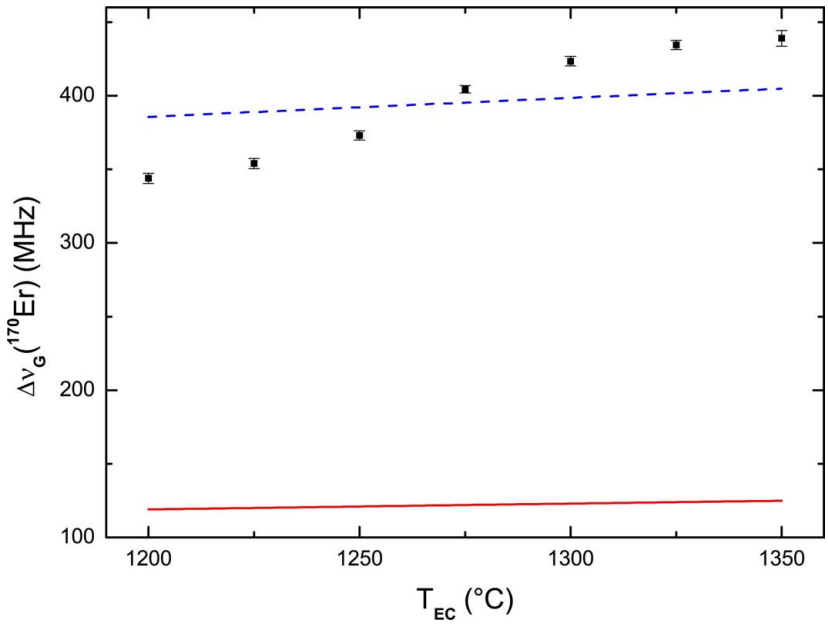

Figure 5.9: The Gaussian linewidth $\Delta\nu_G$ of ^{170}Er in setup 1 as a function of the EC temperature corresponding to the Doppler broadening of the line. The measured values do not fit to the ones expected from Eq. (1.23) for collimation at apertures 1 and 2 drawn with a solid red line. A free fit to $\Delta\nu_G = \alpha\sqrt{T_{EC}}$, indicated by the dashed blue line, suggest $\alpha = 10.0(3)$ corresponding to a collimation at aperture 2 and the octagon chamber.

a Voigt profile to the absorption data.

The linewidth of all isotopes should not differ more than 1 % since the mass dependence of Doppler broadening is weak. However, the linewidth of the three most abundant bosonic isotopes differs by 8 % what we explain by the influence of the fermionic ^{167}Er. ^{167}Er is split into eight hyperfine states and not resolved individually in the measurement, but nevertheless alters the absorption peaks of ^{166}Er and ^{168}Er. Therefore, in the following we will only focus on the properties of the ^{170}Er isotope, which shows the most isolated but yet distinct absorption peak.

The linewidth of a Doppler broadened line depends on the transversal velocity component of the atoms and is thus proportional to the beam divergence and the temperature. In Fig. 5.9 we show the measured values of the Gaussian contribution $\Delta\nu_G$ to the linewidth of the Voigt profile, corresponding to the Doppler width, as a function of T_{EC}, where $T_{HL} = T_{EC} + 100\,°C$. From Eq. (1.23), we expect

$$\Delta\nu_D = (\nu_0/c)\, f\, \sqrt{3\, k_B\, T\,/\, m} = \alpha\sqrt{T}\,, \tag{5.1}$$

where f is the collimation ratio and α a constant for a fixed f. For a collimation of the atomic beam at apertures 1 and 2, as illustrated in Fig. 5.3, $\alpha = 3.1$ and $\Delta\nu_G$ should follow the solid red line. The calculated values strongly differ

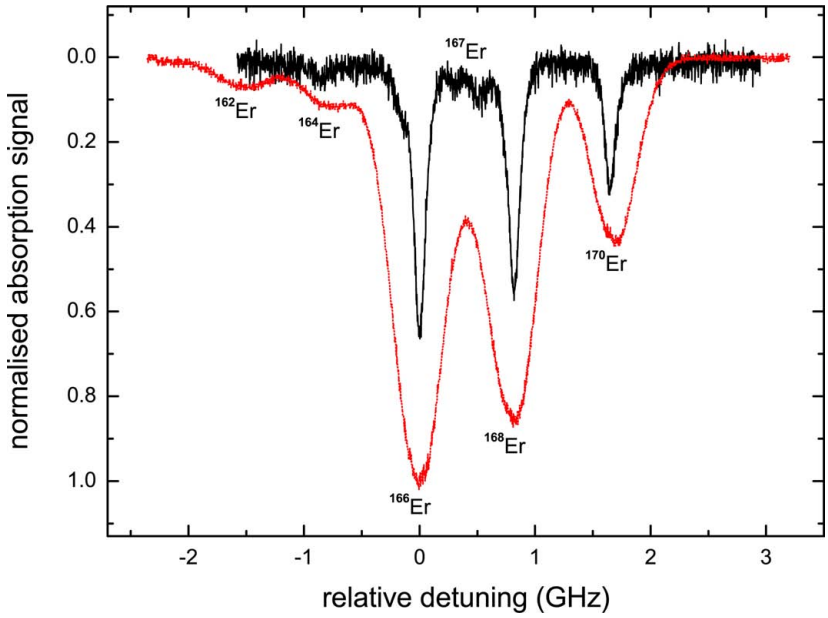

Figure 5.10: Spectrum in setup 1 for different HL temperatures. Dotted red line: $T_{\mathrm{EC}} = 1350\,°\mathrm{C}$, $T_{\mathrm{HL}} = 1450\,°\mathrm{C}$; solid black line: $T_{\mathrm{EC}} = 1350\,°\mathrm{C}$, $T_{\mathrm{HL}} = 970\,°\mathrm{C}$, signal magnified by a factor of 5. For low HL temperatures, the peaks get narrower and the signal is reduced. Therefore hyperfine states of ^{167}Er appear, whereas ^{162}Er is longer resolved. The signal is normalized to the maximum absorption of the signal indicated by the dotted red line corresponding to a maximum optical density $OD_{\mathrm{max}} \simeq 0.21$. For the solid black line, $OD_{\mathrm{max}} \simeq 0.07$.

from the measured ones, which always show larger values of the linewidth. This trend is consistent with our fluorescence measurements. The dashed blue line corresponds to a fit of the measured values by Eq. (5.1), suggesting $\alpha = 10.0(3)$. If we consider the first aperture is not playing any role and that the collimation is provided by aperture 2 and the inner edges of the octagon chamber, we expect $\alpha = 10.1$. This agrees well with the measured values and further confirms the fluorescence measurements.

Varying the HL temperature

To investigate the reason for the apparent failure of aperture 1, we decrease the HL temperature whilst maintaining constant EC temperature. Due to radiative heating the lowest attainable temperature is $T_{\mathrm{HL}} = 970\,°\mathrm{C}$ at $T_{\mathrm{EC}} = 1350\,°\mathrm{C}$. The corresponding spectrum is shown as a solid black curve in Fig. 5.10. The signal has lower intensity and is magnified by a factor of 5 to compare it to the spectrum at $T_{\mathrm{EC}} = 1350\,°\mathrm{C}, T_{\mathrm{HL}} = 1450\,°\mathrm{C}$, drawn as dotted red line. We see that the absorption peaks are narrowed by decreasing the HL temperature. Due to the narrower absorption spectra, hyperfine states of ^{167}Er appear for instance between the ^{166}Er and the ^{168}Er peak. This clear change of the signal strength

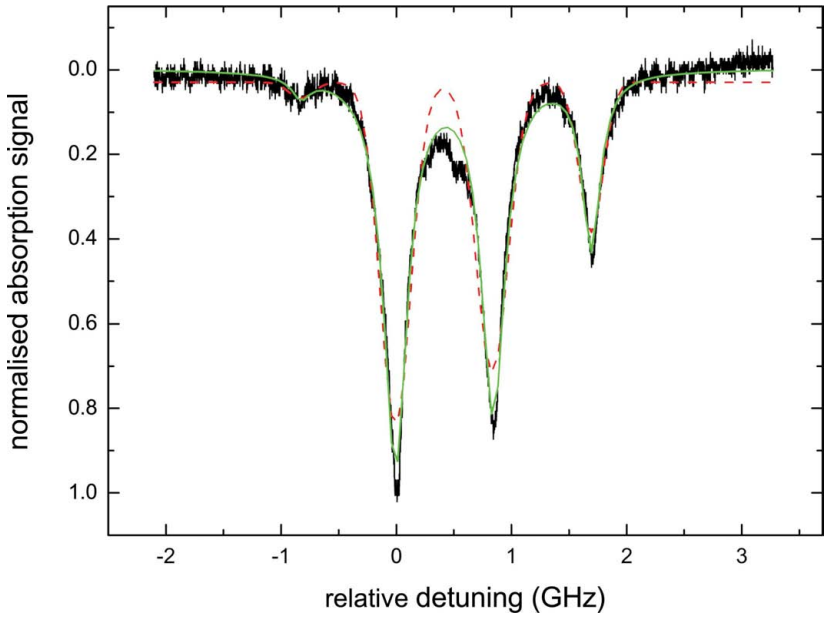

Figure 5.11: Change of the spectrum shape for $T_{\mathrm{EC}} < T_{\mathrm{HL}}$. The solid green line representing a fit to a pure Lorentzian function, fits the spectrum at $T_{\mathrm{EC}} = 1350\,^{\circ}\mathrm{C}$,$T_{\mathrm{HL}} = 1150\,^{\circ}\mathrm{C}$ better than the dashed red line representing a fit to a pure Gaussian function. The signal is normalized to the maximum absorption corresponding to a maximum optical density $OD_{\mathrm{max}} \simeq 0.09$.

and linewidth emphasizes that the HL temperature affects the atomic beam and that it does not only play the secondary role to avoid source material condensation at the apertures.

The line shape of the absorption peaks changes with decreasing the HL temperature while keeping the EC temperature constant, as visible in Fig. 5.11. This observation demonstrates that not only the EC, where the Er material is placed, but also the HL has an oven-like behavior. The solid green line representing a fit to a pure Lorentzian function, fits the spectrum at $T_{\mathrm{EC}} = 1350\,^{\circ}\mathrm{C}$, $T_{\mathrm{HL}} = 1150\,^{\circ}\mathrm{C}$ better than the dashed red line representing a fit to a pure Gaussian function. We find that in contrast to temperature sets with $T_{\mathrm{HL}} \gtrsim T_{\mathrm{EC}}$, where the spectrum evolves towards an almost pure Gaussian profile, for $T_{\mathrm{HL}} \lesssim T_{\mathrm{EC}}$ a Lorentzian function is the dominant contribution to the total line shape. According to Eq. (1.27), the Voigt profile has a Gaussian contribution $\Delta\nu_{\mathrm{G}}$ and a Lorentzian contribution $\Delta\nu_{\mathrm{L}}$ to the total width $\Delta\nu_{\mathrm{V}}$. For $T_{\mathrm{EC}} = 1350\,^{\circ}\mathrm{C}$, $T_{\mathrm{HL}} = 1450\,^{\circ}\mathrm{C}$, $(\Delta\nu_{\mathrm{G}} \,/\, \Delta\nu_{\mathrm{L}}) \approx 10^{21}$ and for $T_{\mathrm{EC}} = 1350\,^{\circ}\mathrm{C}$, $T_{\mathrm{HL}} = 1150\,^{\circ}\mathrm{C}$, $(\Delta\nu_{\mathrm{G}} \,/\, \Delta\nu_{\mathrm{L}}) \approx 0.6$, signifying the change of the line shape. This implies that for $T_{\mathrm{HL}} \lesssim T_{\mathrm{EC}}$ Doppler broadening is not the only broadening mechanism present. The underlying mechanism for the Lorentzian line shape is not fully understood and suggests that complicated atom dynamics occur in the HL part. Saturation- and collisional broadening have Lorentzian line shapes. The first mechanism can be neglected

due to the low intensity of the laser beam of $I \approx 0.01\, I_{\mathrm{sat}}$. As follows, collisional broadening can partially explain the observed behavior.

The HL part has EC-like character

We explain the strong influence of the HL temperature on the linewidth and the line shape as follows. Erbium atoms that emerge from the EC at too large solid angles will not pass aperture 2, but stick to the walls of the HL part. Since these walls are heated, the atoms are re-emitted in random directions. Re-emitted atoms collide with atoms emerging from the EC and create an atomic vapor in the HL. This disables the creation of an atomic beam and gives the HL part an EC-like character. From aperture 2, an atomic beam emerges into the octagon chamber, where it can propagate freely since no atoms are re-emitted from the walls. This corresponds to the situation illustrated in Fig. 5.5: both the EC and the HL part are filled with atomic vapor and thus aperture 1 and the EC itself are effectless to the atomic beam. Consequently aperture 2 and the HL inherit this role and the HL becomes EC-like character. This mechanism depends on two parameters: the flux from the EC, and the temperature of the HL. For low flux from the EC the collisions will be limited and the beam can propagate through the HL part. For low HL temperatures the re-emission of atoms from the walls is reduced and the emergence of atomic vapor in the HL is limited.

We check our speculation by measuring the linewidth as a function of the HL temperature for a constant EC temperature of 1250 °C, as shown in Fig. 5.12. The total linewidth $\Delta\nu_{\mathrm{V}}$ consists of a Gaussian contribution $\Delta\nu_{\mathrm{G}}$, shown as black squares, and Lorentzian contribution $\Delta\nu_{\mathrm{L}}$, shown as red circles. The HL temperature strongly determines the ratio of both contributions. For $T_{\mathrm{HL}} \geq 1200\,^{\circ}\mathrm{C}$, the profile is purely Gaussian and the Lorentzian contribution is not resolved. At high HL temperatures $\Delta\nu_{\mathrm{G}}$ is on the order of magnitude of the expected Doppler broadening for an atomic beam collimated at aperture 2 and the octagon chamber, indicated as a dotted line. For $T_{\mathrm{HL}} \leq 1150\,^{\circ}\mathrm{C}$, $\Delta\nu_{\mathrm{G}}$ drops and $\Delta\nu_{\mathrm{L}}$ dominates. In this region, $\Delta\nu_{\mathrm{G}}$ is even lower than the expected Doppler broadening for an atomic beam collimated at apertures 1 and 2, indicated as a dashed line. This confirms the considerations above: for low HL temperatures the beam can propagate freely from the EC through the HL part, and an additional broadening mechanism with Lorentzian line shape is resolved. $\Delta\nu_{\mathrm{L}}$ increases with rising HL temperature. In first order this agrees with Eq. (1.25), which describes the width of a line broadened by collisional broadening.

Conclusion

We conclude that in the original collimation setup for operation temperatures with $T_{\mathrm{HL}} \gtrsim T_{\mathrm{EC}}$, the emerging atomic beam is highly divergent as pointed out directly by the fluorescence imaging measurement as well as by the large linewidth

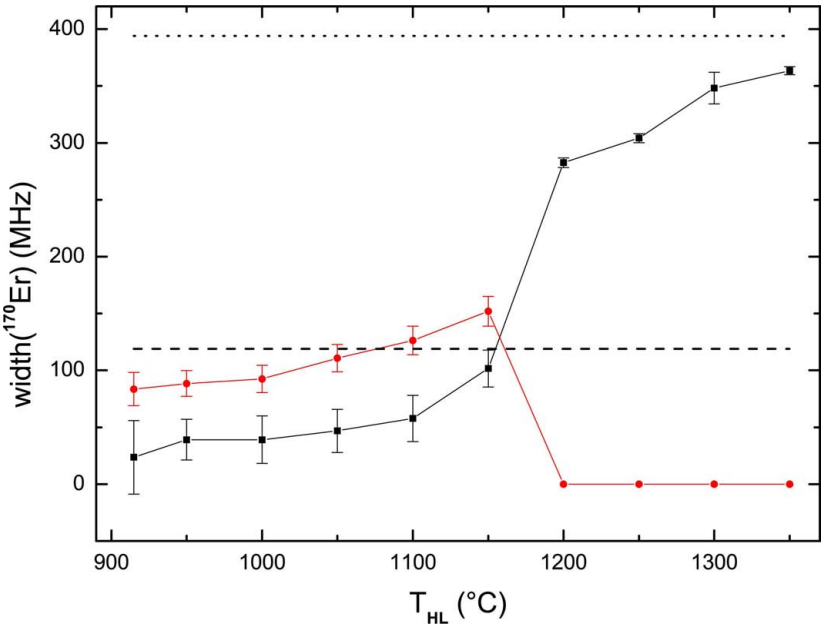

Figure 5.12: Gaussian contribution $\Delta\nu_G$, shown as black squares, and Lorentzian contribution $\Delta\nu_L$, shown as red circles, to the total linewidth $\Delta\nu_V$ of the ^{170}Er absorption peak as a function of the HL temperature for $T_{EC} = 1250\,°C$. For $T_{HL} \geq 1200\,°C$, the profile is purely Gaussian and the Lorentzian contribution is not resolved. For $T_{HL} \leq 1150\,°C$, $\Delta\nu_G$ drops and $\Delta\nu_L$ dominates. The horizontal lines correspond to the expected values of the Doppler broadening of an atomic beam at $T_{EC} = 1250\,°C$. Dashed line: collimation at apertures 1 and 2, dotted line: collimation at aperture 2 and the octagon chamber.

of the absorption peaks. This is explained by a collimation of the atomic beam at aperture 2 and the inner edges of the octagon. Consequently, the HL part is also filled with atomic vapor and has an EC like character. This results into a strong influence of the HL temperature on the line shape and the linewidth of the absorption peaks. For $T_{HL} \gtrsim T_{EC}$ Doppler broadening is the dominant broadening mechanism, leading to a broad, Gaussian shaped absorption peak. We assume that collisional broadening also contributes to the total broadening, as for $T_{HL} \lesssim T_{EC}$ the line shape changes to a Lorentzian function and as the temperature dependence of the linewidth cannot solely be explained by Doppler broadening.

At an oven operation with heated apertures, the high divergence of the atomic beam results in a strong contamination of the chamber with unused Er atoms. This exhausts the source material quickly, requiring frequent refilling of the oven and is thus not providing a good system for long-term operation. To operate the oven at low HL temperatures does also not provide a good long term performance. Although in this case, the reduced linewidth suggests a well collimated beam, on longer timescales, Er atoms condensing on the colder apertures would grow over

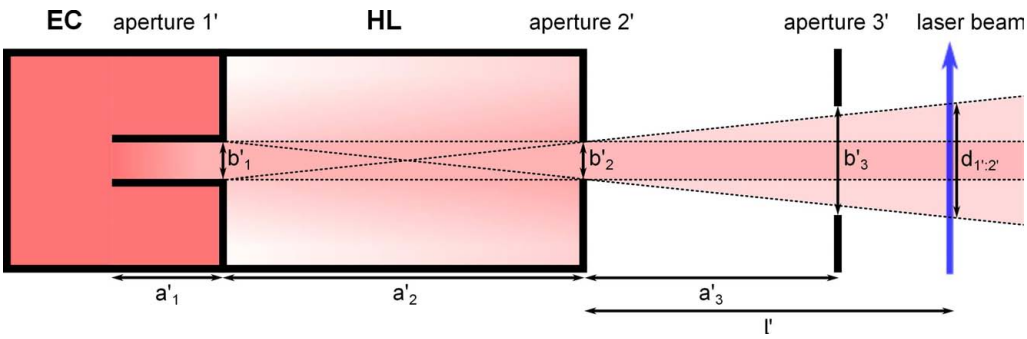

Figure 5.13: Scheme of the optimized collimation setup, referred to as setup 2. Aperture $1'$ is a tube aperture with length $a_1' \simeq 30\,\text{mm}$ and inner diameter $b_1' \simeq 3\,\text{mm}$. Aperture $2'$ and the additional aperture $3'$ have inner diameters of $b_2' \simeq 3\,\text{mm}$ and $b_3' \simeq 8\,\text{mm}$ and are spaced by $a_2' \simeq 50\,\text{mm}$ and $a_3' \simeq 65\,\text{mm}$. At a distance of $l' \simeq 106.5\,\text{mm}$ from aperture $2'$, the probe laser beam transversely intersects the atomic beam. For a collimation on apertures $1'$ and $2'$, the atomic beam diameter is $d_{1':2'} = 11\,\text{mm}$.

and block the atomic beam. Therefore, we designed a new-generation collimation setup.

5.3 Collimation setup 2

The optimized collimation setup, setup 2, is illustrated in Fig. 5.13. Aperture 1 is replaced by aperture $1'$, which is a tube aperture with a length of $a_1' \simeq 30\,\text{mm}$ and an inner diameter $b_1' \simeq 3\,\text{mm}$. According to Eq. (1.10), such a tube should reduce the total flux emerging from the EC by a factor of 0.27, leaving the longitudinal flux density almost equal. The second aperture, aperture $2'$, at a distance $a_2' \simeq 50\,\text{mm}$ from aperture $1'$ also has a reduced inner diameter $b_2' \simeq 3\,\text{mm}$, which guarantees a better collimation. Additionally, at a distance $a_3' \simeq 65\,\text{mm}$ from aperture $2'$, we insert a dark wall collimator, aperture $3'$, which in contrast to aperture $1'$ and $2'$ is not heated. It has inner diameter $b_3' \simeq 8\,\text{mm}$ and reduces the material accumulation in the octagon chamber. This setup will not eliminate the effusive-oven like behavior of the HL section but will reduce its influence on the atomic beam.

Although the geometry of the first aperture of 30 mm is larger than in setup 1, Eq. (1.3) is still fulfilled and so we assume that the EC section still operates in the effusive regime. We performed measurements similar to the ones described in the previous section. The 401 nm probe light intersects the atomic beam transversely at a distance of $l' \simeq 106.5\,\text{mm}$ from aperture $2'$. The measurements were performed on the completely mounted vacuum chamber.

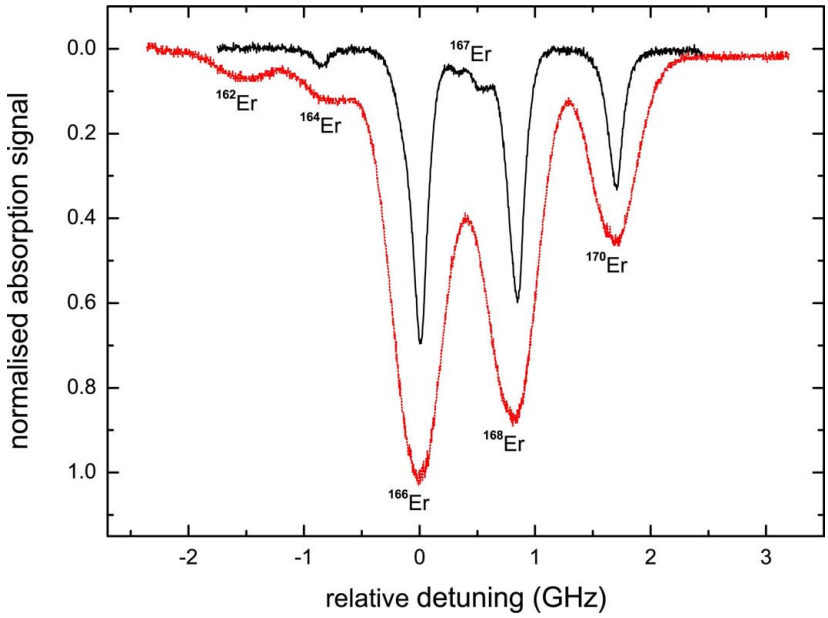

Figure 5.14: Spectrum of setup 1 (dotted red line) and of setup 2 (solid black line, magnified by a factor of 5), both at $T_{\mathrm{EC}} = 1350\,°\mathrm{C}$ and $T_{\mathrm{HL}} = 1450\,°\mathrm{C}$. In setup 2, the peaks are narrowed, and the intensity is reduced. Therefore hyperfine states of ^{167}Er appear, whereas ^{162}Er is no longer resolved. The signal is normalized to the maximum absorption of the signal indicated by the dotted red line corresponding to a maximum optical density $OD_{\mathrm{max}} \simeq 0.21$. For the solid black line, $OD_{\mathrm{max}} \simeq 0.07$.

Beam divergence

We first perform fluorescence imaging of the atomic beam. We observe a lower fluorescence signal due to the reduced atomic flux. As a consequence, we image with a long exposure time, much longer than the inverse of the laser scan rate. We evaluate the beam diameter from a single fluorescence image. We observe a smaller beam divergence compared to the one of setup 1. For instance, the fluorescent region is not anymore cut from the field of view as in setup 1. We evaluate the beam diameter to be $d_{\mathrm{ex}\prime} = 17(3)\,\mathrm{mm}$.

Compared to setup 1, in which $d_{\mathrm{ex}} \geq 41\,\mathrm{mm}$, the beam diameter is strongly reduced. But also in this setup, the measured value significantly deviates from the expected value corresponding to proper collimation at apertures $1'$ and $2'$ of $d_{1':2'} = 11\,\mathrm{mm}$. If we consider again, that the first aperture does not play a role and that the beam is collimated at apertures $2'$ and $3'$, we expect a diameter of $d_{2':3'} = 15\,\mathrm{mm}$, which is in better agreement with the measurement. This corresponds to a situation similar to the simplified scheme for setup 1 in Fig. 5.5, except that the aperture setup is different.

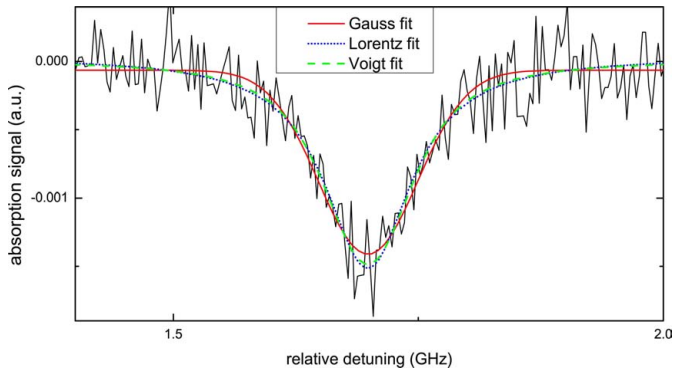

(a)

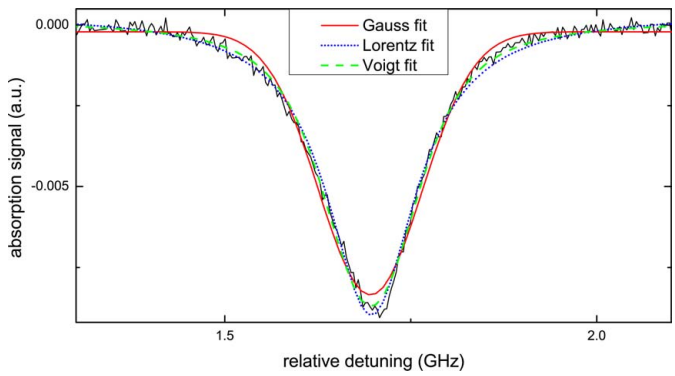

(b)

Figure 5.15: Absorption peak of ^{170}Er fitted to different functions: Gaussian function (solid red line), Lorentzian function (dotted blue line) and Voigt profile (dashed green line) at (a) $T_{\mathrm{EC}} = 1200\,^{\circ}\mathrm{C}$ and (b) $T_{\mathrm{EC}} = 1350\,^{\circ}\mathrm{C}$. The Voigt profile fit gives for (a) $\Delta\nu_{\mathrm{G}} = 5(3) \times 10^2\,\mathrm{MHz}$ and $\Delta\nu_{\mathrm{L}} = 9(2) \times 10^2\,\mathrm{MHz}$ and for (b) $\Delta\nu_{\mathrm{G}} = 101(4)\,\mathrm{MHz}$ and $\Delta\nu_{\mathrm{L}} = 84(4)\,\mathrm{MHz}$. The Gaussian and the Lorentian fit give for (a) $\Delta\nu_{\mathrm{G}} = 119(5)\,\mathrm{MHz}$ and $\Delta\nu_{\mathrm{L}} = 108(7)\,\mathrm{MHz}$ and for (b) $\Delta\nu_{\mathrm{G}} = 164(1)\,\mathrm{MHz}$ and $\Delta\nu_{\mathrm{L}} = 141(2)\,\mathrm{MHz}$.

Spectrum

In collimation setup 2, the spectrum shows narrowed absorption peaks and has lower intensity. In Fig. 5.14 we compare the absorption spectrum obtained using setup 1 (dotted red line) and setup 2 (solid black line). Both spectra are observed at $T_{\mathrm{EC}} = 1350\,^{\circ}\mathrm{C}$ and $T_{\mathrm{HL}} = 1450\,^{\circ}\mathrm{C}$. The spectrum of setup 2 is magnified by a factor of 5 and resolves hyperfine states of ^{167}Er, whereas ^{162}Er is no longer visible because of its very low abundance.

Line shape and linewidth

In contrast to setup 1, where we find the spectrum to be described by a pure Gaussian function for most temperature sets, for setup 2 we observe almost equal contributions from both a Lorentzian as well as a Gaussian function to

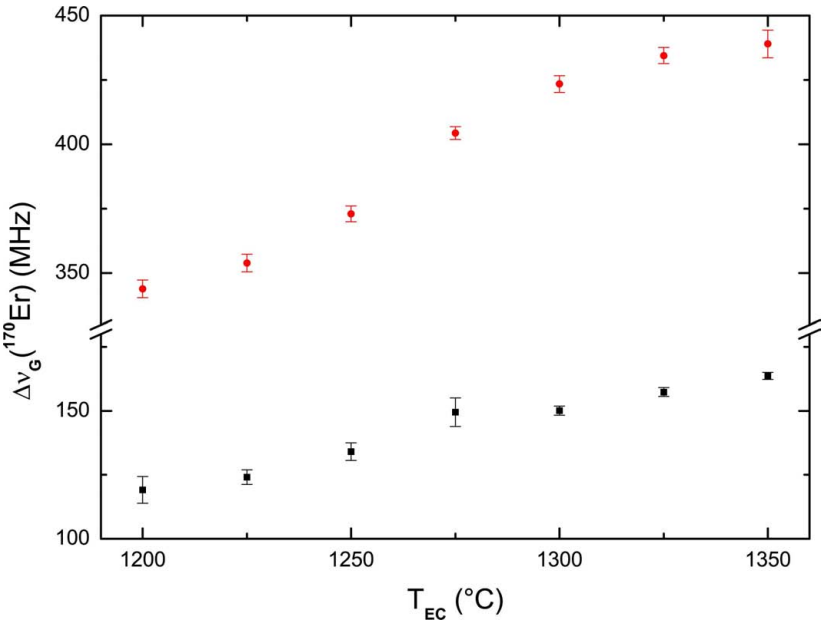

Figure 5.16: Gaussian linewidth $\Delta\nu_G$ as a function of the EC temperature for setup 1, indicated by red circles, and for setup 2, indicated by black squares. The linewidth in setup 2 is reduced by a factor of 3 compared to setup 1, which also corresponds to the value expected by Eq. (1.23). The temperature dependence of $\Delta\nu_G$ is reduced in setup 2.

the Voigt profile of the absorption peaks for all temperature sets. Figure 5.15 (a) and (b) shows the absorption peak of ^{170}Er for low ($T_{EC} = 1200\,°C$) and for high ($T_{EC} = 1350\,°C$) EC temperatures. We evaluate the peak profile using different fit functions. The solid red line represents a Gaussian function, the dotted blue line a Lorentzian function and the dashed green line a Voigt profile. For both low and high temperatures, we observe that all these functions give a good description of the observed profile. For lower EC temperatures, a fit of the Voigt profile to the data gives the Gaussian and Lorentzian width with an uncertainty of 50 %, indicating that due to the low signal-to-noise ratio the fit cannot discriminate between the two contributions. At high EC temperatures, we can distinguish the Gaussian and Lorentzian contributions, which have almost the same weight. For convenience and to have a direct comparison with setup 1, we choose to fit all the absorption spectra with a pure Gaussian function. The extracted values represent an upper limit to the Gaussian width and overestimate thus the Doppler broadening, since the Lorentzian contribution is neglected. However, these values can give us a qualitative trend on the temperature dependence. The error bars shown in all following graphs refer to the statistical error from the fit of a Gaussian function to the absorption data.

Our results are summarized in Fig. 5.16. We compare the Gaussian linewidth $\Delta\nu_G$ as a function of the EC temperature for setup 1, indicated by red circles, with

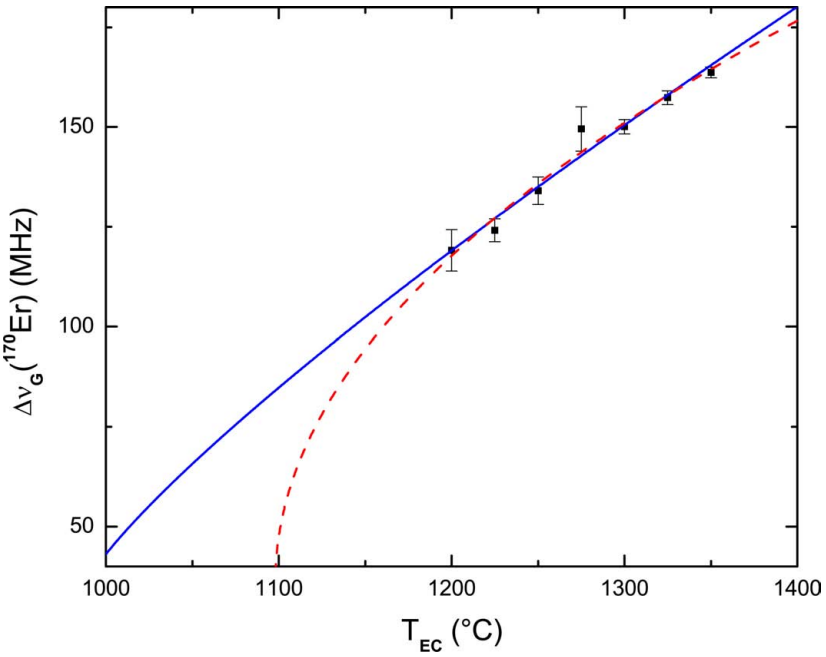

Figure 5.17: Different fits to $\Delta\nu_{\mathrm{G}}(T_{\mathrm{EC}})$ in setup 2 (c.f. Fig. 5.16) by $\Delta\nu_{\mathrm{G}} = \alpha\,(T_{\mathrm{EC}})^x$. For fixed $x = 0.5$ corresponding to pure Doppler broadening, we find $\alpha = 8.1$ (dashed red line). For fixed $\alpha = 1.0$ corresponding to collimation at apertures $1'$ and $2'$, we find $x = 0.8$ (solid blue line).

setup 2, indicated by black squares, where $T_{\mathrm{HL}} = T_{\mathrm{EC}} + 100\,°\mathrm{C}$. The linewidth in setup 2 is reduced by a factor of 3 compared to setup 1, which also corresponds to the value expected by Eq. (1.23) if we consider a purely Doppler broadened line.

The linewidth is affected by both the effective collimation and the type of broadening mechanism. If we consider a pure Doppler broadening and fit the data corresponding to the black squares in Fig. 5.16 to Eq. 5.1, as shown by the dashed red line in Fig.5.17, we find $\alpha = 8.1$. This suggests an atomic beam that is much less collimated than by apertures $2'$ and $3'$. If we consider a collimation of the atomic beam at apertures $1'$ and $2'$ corresponding to $\alpha = 1.0$ and fit the data to a function T^x, as shown by the solid blue line in Fig. 5.17, we find a temperature dependence of $T^{0.8}$. Our data suggests that we are in an intermediate case. Further experiments at lower temperatures could clarify this point.

In general, we observe that Doppler broadening is not the sole broadening mechanism contributing to the absorption line suggesting complicated atom dynamics inside the HL part. From the linewidth at $T_{\mathrm{EC}} = 1350\,°\mathrm{C}$ we estimate an upper limit of the transversal Doppler velocity to $65\,\mathrm{m/s}$.

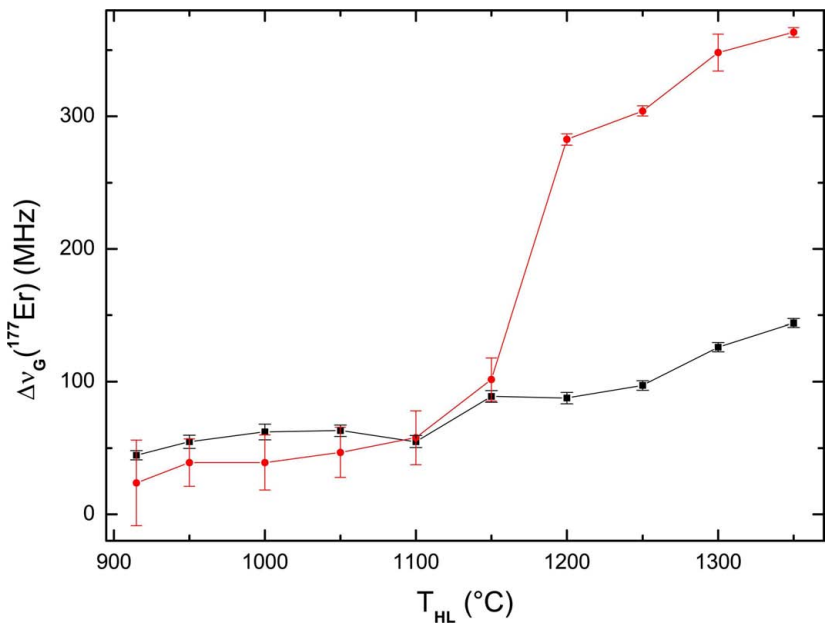

Figure 5.18: Gaussian linewidth $\Delta\nu_G$ as a function of the HL temperature, where $T_{EC} = 1250\,°C$ for setup 1, indicated by red circles, and for setup 2, indicated by black squares. While for $T_{HL} \lesssim 1150\,°C$, the width is for both setups of the same magnitude, for $T_{HL} > 1150\,°C$ the influence of the HL temperature on $\Delta\nu_G$ is strongly reduced in setup 2.

The influence of the HL temperature

In Fig. 5.18 we show the Gaussian linewidth $\Delta\nu_G$ as a function of the HL temperature, where $T_{EC} = 1250\,°C$ for setup 1, indicated by red circles, and for setup 2, indicated by black squares. The influence of the HL temperature on $\Delta\nu_G$ is reduced by setup 2. While for $T_{HL} \lesssim 1150\,°C$, the width is for both setups of the same magnitude, for $T_{HL} > 1150\,°C$ the influence of the HL temperature on $\Delta\nu_G$ is strongly reduced in setup 2. We conclude that the emergence of atomic vapor in the HL is hindered in setup 2. This agrees well with the picture drawn above of the EC-like character of the HL, which is dependent on T_{HL} and on the flux from the EC. Compared to setup 1, in setup 2 the flux is reduced and so are the collisions in the HL part. Therefore, the influence of the HL temperature on $\Delta\nu_G$ is reduced.

Conclusion

Similar to setup 1, for oven operation with $T_{HL} > T_{EC}$ in setup 2, the HL has EC-like character and is filled with atomic vapor disabling aperture $1'$. But although the atomic beam is not collimated as intended, this optimized setup shows good improvements. The atomic beam divergence is reduced and so is the part of the unused atoms. Also the influence of the HL temperature on the atomic beam is

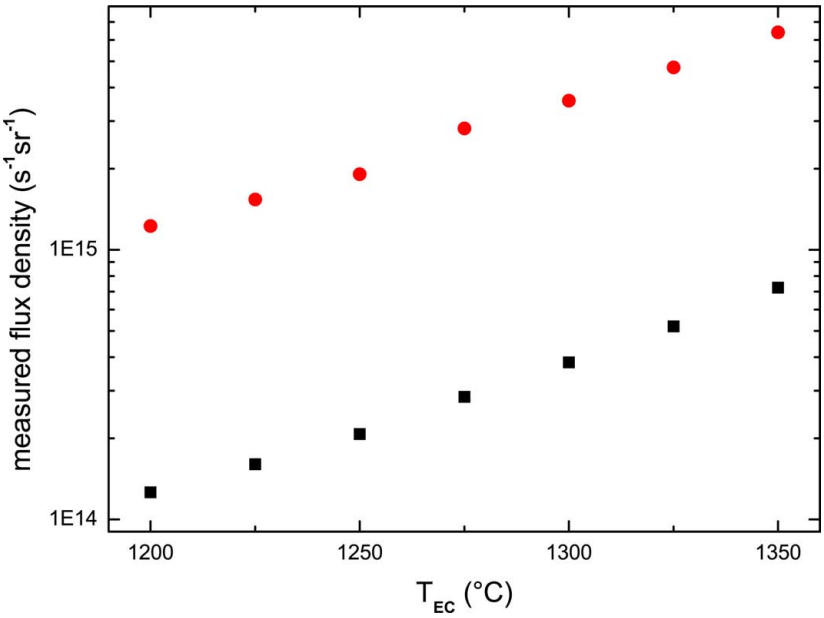

Figure 5.19: The flux density in units of sr^{-1} measured in the octagon chamber as a function of the EC temperature, where $T_{\mathrm{HL}} = T_{\mathrm{EC}} + 100\,°\mathrm{C}$. The flux in setup 1, indicated by red circles, is an order of magnitude higher than in setup 2, indicated as black squares. The linear temperature dependence of the flux in both setups exhibits the exponential dependence of the vapor pressure on the temperature.

strongly reduced. Due to equally strong Gaussian and Lorentzian contributions to the line shape, we assume that besides Doppler broadening also collisional broadening contributes to the total broadening.

5.4 Flux

The atomic flux is a very important quantity to characterize the oven system since it determines the number of atoms per unit time that enter the ZS tube and that can be captured by the MOT. According to Sec. 1.3, we can estimate the flux at the position of the probe laser beam by measuring I, I_0 and j. From the ^{166}Er absorption peak amplitude of the differential signal and the magnitude of the reference signal, we obtain the transmitted intensity I and the incident intensity I_0. By imaging the fluorescence on resonance of the ^{166}Er transition, we measure the light-atom interaction length j. We normalise the total flux obtained from Eq. (1.17) to the unit solid angle of emergence, and account for the fact that we measured the optical density only for ^{166}Er by scaling it with the inverse abundance of ^{166}Er. The resulting flux density $\Theta_{\mathrm{ex}}\,/\,\mathrm{sr}$ includes all isotopes and holds only for small solid angles. It provides a suitable quantity to analyse the flux measured in the octagon chamber in dependence of the collimation setup and of the operation temperature.

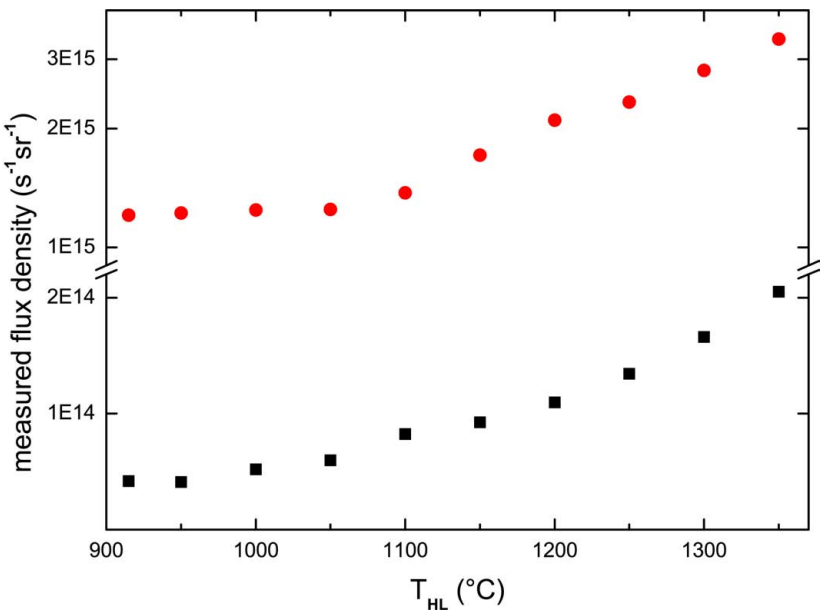

Figure 5.20: The flux density in units of sr^{-1} measured in the octagon chamber as a function of the HL temperature, where $T_{\mathrm{EC}} = 1250\,°\mathrm{C}$. Both in setup 1, indicated by red circles, and in setup 2, indicated by black squares, the flux is dependent on the HL temperature for $T_{\mathrm{HL}} \gtrsim 1050\,°\mathrm{C}$.

Setup 1 vs. setup 2

Figure 5.19 shows the flux density $\Theta_{\mathrm{ex}}\,/\,\mathrm{sr}$ measured in the octagon chamber as a function of the EC temperature on a logarithmic scale, where $T_{\mathrm{HL}} = T_{\mathrm{EC}} + 100\,°\mathrm{C}$. The flux in setup 2, indicated as black squares, is reduced to 9 % of the flux of setup 1, indicated as red circles. This agrees well with the flux reduction due to the different collimation setup expected from Eq. (1.9), which also predicts a value of 9 %. In both setups we see a linear temperature dependence with equal slope, which reflects the exponential temperature dependence of the vapor pressure shown in Eq. (2.1), which is proportional to the atomic flux [51].

Influence of the HL temperature

As expected, the HL temperature influences the flux in both setups. We show in Fig. 5.20 the flux density $\Theta_{\mathrm{ex}}\,/\,\mathrm{sr}$ measured in the octagon chamber as a function of the HL temperature. The EC temperature is constant at $T_{\mathrm{EC}} = 1250\,°\mathrm{C}$. Both in setup 1, indicated by red circles, and in setup 2, indicated by black squares, the flux depends on the HL temperature for $T_{\mathrm{HL}} \gtrsim 1050\,°\mathrm{C}$. In this region, the increase of the flux with the HL temperature is of similar strength in both setups. In contrast to this, as show in previous measurements (c.f. Fig. 5.18), the linewidth $\Delta\nu$ in setup 2 shows reduced dependence on the HL temperature. Therefore, we conclude that in both setups for increasing HL temperatures, more

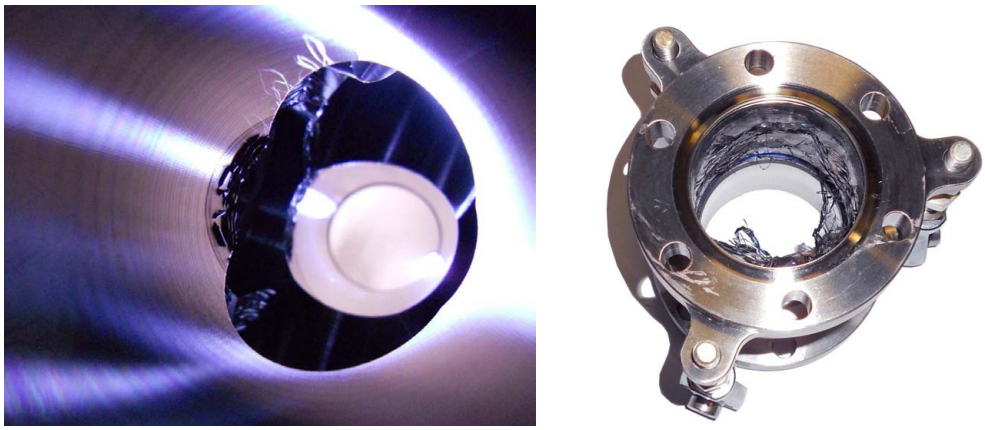

(a) (b)

Figure 5.21: Accumulation of Er in the vacuum chamber. (a) View through a viewport of the octagon while operating the oven in setup 1. On the inner edges, Er starts to accumulate in tiny rolls. (b) The connection tube of oven and octagon after operating the oven in setup 1. The inner walls are all over coated with Er, and the Er layer peels off.

and more atoms are re-emitted by the HL walls and contribute to the flux out of the oven. However, in setup 2, the total amount of re-emitted atoms is less and so are the collisions in the HL part. This explains that the HL temperature has reduced influence on the linewidth in setup 2, but that the relative increase of the flux with the HL temperature is similar in both setups.

Material deposition

The high flux in setup 1 also leads to undesirable accumulation of Er material. Already after some hours of oven operation, tiny rolls of accumulated Er emerged at the inner edges of the octagon, as show by Fig. 5.21 (a). When changing the apertures from setup 1 to setup 2, we opened the oven chamber and realized that Er material coated the inner walls of the connection tube of oven and octagon all over, as seen in Fig. 5.21 (b). Due to gravity, the Er layer peeled off the wall. In long-term operation, this would give additional contact surface for Er atoms from the beam that stick to it, grow new structures and finally block the atomic beam emerging from the oven. Thus, it was an important step to adapt the apertures to setup 2, since this setup provides a better collimated beam with reduced flux in contrast to setup 1, which could neither provide reliable long-term operation nor a well-collimated atomic beam.

Extracted flux at the MOT position

To estimate the number of atoms that reach the MOT region per second from our measured value for the atomic flux in the octagon chamber, we need to take into

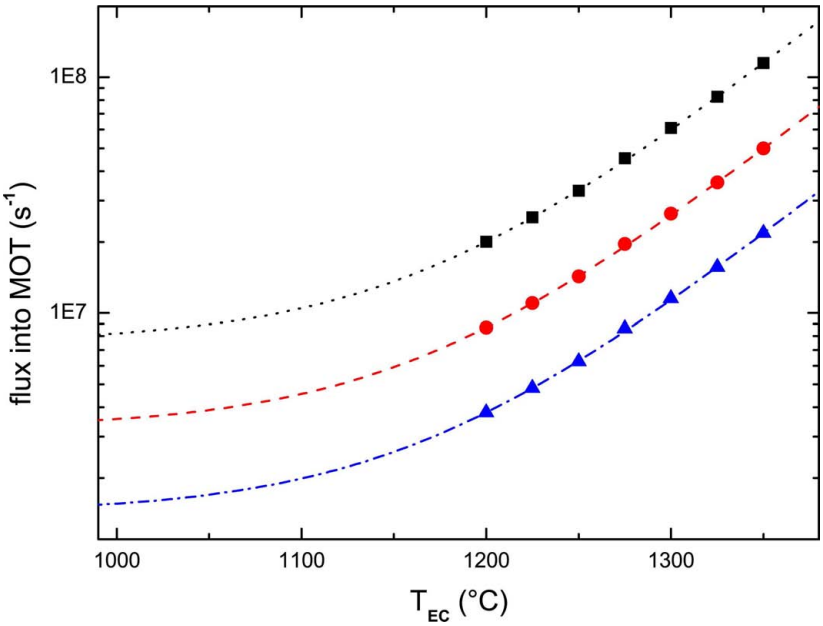

Figure 5.22: Derived atomic flux that can be captured by the MOT as a function of the EC temperature in setup 2. According to Eq. (5.2), several loss factors determine Θ_{MOT}, where in our setup ξ_2 is variable. We plot $\Theta_{\mathrm{MOT}}(T_{\mathrm{EC}})$ for three different values of ξ_2: 0.324 (black squares), 0.140 (red circles) and 0.061 (blue triangles). The dotted black, dashed red and dash-dotted blue lines correspond to exponential fits to the measured values and are also shown for lower temperatures to indicate the trend.

account several loss factors [84]. For geometrical arguments, only a fraction of Θ_{ex} can enter the ZS tube, what gives rise to a loss factor ξ_0. The isotope factor ξ_1 considers that only a certain isotope is slowed and captured. The ZS factor ξ_2 corresponds to the ratio of atoms that can be slowed by the ZS to the total number of atoms injected into the ZS: $\xi_2 = \int_0^{v_0} P'(v)\mathrm{d}v \,/\, \int_0^{\infty} P'(v)\mathrm{d}v$, where v_0 is the capture velocity of the ZS and $P'(v)$ is the velocity distribution in the beam. Since we can vary v_0 by the magnetic offset field of the ZS to adjust the magnetic field profile to the available slowing light power, also ξ_2 varies. The last loss factor ξ_3 accounts for that the slowed atomic beam leaving the ZS has a large divergence, since only longitudinal velocity components are slowed in the ZS. Therefore only a part of those atoms passes the MOT region: $\xi_3 = \int_0^{r_0} I(r)\mathrm{d}r \,/\, \int_0^{\infty} I(r)\mathrm{d}r$, where $I(r)$ is the intensity and r_0 is the radius of the MOT region. Combining this, yields to the number of atoms that can be captured in the MOT per unit time, if we assume that the capture velocity of the MOT is larger or equal to the final velocity of the slowed atoms from the ZS:

$$\Theta_{\mathrm{MOT}} \approx \xi_0\, \xi_1\, \xi_2\, \xi_3\, \Theta_{\mathrm{ex}}. \tag{5.2}$$

For our setup, $\xi_0 = 1.3 \times 10^{-4}$, ξ_2 can vary from 0.061 to 0.324, depending on the capture velocity and $\xi_3 = 0.011$. If we consider ^{166}Er, $\xi_1 = 0.336$. In Fig. 5.22

we plot $\Theta_{\mathrm{MOT}}(T_{\mathrm{EC}})$ for three different values of ξ_2: 0.324 (black squares), 0.140 (red circles) and 0.061 (blue triangles). The dotted black, dashed red and dash-dotted blue line correspond to exponential fits to the measured values and are also shown for lower temperatures, at which we could not probe the flux with our measurement. These lines indicate the presumable development of Θ_{MOT}, which should only be considered as a rough estimation. All values suggest that with setup 2, we can have a sufficient supply of Er atoms for tapping and further cooling large atomic samples.

Conclusion and Outlook

During my master thesis work, I focused my efforts in producing and characterizing an Er atomic beam, emerging from a high-temperature oven. The knowledge of the atomic beam behavior is fundamental for all future experiments on laser cooling and Bose condensation of Er atoms. Due to erbium's high melting point, the operation temperatures of the oven are unusually high for standard ultracold gas experiments based on alkali and alkaline earth elements. A big experimental effort was then necessary to design and operate the oven system. To shield the high temperatures, the oven system is water cooled. To avoid material condensation on colder parts of the system, the apertures that collimate the atomic beam are heated to higher temperatures than the effusion cell. To backup the system against power failure we protect it with an UPS. To secure safe operation, the oven system is connected to the cooling water system control and to the emergency-off system. The oven control program provides not only the user interface, but also coordinates the safety systems.

We characterize the atomic beam emerging from the oven by laser spectroscopy. Our measurements clearly reveal a complex beam behavior in the oven chamber leading to a highly divergent atomic beam and the deposition of Er material at the walls of the vacuum chamber. To minimize both effects, we had to design and mount a novel atomic beam collimation setup. The optimized setup consists of a tube aperture combined with two circular apertures. The measurements on this new setup show that it provides a much better collimation of the atomic beam with a reduced but sufficient atomic flux for large cooled and trapped ensembles of Er atoms. We find the optimal operation temperature to be 1250 °C. At this temperature, the estimated total atomic flux, which is injected into the ZS slower tube is $3 \times 10^{10}\,\mathrm{s}^{-1}$ with a transversal Doppler velocity of $65\,\mathrm{m/s}$. We expect correspondingly a number of the order of $10^{7}\,\mathrm{atoms/s}$ that can be captured by the MOT. This is a large enough value to guarantee a good MOT operation.

Currently, we are baking the complete experimental apparatus at a temperature of 200 °C to lower the background pressure in the chamber further. In the MOT chamber, we measure a background pressure of 2×10^{-11} mbar, which

(a)

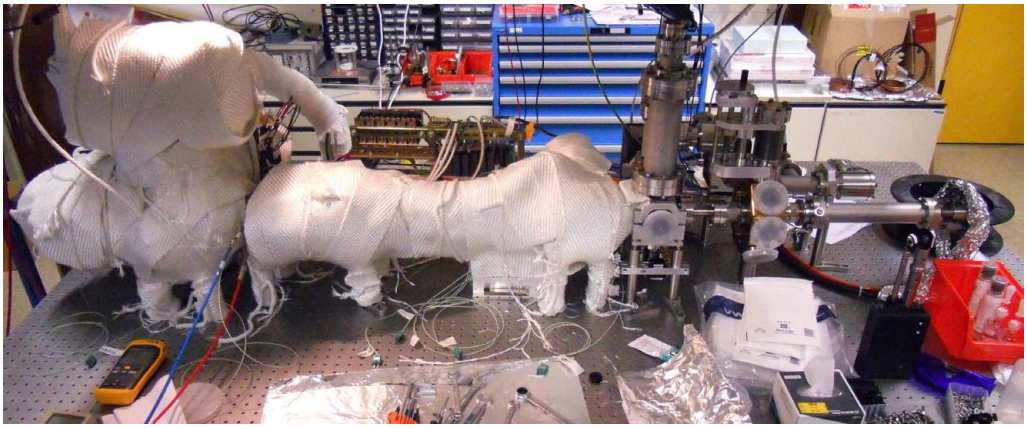

(b)

Figure 6.1: The vacuum chamber, (a) almost completely mounted. The ZS is clearly visible in the center in white, to the left hand side is the golden colored MOT chamber, and to the very right side is the Er oven. (b) The experimental chamber whilst the baking. To lower the background pressure, we heat the chamber to temperatures of 200 °C for several days. Thereby, residual gases that are enclosed in the stainless steel walls of the chamber and that limit the vacuum are released and pumped off.

assures a good enough vacuum level for our purposes. The next step is the adjustment and testing of the ZS as well as the setup of the narrow-line MOT. Once the MOT is working, we can load the ODT and start to study the collisional behavior of cold Er atoms in detail by Feshbach spectroscopy, which is a major step on our way to the Bose-Einstein condensation of Er.

Appendices

Appendix A

Magnetic moments of the lanthanides

The magnetic moment μ is calculated as

$$\mu = g\, M_J\, \mu_{\mathrm{B}}, \tag{A.1}$$

where M_J is the projection of the total angular momentum quantum number J towards its quantization axis. g is the Landé g-factor, which for LS-coupling of the electrons can be estimated as

$$g = 1 + (g_{\mathrm{s}} - 1)\, \frac{J\,(J-1) - L\,(L-1) + S\,(S-1)}{2\,J\,(J-1)}, \tag{A.2}$$

where g_{s} is the Landé g-factor of the electron, which is can be approximated by $g_{\mathrm{s}} = 2$. S is the total spin quantum number and L is the total orbital angular momentum quantum number. So, to evaluate the magnetic moment for a certain electronic configuration one has to know the specific quantum numbers S, L and J of the state. These quantities can be derived with the aid of Hund's rules [60]. Those rules only apply to the lowest term of the ground state configuration for cases where there is only one incomplete subshell and where the electrons couple in a LS-coupling scheme. This is the case for most of the lanthanide atoms in the ground state, as one can see in Tab. A.1. Except for Ce and Gd, the four Hund's rules determine S, L and J.

The calculated μ agrees well agreement with the measured values from [59] as shown in Tab. A.1. This underlines the validity of the assumptions and the explanation of the magnitude of the magnetic moments by the occupation of the $4f$ shell.

el.	$4f^n$	$5d^n$	S	L	J	term	g (lit.)	g (calc.)	μ (lit.)	μ (calc.)
La	0	1	$\frac{1}{2}$	2	$\frac{3}{2}$	${}^2D_{\frac{3}{2}}$	0.79755	0.80000	1.20	1.20
Ce	1	1	0	4	4	${}^1G_4$	0.94543	1.00000	3.78	4.00
Pr	3	0	$\frac{3}{2}$	6	$\frac{9}{2}$	${}^4I_{\frac{9}{2}}$	0.73104	0.72727	3.29	3.27
Nd	4	0	2	6	4	${}^5I_4$	0.60329	0.60000	2.41	2.40
Pm	5	0	$\frac{5}{2}$	5	$\frac{5}{2}$	${}^6H_{\frac{5}{2}}$	0.30500	0.28571	0.76	0.71
Sa	6	0	3	3	0	${}^7F_0$	0	0	0	0
Eu	7	0	$\frac{7}{2}$	0	$\frac{7}{2}$	${}^8S_{\frac{7}{2}}$	1.99340	2.00000	6.98	7.00
Gd	7	1	4	2	2	${}^9D_2$	2.65140	2.66667	5.30	5.33
Tb	9	0	$\frac{5}{2}$	5	$\frac{15}{2}$	${}^6H_{\frac{15}{2}}$	1.32513	1.33333	9.94	10.00
Dy	10	0	2	6	8	${}^5I_8$	1.24159	1.25000	9.93	10.00
Ho	11	0	$\frac{3}{2}$	6	$\frac{15}{2}$	${}^4I_{\frac{15}{2}}$	1.19514	1.20000	8.96	9.00
Er	12	0	1	5	6	${}^3H_6$	1.16381	1.16667	6.98	7.00
Tm	13	0	$\frac{1}{2}$	3	$\frac{7}{2}$	${}^2F_{\frac{7}{2}}$	1.14119	1.14286	3.99	4.00
Yb	14	0	0	0	0	${}^1S_0$	0	0	0	0

Table A.1: Occupation of the $4f$ shell, occupation of the $5d$ shell, resulting total spin quantum number S, resulting total orbital momentum quantum number L, resulting total angular momentum quantum number J, the according term symbol, the Landé g-factor found in literature [59], the estimated Landé g-factor calculated for LS-coupling, the resulting magnetic moment μ for the Landé g-factor from literature and from the calculation, for all ground states of the lanthanide elements ('el.').

Appendix B

Erbium oven control

The screenshot of the LabVIEW block diagram in Fig. B.1 shows the structure of the oven control program code. After initialization in a flat sequence, the main program starts. Here, the datasockets in the upper left manage the 'On/Stby' switch and access the network variables, which connect the control program with the PID controllers via the iTools *OPC server*. The while-loop on the upper right, plots the EC and the HL temperature and the working setpoints versus the absolute time. The environment variables in the right of the lower while loop acquire the UPS status. The MGE UPS *personal solution pack* program triggers the command line if one of the UPS variables changes. The command line has the new variable values as argument and starts the executable subVI *UPS-trigger-LabVIEW.exe*. The subVI reads the command line argument and distributes the contained information to the according environment variable. The oven control program displays the UPS status and sets the oven to standby mode for too little remaining backup time of the UPS, this is realized in the attached case structure.

The central part of the VI is the case structure in the lower while-loop. The screenshot only displays one out of 14 cases, which manage and secure the working of the control program:

- case 0: default case
- case 1: reacts to the 'EMERGENCY OFF' button[1]
- case 2-9: set safety limits for the input values of the OPC server variables and manages the 'On/Stby' switch
- case 10: preset values changeable via the 'enable changes' switch
- case 11-13: aid the scaling and appearance of the temperature plot

[1] As seen in Fig B.1, in an emergency case, the temperature ramps are set to $0\,^{\circ}\mathrm{C}/\mathrm{min}$. However, due to the interpretation of the PID controller, this sets the temperature immediately to the new setpoints of $0\,^{\circ}\mathrm{C}$.

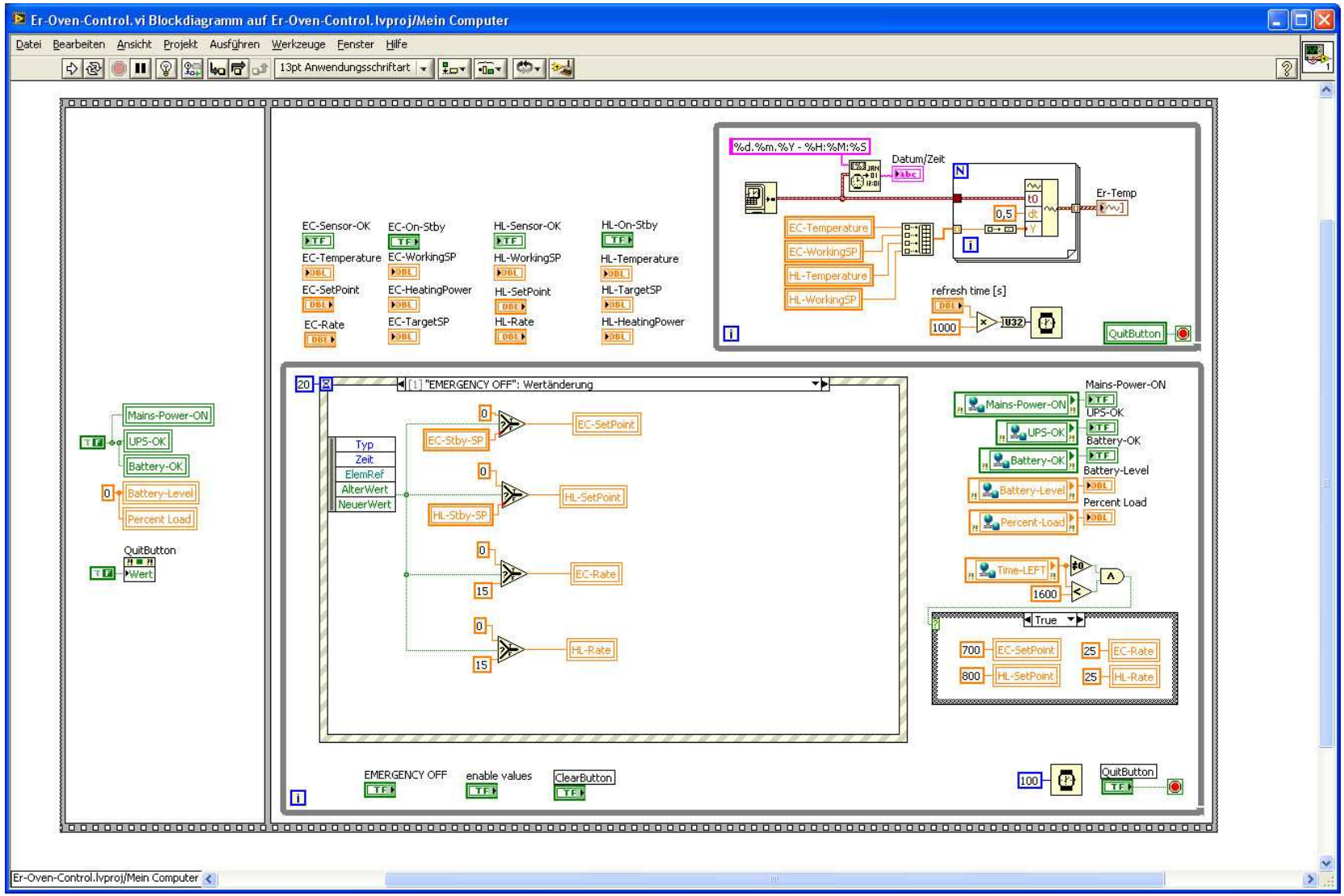

Figure B.1: A screenshot of the LabVIEW block diagram, which displays the oven control program code.

Appendix C

Atomic beam shutter control

C.1 Control box

We use an Atmel *AVR ATmega128* μC mounted on a *Crumb128-light* μC module. An external resonator with a frequency of 14.7456 MHz is the clock source for the processor. The detailed pin configuration and the whole electric circuit are shown in the circuit diagram in Fig. C.1. The settings to program the μC via the Atmel *AVR Studio 4* program with the *AVRISP mkII* programming interface are: ISP frequency 2 MHz, Fuses: (no M103C; SUT CKSEL = ext. crystal/resonator high freq., start-up time: 16 K CK +64 ms). We repeat a part of the manual text, which gives the main operating guidelines:

"The control box has on its face the following switches and connectors: power, emergency stop, ttl, power switch, reset push button (red), pc/manual control switch and the unshut/shut switch. On the side the servo can be plugged in, as well as, if necessary the programming interface. To access the potentiometers and the pushbutton (green), one has to open the box.

When everything is connected, the power switch starts the controller (no more than 8 V), the orange LED shines. All three other LEDs shine for 1 second (default led test at initialisation) (also if system is reset). The red push button resets the controller in case this is needed.

For control via the pc (TTL signal), set the pc/manual control switch to pc. The blue LED shines as well as either the green or the red one, indicating the status of the shutter (beam unshut or beam shut respectively).

For control by hand, set the pc/manual control switch to manual. The blue LED doesn't shine. The unshut/shut switch allows control over the shutter position, which is indicated by the green or the red LED.

For positioning the shutter positions, one has to operate in the manual control mode, has to keep the green push button pushed and turn at the same time

the screw at the according potentiometer. According means that you can only change the position of the choice you have made at the unshut/shut switch. The potentiometer marked 'u' will change the position of the shutter at unshut, if the unshut/shut switch is set to unshut. The potentiometer marked 's' will change the position of the shutter at shut, if the unshut/shut switch is set to shut. If the green push button is released, normal manual operation continues.

If an emergency stop occurs, the shutter will be set to 'beam shut' and block the atomic beam. The red, blue and green LED blink to indicate the interrupt. If the emergency stop ends, normal operation mode continues automatically.''

C.2 Source code

The explanation below, describes the source code shown in List.B.2, and is also contained in the control box manual.

''The header file, abs.h (see List. C.2), defines constants, macros and variables and links functions. In the program, after the including the needed header and libraries (order is not commutative) the main loop starts. The initialisation of input/output, interrupts, PWM and analog-to-digital conversion take place and interrupts are activated.

The while-loop keeps the program running and checks switches and the emergency stop. If this is not activated, the main loop checks whether the operation mode is manual control or pc control. In the fist case there's distinction between normal operation and positioning of the shutter via the potentiometers (setting the values for 'beam shut' and 'beam unshut'). If the emergency stop is active (signal at BNC connection is low, signal at μC is high (opto-isolator)), the shutter is set to the position 'beam shut' , and all LEDs are blinking.

The controlling of the servo is accomplished by an timer interrupt that runs every 10 ms. Here, basically some if-loops decide whether the value of shutterpos has changed in the last second (period is dependent on j, see code). If so, the new value is set and the signal is changed accordingly. If not, no signal is sent to the servo (just high, no PWM). The reason for that is that, in this way, the servo is only driven when needed and left passive when not needed, what prevents needless vibrations of the system. At the start of the interrupt SREG is back saved and reloaded in the end to make the program more robust and save.

At the input output initialization the pins are set in the needed configurations (input, output, internal pull-ups). For a default check of the LEDs, by _delay_ms(1000), all LEDs shine for 1 s. At the interrupt initialization, the timer interrupt frequency is set, as well as the mode of the external interrupt. At the PWM initialization, the mode, as well as the pulse of the signal (50 Hz) is set

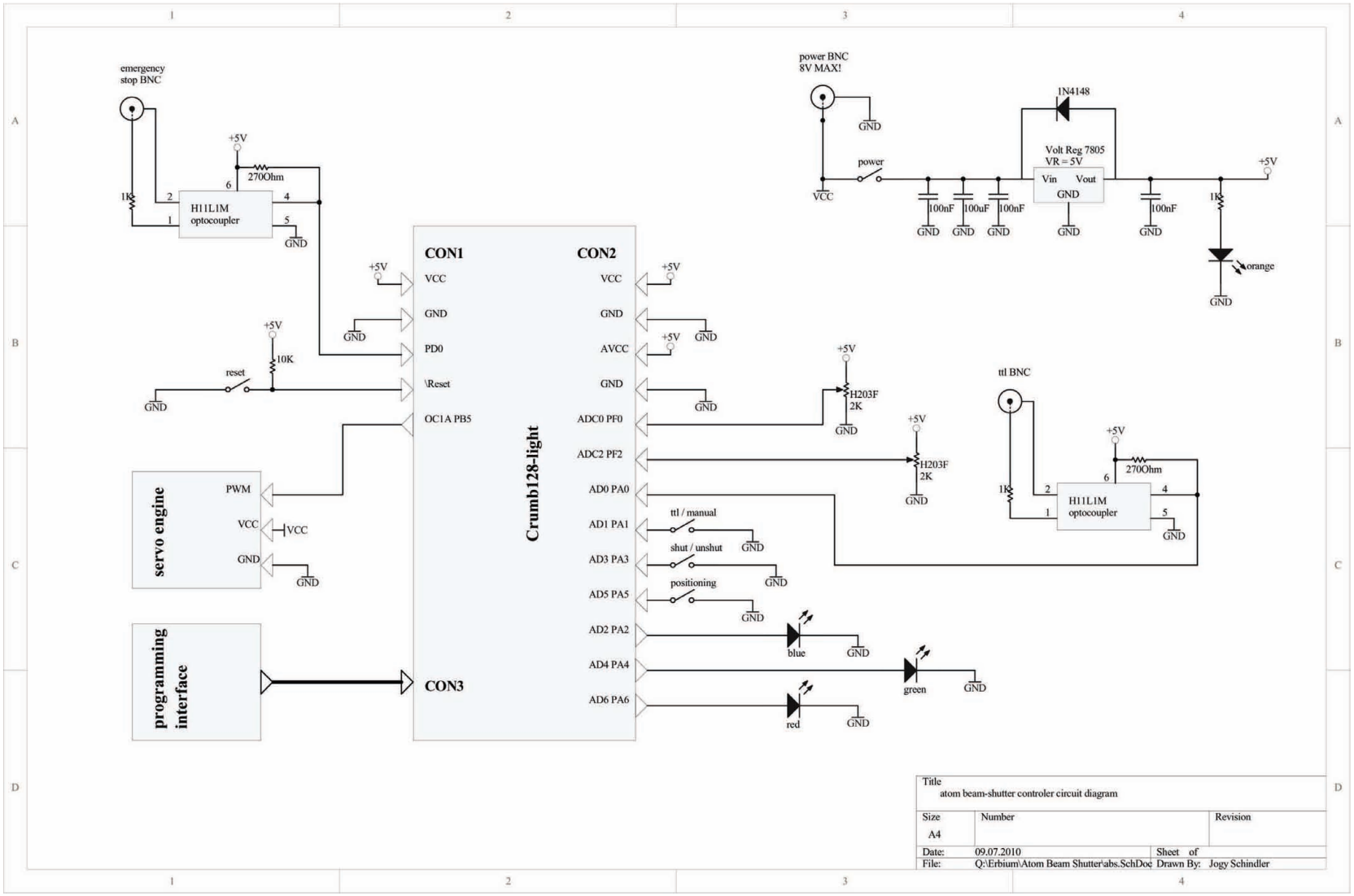

Figure C.1: The circuit diagram of the atomic beam shutter control box, which operates a servo motor. An Atmel *AVR ATmega128* μC with external resonator is mounted on the *Crumb128-light* μC module. Opto-isolators give galvanic separation, the voltage regulator protects the μC from high voltage

(ICR1). At the analog to digital conversion initialization, the mode is selected and a dummy readout takes place, for reserving the variable for the upcoming results.

The measurement functions do a simple ADC k times to give a stable average (important: clear the channel before selecting it). The flashing of the LEDs is done by a simple counting of b. Manual_control checks the switch for choosing the shutter position manually and sets the value of shutterpos accordingly. Whereas in pc_control shutterpos is set according to the TTL signal from the pc (which is inverted ↔ optocoupler)."

Listing C.1: Source code of the μC firmware.

```
/***************************
atom beam-shutter controller
***************************/

//version 1.0
//author: jogy schindler
//date: 07.07.010


#include <avr/io.h>
#include <avr/interrupt.h>
#include "abs.h"
#include <util/delay.h>


//---------
//main loop
//---------

int main(void)
{
    cli();
    init_io();
    init_int();
    init_pwm();
    init_adc();
    sei();

    while(1)
    {
        e = PIND;    //check and filter emergency stop status
        e &= (1<<PD0);

        if (e==0)    //signal @ bnc is high (no emergency stop) -> signal @ pin is low (optocoupler), normal operation
        {
            l = PINA;    //check and filter switchposition
            l &= (1<<PA1);

            if (l==0)    //switch [MANUAL_CONTROL <-> PC_CONTROL] == MANUAL_CONTROL
            {
                m = PINA;    //check and filter switchposition
                m &= (1<<PA5);
                m /= 32;

                if (m==1)    //switch [SHUTTER_POSITIONING <-> OPERATING] == OPERATING
                {
                    manual_control();
                }

```

```
                else    //switch [SHUTTER_POSITIONING <-> OPERATING] == SHUTTER_POSITIONING
                {
                    measure_poti1(); //measure potentiometer 1 for value of beam_unshut
                    measure_poti2(); //measure potentiometer 2 for value of beam_shut

                    manual_control();
                }
            }

            else    //switch [MANUAL_CONTROL <-> PC_CONTROL] == PC_CONTROL
            {
                pc_control();
                led_b_on();
            }
        }

        else    //signal @ bnc is low (emergency stop) -> signal @ pin is high (optocoupler), emergency stop
        {
            OCR1A = (3*beam_shut)+1000; //set servo to beam_shut

            led_flash();    //for indication of emergency stop
            h = 0;  //h reset for business as usual after emergency stop
        }
    }

    return 1;
}


//---------
//interrupt
//---------

//timer interupt for setting servo
ISR(TIMER3_COMPA_vect)
{
    stemp = SREG;   //backsaving SREG
    TCNT3 = 0;      //reset

    if (shutterpos != h)    //if shutterpos changed
    {
        j=0;
        OCR1A = (3*shutterpos)+1000;        //set pulselenght (empirical formula, by theoretical estimate, and experimental trial an error)
        h = shutterpos; //inverse pulselenghtfunction for if loop
    }

    if (shutterpos == h)    //if shutterpos unchanged
    {
        if (j<100)  //if shutterpos changed recently
        {
            OCR1A = (3*shutterpos)+1000;        //set pulselenght, until new servo position is driven (j=100 = 1 s, for 180  servo needs ~0.8 s, so if fast signal-off use with 90  set j=50 - but check accurately!)
            h = shutterpos; //inverse pulselenghtfunction for if loop
        }
        if (j>=100) //if shutterpos unchanged for longer time
        {
            j=200;  //stay in this mode until shutterpos changes
            OCR1A = ICR1;   //no pwm signal to servo, for avoiding vibrations
        }
    }

    j++;
    SREG = stemp;   //loading SREG
```

```
112 }
113
114
115 //---------------
116 //initialisation
117 //---------------
118
119 //input-output initialisation
120 void init_io(void)
121 {
122     DDRA |= (1<<PA2) | (1<<PA4) | (1<<PA6);      //leds set to output
123     PORTA |= (1<<PA0) | (1<<PA1) | (1<<PA3) | (1<<PA5); //activate pull-up @ ttl
        -pin and switches
124     DDRB |= (1<<PB5);          //servo-pin set to output
125     PORTD |= (1<<PD0);   //activate pull-up @ emergency stop
126
127     led_all_on();         //default led check @ initialisation: all leds on for 1s
128     _delay_ms(1000);
129     led_all_off();
130 }
131
132
133 //interrupt initialisation
134 void init_int(void)
135 {
136     TCCR3B |= (1<<CS32) | (1<<CS30);     //prescaler = 1024, normal operation
        mode (see table 61 in datasheet)
137     OCR3A = (int)(((XTAL/1024)*10)/1000);    //compare: timer-interupt every 10ms
        , take care on the brakets and calculation order: crucial! OCR3A=f(clk)
        /(prescaler*f(OCR3A))
138     ETIMSK = (1<<OCIE3A);         //timer3-compare-interrupt-enable
139 }
140
141
142 //pulsewidthmodulation initialisation
143 void init_pwm(void)
144 {
145     TCCR1A = (1<<COM1A1) | (1<<WGM11); //noninverting fast pwm, TOP is ICR1 (
        mode 14, see table 61 in datasheet)
146     TCCR1B = (1<<WGM13) | (1<<WGM12) | (1<<CS11); //fast pwm with prescaler 8 (
        resolution maximal)
147     ICR1 = 36865; //TOP \equiv 20ms (@prescaler 8) -> 50Hz pulse [ICR1=(f(clk)/(
        prescaler*f(pwm)))] --> OCR1A=3687,...,1843
148 }
149
150
151 //analog to digital convertion initialisation
152 void init_adc(void)
153 {
154     ADMUX |= (1<<REFS0);     //reference voltage is AVCC
155     ADCSRA |= (1<<ADEN) | (1<<ADPS2) | (1<<ADPS1) | (1<<ADPS0); //activate ADC,
        prescaler = 128 (-> ADC frequency = 115kHz)
156
157     ADCSRA |= (1<<ADSC);     //start dummy readout
158     while ( ADCSRA & (1<<ADSC) )
159     {;} //wait for end of conversion
160     beam_unshut = ADCW;      //read ADCW to get result of the next measurement in
         this variable
161
162     measure_poti1();     //measure the potis for selecting the recent set
        settings
163     measure_poti2();
164 }
165
166
167 //---------
168 //functions
169 //---------
170
171 //voltage measurement @ potentiometer #1
```

```
172 void measure_poti1(void)
173 {
174     ADMUX &= ~(1<<MUX1);     //set channel zero, chose channel ADC0 (default)
175     beam_unshut = 0;
176
177     for (k=0; k<32; k++) //measure k+1 times and average, chose k as 2^n for
            faster calculation
178     {
179         ADCSRA |= (1<<ADSC);     //single conversion
180         while ( ADCSRA & (1<<ADSC) )
181         {;}
182         beam_unshut += ADCW;
183     }
184     beam_unshut /= (k+1);
185 }
186
187
188 //voltage measurement @ potentiometer #2
189 void measure_poti2(void)
190 {
191     ADMUX &= ~(1<<MUX1);     //set channel zero
192     ADMUX |= (1<<MUX1);      //chose channel ADC2
193     beam_shut = 0;
194
195     for (k=0; k<32; k++)     //measure k+1 times and average
196     {
197         ADCSRA |= (1<<ADSC);     //single conversion
198         while ( ADCSRA & (1<<ADSC) )
199         {;}
200         beam_shut += ADCW;
201     }
202     beam_shut /= (k+1);
203 }
204
205
206 //flashing leds @ emergency block
207 void led_flash(void)
208 {
209     if ((0<b && b<20000))
210     {
211         led_all_on();
212     }
213     if ((10000<b && b<40000))
214     {
215         led_all_off();
216     }
217     if (b>=40000)
218     {
219             b=0;
220     }
221     b++;
222 }
223
224
225 //sets the shutterposition according to the [SHUTTERPOS=BEAM_SHUT <-> SHUTTERPOS
        =BEAM_UNSHUT]-switch
226 void manual_control(void)
227 {
228     i = PINA;
229     i &= (1<<PA3);
230     i /= 8;
231
232     if (i==1)    //switch [SHUTTERPOS=BEAM_SHUT <-> SHUTTERPOS=BEAM_UNSHUT] ==
            SHUTTERPOS=BEAM_UNSHUT
233     {
234         shutterpos = beam_unshut;
235         led_all_off();
236         led_g_on();
237     }
238
```

```
    else    //switch [SHUTTERPOS=BEAM_SHUT <-> SHUTTERPOS=BEAM_UNSHUT] ==
        SHUTTERPOS=BEAM_SHUT
    {
        shutterpos = beam_shut;
        led_all_off();
        led_r_on();
    }
}


//sets the shutterposition according to the TTL signal from the PC (inverted!)
void pc_control(void)
{
    ttl = PINA;
    ttl &= (1<<PA0);

    if (ttl==1)
    {
        shutterpos = beam_shut;
        led_all_off();
        led_r_on();
    }

    else
    {
        shutterpos = beam_unshut;
        led_all_off();
        led_g_on();
    }
}
```

Listing C.2: Header of the source code.

```
/*************************************
atom beam-shutter controller - header
*************************************/


//constants

#define XTAL (double) 14745600  //quarz frequency, (double) to format -> helps
    with calculations
#define F_CPU 14745600UL    //cpu frequency defined for delay.h


//macros

#define led_b_on()      PORTA |= (1<<PA2)
#define led_b_off()         PORTA &= ~(1<<PA2)
#define led_g_on()      PORTA |= (1<<PA4)
#define led_g_off()     PORTA &= ~(1<<PA4)
#define led_r_on()      PORTA |= (1<<PA6)
#define led_r_off()     PORTA &= ~(1<<PA6)
#define led_all_on()        PORTA |= (1<<PA2) | (1<<PA4) | (1<<PA6)
#define led_all_off()       PORTA &= ~((1<<PA2) | (1<<PA4) | (1<<PA6))


//variables

unsigned char e;    //for emergeny stop
unsigned char i;    //for switch SHUTTERPOS=BEAM_SHUT <-> SHUTTERPOS=BEAM_UNSHUT
unsigned char l;    //for switch MANUAL_CONTROL <-> PC_CONTROL
unsigned char m;    //for switch POSITIONING <-> OPERATING
unsigned char ttl;  //for TTL signal
unsigned char j=0;  //for counter of timer interrupts
unsigned int h=0;   //for interrupt intermediate memory @ if loops
unsigned int k;     //for counter of measure_poti# mean-loop
unsigned int b=0;   //for counter of function flash
unsigned int stemp; //for backsaving SREG when interrupt is performed
volatile unsigned int shutterpos;   //volatile, since used for timer-interrupt
```

```
37 unsigned int beam_unshut;
38 unsigned int beam_shut;
39
40
41 //functions
42
43 void init_io(void);
44 void init_int(void);
45 void init_pwm(void);
46 void init_adc(void);
47 void measure_poti2(void);
48 void measure_poti1(void);
49 void manual_control(void);
50 void pc_control(void);
51 void led_flash(void);
```

Appendix D

Calibrations

D.1 Laser frequency

To calibrate the laser frequency in the scanning region, we use a wavemeter. It measures the wavelength of the non-frequency-doubled 802 nm light from the test output of the laser system. Since the light is transported with a long fiber to the wavemeter, the measurement is vulnerable to temperature fluctuations and vibrations. Also the switcher box that is used to share the wavemeter with other experiments reduces the accuracy and time resolution if operated in switch mode. Therefore, this method is not suitable for absolute frequency measurements. However, for relative frequency measurements with time averaged values, the precision is sufficient. A long-term record from the wavemeter gives the maximum and minimum frequencies of the scan. To obtain the real maximum and minimum wavelength values, it is important to average the recorded values over long times and then choose the absolute maxima and minima. Figure D.1 shows such a record of the wavelength as a function of the time. The amplitudes do not correspond to the real amplitudes, as we can see by the interference pattern of the data points. Since the sampling rate of the wavemeter is too small to allow smooth sampling, we observe interference with the scan rate of the laser. To convert the time axis of the measurements at the oscilloscope to a frequency axis, we determine the frequency change per time. We measure the scan rate of the laser with an oscilloscope and combine this with the absolute maxima and minima of the frequencies to obtain the frequency change per unit time of the scan. We scale the time scale of the oscilloscope with this value and obtain a frequency axis, which we normalize to the ^{166}Er absorption peak and that thus shows the relative detuning.

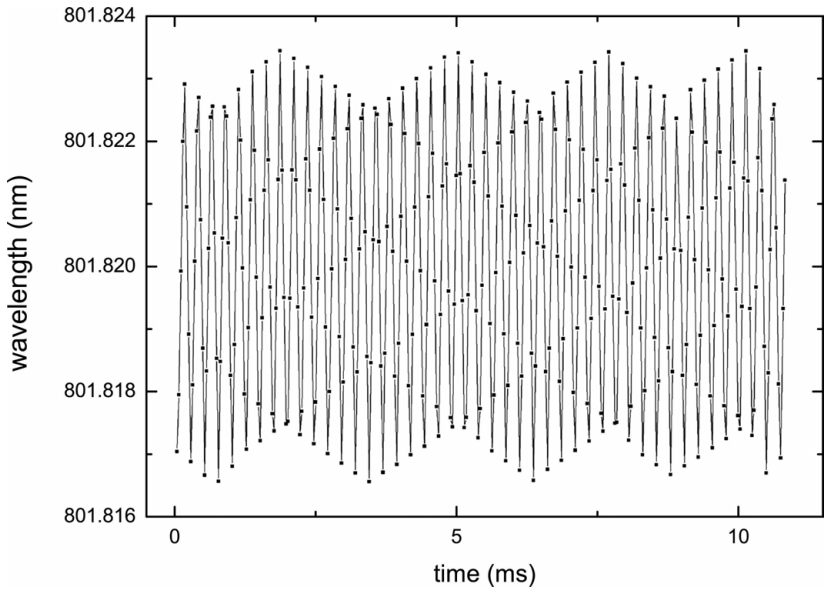

Figure D.1: Interference pattern of the laser scan rate and the sampling rate of the wavemeter. The amplitude response does not correspond to the real amplitudes since the sampling rate is too small.

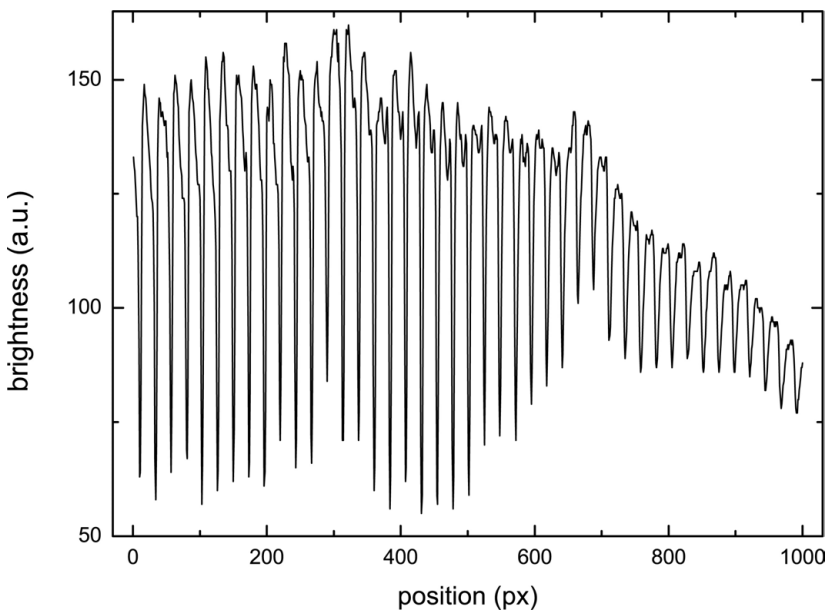

Figure D.2: Brightness as a function of position along one pixel row of an image of an ruler. One peak spacing corresponds to 1 mm what determines the scaling factor.

D.2 CCD camera

To calibrate the pixel size of the CCD images, we focus the camera lens to a ruler at equal distance as the center of the chamber. The profile along one pixel row of the resulting image, as in Fig. D.2, shows distinct peaks with a spacing of 1 mm. This determines the scaling factor to convert pixel to mm.

The exposure time of the camera needs to be short to avoid saturation of the CCD chip. As well, it needs to be long to detect very low fluorescence light intensities. To find the optimum value, we measured the waist of an imaged atomic cloud as a function of the exposure time. A measurement-set at $T_{\mathrm{EC}} = 1350\,^{\circ}\mathrm{C}$ and $T_{\mathrm{HL}} = 1450\,^{\circ}\mathrm{C}$ gives the upper bound, another set at $T_{\mathrm{EC}} = 1250\,^{\circ}\mathrm{C}$ and $T_{\mathrm{HL}} = 950\,^{\circ}\mathrm{C}$ gives the lower bound. As we see in Fig. D.3, for exposure times below 100 ms, the low temperature cloud cannot be detected properly. For exposure times above 250 ms, the waist of the high-temperature cloud is no longer constant, but it depends linearly on the exposure time. It seems likely that this is a smear effect, where at the readout of the chip, charges from the overexposed pixels swap to neighboring pixels by mistake and broaden the bright region. This measurement was made at collimation setup 1 and leads to an optimal exposure time of 100 ms.

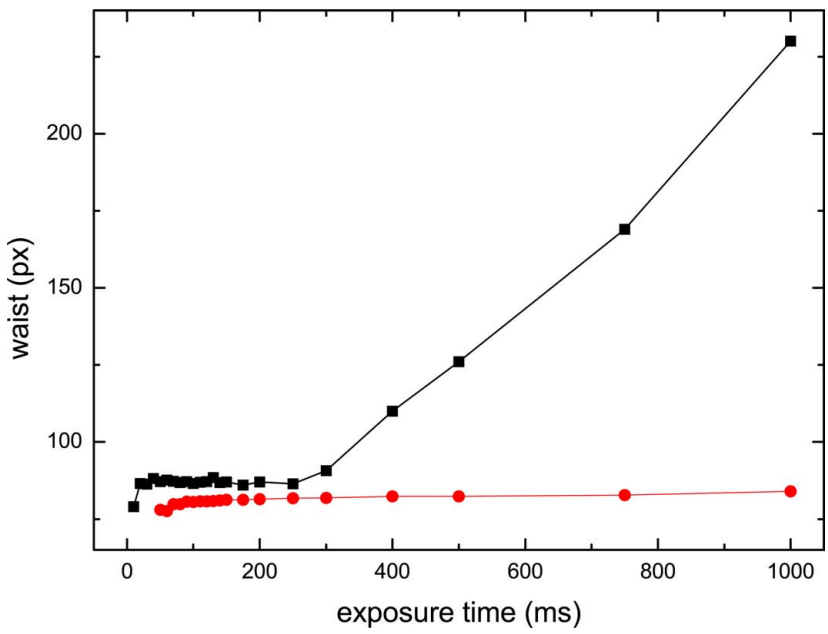

Figure D.3: The waist of an imaged atomic cloud in setup 1 for two different temperature settings. For too short or too long exposure times, the waist is no longer constant.

Bibliography

[1] S. Ospelkaus, K.-K. Ni, D. Wang, M. H. G. de Miranda, B. Neyenhuis, G. Quéméner, P. S. Julienne, J. L. Bohn, D. S. Jin, and J. Ye, *Quantum-State Controlled Chemical Reactions of Ultracold Potassium-Rubidium Molecules*, Science 327, 853 (2010).

[2] M. Greiner and S. Föllig, *Condensed-matter physics: Optical lattices*, Nature 453, 736 (2008).

[3] F. Ferlaino and R. Grimm, *Forty years of Efimov physics: How a bizarre prediction turned into a hot topic*, Physics 3, 9 (2010).

[4] J. K. Chin, D. E. Miller, Y. Liu, C. Stan, W. Setiawan, C. Sanner, K. Xu, and W. Ketterle, *Evidence for superfluidity of ultracold fermions in an optical lattice*, Nature 443, 961 (2006).

[5] R. P. Feynman, *Simulating physics with computers*, Int. J. Th. Phys. 21, 467 (1981).

[6] M. H. Anderson, J. R. Ensher, M. R. Matthews, C. E. Wieman, and E. A. Cornell, *Observation of Bose-Einstein Condensation in a Dilute Atomic Vapor*, Science 269, 198 (1995).

[7] C. C. Bradley, C. A. Sackett, J. J. Tollett, and R. G. Hulet, *Evidence of Bose-Einstein Condensation in an Atomic Gas with Attractive Interactions*, Phys. Rev. Lett. 75, 1687 (1995).

[8] K. B. Davis, M.-O. Mewes, M. R. Andrews, N. J. van Druten, D. S. Durfee, D. M. Kurn, and W. Ketterle, *Bose-Einstein Condensation in a Gas of Sodium Atoms*, Phys. Rev. Lett. 75, 3969 (1995).

[9] B. DeMarco and D. S. Jin, *Onset of Fermi Degeneracy in a Trapped Atomic Gas*, Science 285, 1703 (1999).

[10] A. G. Truscott, K. E. Strecker, W. I. McAlexander, G. B. Partridge, and R. G. Hulet, *Observation of Fermi Pressure in a Gas of Trapped Atoms*, Science 291, 2570 (2001).

[11] F. Schreck, L. Khaykovich, K. L. Corwin, G. Ferrari, T. Bourdel, J. Cubizolles, and C. Salomon, *Quasipure Bose-Einstein Condensate Immersed in a Fermi Sea*, Phys. Rev. Lett. 87, 080403 (2001).

[12] C. Chin, R. Grimm, P. Julienne, and E. Tiesinga, *Feshbach resonances in ultracold gases*, Rev. Mod. Phys. 82, 1225 (2010).

[13] M. Gustavsson, E. Haller, M. J. Mark, J. G. Danzl, G. Rojas-Kopeinig, and H.-C. Nägerl, *Control of Interaction-Induced Dephasing of Bloch Oscillations*, Phys. Rev. Lett. 100, 080404 (2008).

[14] K. K. Winkler, G. Thalhammer, F. Lang, R. Grimm, J. H. Denschlag, A. D. Daley, A. Kantian, H. P. Büchler, and P. Zoller, *Repulsively bound atom pairs in an optical lattice*, Nature 441, 853 (2006).

[15] S. Jochim, M. Bartenstein, A. Altmeyer, G. Hendl, S. Riedl, C. Chin, J. Hecker Denschlag, and R. Grimm, *Bose-Einstein Condensation of Molecules*, Science 302, 2101 (2003).

[16] F. Ferlaino, S. Knoop, and R. Grimm, *Ultracold Feshbach Molecules*, in *Cold Molecules: Theory, Experiment, Applications*, edited by R. Krems, F. Bretislav, and W. C. Stwalley, CRC Press, 2009.

[17] S. Stellmer, M. K. Tey, B. Huang, R. Grimm, and F. Schreck, *Bose-Einstein Condensation of Strontium*, Phys. Rev. Lett. 103, 200401 (2009).

[18] Y. N. M. de Escobar, P. G. Mickelson, M. Yan, B. J. DeSalvo, S. B. Nagel, and T. C. Killian, *Bose-Einstein Condensation of* ^{84}Sr, Phys. Rev. Lett. 103, 200402 (2009).

[19] S. Kraft, F. Vogt, O. Appel, F. Riehle, and U. Sterr, *Bose-Einstein Condensation of Alkaline Earth Atoms:* ^{40}Ca, Phys. Rev. Lett. 103, 130401 (2009).

[20] T. Lahaye, C. Menotti, L. Santos, M. Lewenstein, and T. Pfau, *The physics of dipolar bosonic quantum gases*, Rep. Prog. Phys. 72, 126401 (2009).

[21] M. Baranov, *Theoretical progress in many-body physics with ultracold dipolar gases*, Phys. Rep. 464, 71 (2008).

[22] J. M. Sage, S. Sainis, T. Bergeman, and D. DeMille, *Optical Production of Ultracold Polar Molecules*, Phys. Rev. Lett. 94, 203001 (2005).

[23] K.-K. Ni, S. Ospelkaus, M. H. G. de Miranda, A. Pe'er, B. Neyenhuis, J. J. Zirbel, S. Kotochigova, P. S. Julienne, D. S. Jin, and J. Ye, *A High Phase-Space-Density Gas of Polar Molecules*, Science 322, 231 (2008).

[24] A. Griesmaier, J. Werner, S. Hensler, J. Stuhler, and T. Pfau, *Bose-Einstein Condensation of Chromium*, Phys. Rev. Lett. 94, 160401 (2005).

[25] T. Lahaye, J. Metz, B. Fröhlich, T. Koch, M. Meister, A. Griesmaier, T. Pfau, H. Saito, Y. Kawaguchi, and M. Ueda, *d-Wave Collapse and Explosion of a Dipolar Bose-Einstein Condensate*, Phys. Rev. Lett. 101, 080401 (2008).

[26] T. Koch, T. Lahaye, J. Metz, B. Fröhlich, A. Griesmaier, and T. Pfau, *Stabilization of a purely dipolar quantum gas against collapse*, Nature Phys. 4, 218 (2008).

[27] B. Pasquiou, G. Bismut, E. Maréchal, P. Pedri, L. Vernac, O. Gorceix, and B. Laburthe-Tolra, *Spin Relaxation and Band Excitation of a Dipolar Bose-Einstein Condensate in 2D Optical Lattices*, Phys. Rev. Lett. 106, 015301 (2011).

[28] S. H. Youn, M. Lu, and B. L. Lev, *Anisotropic sub-Doppler laser cooling in dysprosium magneto-optical traps*, Phys. Rev. A 82, 043403 (2010).

[29] H. Y. Ban, M. Jacka, J. L. Hanssen, J. Reader, and J. J. McClelland, *Laser cooling transitions in atomic erbium*, Opt. Express 13, 3185 (2005).

[30] D. Sukachev, A. Sokolov, K. Chebakov, A. Akimov, S. Kanorsky, N. Kolachevsky, and V. Sorokin, *Magneto-Optical Trap for Thulium Atoms*, arXiv:1003.0877v2 (2010).

[31] C. I. Hancox, S. C. Doret, M. T. Hummon, L. Luo, and J. M. Doyle, *Magnetic trapping of rare-earth atoms at millikelvin temperatures*, Nature 431, 281 (2004).

[32] C. B. Connolly, Y. S. Au, S. C. Doret, W. Ketterle, and J. M. Doyle, *Large spin relaxation rates in trapped submerged-shell atoms*, Phys. Rev. A 81, 010702 (2010).

[33] J. J. McClelland and J. L. Hanssen, *Laser Cooling without Repumping: A Magneto-Optical Trap for Erbium Atoms*, Phy. Rev. Lett. 96, 143005 (2006).

[34] A. J. Berglund, J. L. Hanssen, and J. J. McClelland, *Narrow-Line Magneto-Optical Cooling and Trapping of Strongly Magnetic Atoms*, Phys. Rev. Lett. 100, 113002 (2008).

[35] N. F. Ramsey, *Thermal Atom Beams*, in *Atomic, Molecular and Optical Physics: Atoms and Molecules*, edited by F. B. Dunning and R. G. Hulet, volume 29B of *Experimental Methods in the Physical Sciences*, chapter 1, Academic Press, 1996.

[36] J. F. O'Hanlon, *A User's Guide to Vacuum Technology*, John Wiley & Sons, 2003.

[37] N. Ramsey, *Molecular Beams*, Oxford University Press, 1985.

[38] W. Demtröder, *Laser Spectroscopy: Basic Concepts and Instrumentation*, Springer, 2010.

[39] W. Demtröder, *Experimentalphysik 3 – Atome, Moleküle und Festkörper*, Springer, 2005.

[40] H. Haken and H. C. Wolf, *Atom- und Quantenphysik*, Springer, 1990.

[41] H. J. Metcalf and P. van der Straten, *Laser Cooling and Trapping*, Springer, 1999.

[42] J. J. Olivero and R. L. Longbothum, *Empirical fits to the Voigt line width: A brief review*, J. Quant. Spectrosc. Radiat. Transfer 17, 12 (1977).

[43] R. Mears, L. Reekie, S. Poole, I.M., and D. Payne, *Low-threshold tunable CW and Q-switched fibre laser operating at 1.55 μm*, Electr. Lett. 22, 159 (1986).

[44] A. Klinger, *Optical Frequency Comb for Ultracold Groundstate Molecules*, Master's thesis, Universität Innsbruck, 2011.

[45] R. Mears, L. Reekie, I. Jauncey, and D. Payne, *Low-noise erbium-doped fibre amplifier operating at 1.54 μm*, Electr. Lett. 23, 1026 (1987).

[46] E. Desurvire, J. R. Simpson, and P. C. Becker, *High-gain erbium-doped traveling-wave fiber amplifier*, Opt. Lett. 12, 888 (1987).

[47] A. A. Olsson, J. R. Simpson, N. Olsson, and P. C. Becke, *Erbium-Doped Fiber Amplifiers*, Academic Press, 1999.

[48] G. Teikemeier and D. Goldberg, *Skin resurfacing with the erbium:YAG laser*, Dermatol. Surg. 23, 685 (1997).

[49] E. Bornstein, *Proper use of Er:YAG lasers and contact sapphire tips when cutting teeth and bone: scientific principles and clinical application*, Dent. Today 23, 86 (2004).

[50] F. H. Spedding, A. H. Daane, and K. W. Herrmann, *The crystal structures and lattice parameters of high-purity scandium, yttrium and the rare earth metals*, Acta Cryst. 9, 559 (1956).

[51] R. Chicireanu, *Studies of cold chromium atoms in magnetic and optical traps: steps towards Bose-Einstein Condensation*, PhD thesis, Université Paris-Nord, 2007.

[52] A. M. James and M. P. Lord, *Macmillan's chemical and physical data*, Macmillan, 1992.

[53] D. E. Gray, *American Institute of Physics Handbook*, American Institute of Physics, 1972.

[54] C. Antoine, *Tensions des vapeurs; nouvelle relation entre les tensions et les températures*, Comp. Rend. Séanc. l'Acad. Scie. Paris 107, 681 (1888).

[55] F. Lindemann, *The calculation of molecular vibration frequencies*, Physik. Z. 11, 609 (1910).

[56] J. Mueller, B. Singh, and N. A. Surplice, *The gettering action of evaporated films of titanium and erbium*, J. Phys. D 5, 1177 (1972).

[57] M. Saffman and K. Mølmer, *Scaling the neutral-atom Rydberg gate quantum computer by collective encoding in holmium atoms*, Phys. Rev. A 78, 012336 (2008).

[58] A. J. Berglund, S. Lee, and J. J. McClelland, *Sub-Doppler laser cooling and magnetic trapping of erbium*, Phys. Rev. A 76, 053418 (2007).

[59] W. C. Martin, R. Zalubas, and L. Hagan, *Atomic Energy Levels – The Rare-Earth Elements*, National Institute of Standards and Technology, 1972.

[60] C. J. Foot, *Atomic Physics*, Oxford University Press, 2005.

[61] G. W. Drake, *Atomic, Molecular and Optical Physics Handbook*, American Institute of Physics, 1996.

[62] B. G. Wybourne and L. Smentek, *Optical Spectroscopy of Lanthanides - Magnetic and Hyperfine Interactions*, CRC Press, 2007.

[63] J. K. Boehlke, J. R. Laeter, P. De Bievre, H. Hidaka, H. S. Peiser, K. J. Rosman, and P. D. Taylor, *Isotopic Compositions of the Elements, 2001*, J. Phys. Chem. Ref. Data 34, 57 (2005).

[64] F. Schreck, G. Ferrari, K. L. Corwin, J. Cubizolles, L. Khaykovich, M.-O. Mewes, and C. Salomon, *Sympathetic cooling of bosonic and fermionic lithium gases towards quantum degeneracy*, Phys. Rev. A 64, 011402 (2001).

[65] M. K. Tey, S. Stellmer, R. Grimm, and F. Schreck, *Double-degenerate Bose-Fermi mixture of strontium*, Phys. Rev. A 82, 011608 (2010).

[66] R. J. Lipert and S. C. Lee, *Isotope shifts and hyperfine structure of erbium, dysprosium, and gadolinium by atomic-beam diode-laser spectroscopy*, Appl. Phys. B 57, 373 (1993).

[67] W.-G. Jin, T. Horiguchi, M. Wakasugi, and Y. Yoshizawa, *Hyperfine Structure and Isotope Shift in Er I by the Atomic-Beam Laser Spectroscopy*, JPSJ 59, 3148 (1990).

[68] J. J. McClelland, *Natural linewidth of the 401-nm laser-cooling transition in Er I*, Phys. Rev. A 73, 064502 (2006).

[69] E. A. Den Hartog, J. P. Chisholm, and J. E. Lawler, *Radiative lifetimes of neutral erbium*, J. Phys. B 43, 155004 (2010).

[70] S. H. Youn, M. Lu, U. Ray, and B. L. Lev, *Dysprosium magneto-optical traps*, Phys. Rev. A 82, 043425 (2010).

[71] M. Walhout, J. Dalibard, S. L. Rolston, and W. D. Phillips, σ_+- σ_- *Optical molasses in a longitudinal magnetic field*, J. Opt. Soc. Am. B 9, 1997 (1992).

[72] J. Werner, H. Wallis, and W. Ertmer, *Atoms with anomalous Zeeman effect in a 1D-magneto-optical molasses*, Opt. Commun. 94, 525 (1992).

[73] J. Jensen and A. R. Mackintosh, *Rare Earth Magnetism: Structures and Excitations*, Clarendon Press Oxford, 1991.

[74] J. P. D'Incao and C. H. Greene, *Collisional Aspects of Bosonic and Fermionic Dipoles in Quasi-Two-Dimensional Confining Geometries*, arXiv:1011.3469v2 (2010).

[75] W. Ketterle and N. J. van Druten, *Evaporative Cooling of Trapped Atoms*, Adv. At. Mol. Opt. Phys. 35, 181 (1996).

[76] R. V. Krems, G. C. Groenenboom, and A. Dalgarno, *Electronic Interaction Anisotropy between Atoms in Arbitrary Angular Momentum States*, J. Phys. Chem. A 108, 8941 (2004).

[77] A. A. Buchachenko, Y. V. Suleimanov, M. M. Szczesniak, and G. Chalasinski, *Interactions and collisions of cold metal atoms in magnetic traps*, Phys. Scr. 80, 048109 (2009).

[78] N. Leefer, A. Cingöz, B. Gerber-Siff, A. Sharma, J. R. Torgerson, and D. Budker, *Transverse laser cooling of a thermal atomic beam of dysprosium*, Phys. Rev. A 81, 043427 (2010).

[79] E. Wille, *Preparation of an Optically Trapped Fermi-Fermi Mixture of* ^{6}*Li and* ^{40}*K Atoms and Characterization of the Interspecies Interactions by Feshbach Spectroscopy*, PhD thesis, Universität Innsbruck, 2009.

[80] G. Thalhammer, *Ultrakalte gepaarte Atome in kohärenten Lichtfeldern*, PhD thesis, Universität Innsbruck, 2007.

[81] R. K. Raj, D. Bloch, J. J. Snyder, G. Camy, and M. Ducloy, *High-Frequency Optically Heterodyned Saturation Spectroscopy Via Resonant Degenerate Four-Wave Mixing*, Phys. Rev. Lett. 44, 1251 (1980).

[82] D. J. McCarron, S. A. King, and S. L. Cornish, *Modulation transfer spectroscopy in atomic rubidium*, Meas. Sci. Technol. 19, 105601 (2008).

[83] CreaTec Fischer & Co. GmbH, *Dual Filament Effusion-Cell DFC-40-10-290-WK*, Industriestr. 9, 74391 Erligheim, Germany, 2009.

[84] S. Kroboth, *Laserkühlung von Ytterbiumatomen*, Master's thesis, Universität Stuttgart, 2002.

List of Symbols and Abbreviations

Abbreviation	Description
2-LS	two level system
A	area
a	distance between two apertures
a	scattering length
a.u.	arbitrary units
a_{dd}	dipole-dipole characteristic radius
a_0	Bohr radius
ADC	analog to digital conversion
α	angle of emergence relative to the z-axis from the oven
amu	atomic mass unit
b	inner diameter of aperture
BEC	Bose-Einstein condensate
c	speed of light
C	normalisation constant
CCD	charge-coupled device
d	atomic beam diameter
D	$\ln(10)\times$ optical density
DDI	dipole-dipole interaction
$\Delta\nu$	linewidth
E	energy
$\lvert e\rangle$	excited state
EC	effusion cell
EOM	electro-optic modulator
f	collimation ratio
F	quantum number of the hyperfine splitting
FWHM	full width half maximum
g	Landé-g factor

Abbreviation	Description
$\|e\rangle$	ground state
Γ	spontaneous decay rate
h	Planck constant
$\hbar$	reduced Planck constant
HCL	hollow cathode lamp
HL	hot lip
I	intensity
I	total nuclear spin quantum number
I_{sat}	saturation intensity
IC	integrated circuit
j	light-atom interaction length
J	total angular momentum quantum number
k	photon momentum
k_B	Boltzmann constant
l	distance from aperture 2
L	total orbital angular momentum quantum number
λ	wavelength
λ_{mf}	mean free path
$\lambda/2$	half-wave plate
LED	light emitting diode
LO	local oscillator
m	mass
m_J	projection of the total angular momentum quantum - - number to the quantization axis
MOT	magneto-optical trap
μ	magnetic moment
μC	mirco controller
μ_0	magnetic constant
μ_B	Bohr magneton
n	density
ν	frequency
ν_0	resonance frequency
NIST	National Institute of Standards and Technology
OD	optical density
ODT	optical dipole trap
ω	solid angle
PBS	polarizing beam splitter
PD	photo diode
Θ	flux
PID	proportional integral derivative

Abbreviation	Description
PWM	pulse width modulation
r	absolute distance
S	total spin quantum number
σ_{at}	atom-atom cross-section
σ_0	light-atom cross-section
smsf	single-mode single-frequency
T	temperature
t	time
τ	lifetime
TC	transversal cooling
TTL	transistor-transistor logic
UHV	ultra high vacuum
UPS	uninterrupted power supply
v	velocity
V	volume
ZS	Zeeman slower

Merci!

First, I would like to thank my supervisor Francesca Ferlaino for giving me the opportunity to participate in setting up this new experiment. Especially from her, I also learnt things that are not directly connected to physics, such as presenting and writing. In moments when we underestimated the power of Hofstadter's law, our team play was exceptionally good – thanks. Großer Dank geht auch an Rudi Grimm; dafür, in seiner Arbeitsgruppe mitarbeiten zu können, für seine weisen physikalischen Ratschläge, als auch für die Möglichkeit an der EuroQUAM und dem netten Waldrast-Retreat teilnehmen zu können.

I thank our continuously growing erbium team for the great team work. Besonders von Alberts schier grenzenlosen Technik Know-How konnte ich mir so manches abschauen. Danke für die vielen feinen gemeinsamen Laborstunden. I also want to mention Kiyotaka, with whom I shared some inspiring discussions on easy, but amazingly complicated atomic beam physics.

The whole group offered a very pleasant and supporting working atmosphere with tasty 'cakes at 4' and many answers to my questions – thanks to all of you. Besonderen Dank an Simon – meinen 'Postdoc' – der mir viel bei Belangen rund ums blaue Licht half and also to Matteo for his supporting smile. Im weiteren danke ich unseren Werkstattmitarbeitern für die technische Unterstützung, die vor allem beim Aufbau eines neuen Experiments nötig ist. Besonders Helmut brachte mir mit seiner aufgeweckten Art die Bedienung vieler Maschinen bei.

Seit Begin meines Studiums begleitete mich und viele andere Studenten Sabine Schindler als Studienbeauftragte bei allem Offiziellem höchst unbürokratisch, geduldig und fair – vielen Dank. Von Peter Zollers fast schon legendären Vorlesungen konnte ich sehr viel lernen, und im Nachhinein diese auch genießen. Danke auch an Alexander Glätzle, welcher mir hierbei als Tutor zur Seite stand und uns die Türen öffnete, um den Viktor Franz Hess Südpfeiler zu erklettern.

Ohne den tollen und bergbegeisterten Studienkollegen hätten diese 6 Jahre nicht halb so viel Spaß gemacht. Mit Roland und Ben teilte ich Biwakschachteln und Lerngruppen, mit Flo eine wahnsinns WG und viele Flaschen Wein. Adam, Andi und ich haben während der intensiven Diplomzeit viel zusammengearbeitet und uns zudem einige belebende Auszeiten erlaubt: Nachtklettern an der Mar-

tinswand, frühmorgentliche Gratüberschreitungen, Rennrad-Konferenzpausen, Feierabend-Saunen und natürlich unsere tägliche, obligate Kaffepause. Besten Dank. Auch meinem Bürokollegen Mohamed danke ich für erfrischende Schreibpausen mit Bürotennis und seine Hilfe bei unserem Umzug nur eine Woche vor Abgabe dieser Arbeit.

Hans Strack-Zimmermann möchte ich als meinen langjährigen Berater im Hintergrund danken. Meinen Eltern Lisa und Wolfgang danke ich über alles für ihre positive, vertrauensvolle Einstellung und die vielen Freiheiten die sie mir gaben. Ihre Großzügigkeit hat es mir ermöglicht hier in Innsbruck das zu studieren, was ich wollte. Schließlich möchte ich noch meiner wundervollen Freundin Chris danken, die mich besonders im letzten Jahr auf jede mögliche Weise unterstützt hat und somit auch einen Beitrag zu dieser Arbeit geleistet hat.

Merci!